University of Kentucky
UKnowledge

Theses and Dissertations--Physics and Astronomy

Physics and Astronomy

2016

Physical and Electronic Properties of Nanoscale 2D Materials

Mathias J. Boland
University of Kentucky, mbo233@g.uky.edu
Digital Object Identifier: https://doi.org/10.13023/ETD.2016.446

Right click to open a feedback form in a new tab to let us know how this document benefits you.

Recommended Citation

Boland, Mathias J., "Physical and Electronic Properties of Nanoscale 2D Materials" (2016). *Theses and Dissertations--Physics and Astronomy*. 39.
https://uknowledge.uky.edu/physastron_etds/39

This Doctoral Dissertation is brought to you for free and open access by the Physics and Astronomy at UKnowledge. It has been accepted for inclusion in Theses and Dissertations--Physics and Astronomy by an authorized administrator of UKnowledge. For more information, please contact UKnowledge@lsv.uky.edu.

STUDENT AGREEMENT:

I represent that my thesis or dissertation and abstract are my original work. Proper attribution has been given to all outside sources. I understand that I am solely responsible for obtaining any needed copyright permissions. I have obtained needed written permission statement(s) from the owner(s) of each third-party copyrighted matter to be included in my work, allowing electronic distribution (if such use is not permitted by the fair use doctrine) which will be submitted to UKnowledge as Additional File.

I hereby grant to The University of Kentucky and its agents the irrevocable, non-exclusive, and royalty-free license to archive and make accessible my work in whole or in part in all forms of media, now or hereafter known. I agree that the document mentioned above may be made available immediately for worldwide access unless an embargo applies.

I retain all other ownership rights to the copyright of my work. I also retain the right to use in future works (such as articles or books) all or part of my work. I understand that I am free to register the copyright to my work.

REVIEW, APPROVAL AND ACCEPTANCE

The document mentioned above has been reviewed and accepted by the student's advisor, on behalf of the advisory committee, and by the Director of Graduate Studies (DGS), on behalf of the program; we verify that this is the final, approved version of the student's thesis including all changes required by the advisory committee. The undersigned agree to abide by the statements above.

Mathias J. Boland, Student

Dr. Douglas R. Strachan, Major Professor

Dr. Christopher Crawford, Director of Graduate Studies

PHYSICAL AND ELECTRONIC PROPERTIES OF NANOSCALE 2D MATERIALS

DISSERTATION

A dissertation submitted in partial
fulfillment of the requirements for
the degree of Doctor of Philosophy
in the College of Arts and Sciences
at the University of Kentucky

By
Mathias J. Boland
Lexington, Kentucky

Director: Dr. Douglas R. Strachan, Professor of Physics
Lexington, Kentucky 2016

Copyright© Mathias J. Boland 2016

ABSTRACT OF DISSERTATION

PHYSICAL AND ELECTRONIC PROPERTIES OF NANOSCALE 2D MATERIALS

There is a great push towards reducing the size scale of both electronic components and machines. Two dimensional materials, such as graphene, are ideal candidates towards this push, as they are naturally atomically thin. In the case of nanoscale machines, the mechanical properties of the material surfaces become increasingly important. The use of laminar materials, such as graphene and MoS_2, to modify the surface properties, yet maintain nanoscale topographical features, are very attractive. Towards this goal, we have investigated the surface properties of MoS_2 at the nanoscale using Lateral Force Microscopy (LFM). In these investigations, we measure periodic frictional features with periodicity of ~ 4 nm. Ultrashort devices that incorporate atomically thin components have the potential to be the smallest electronics. Such extremely scaled devices are expected to show ballistic nonlinear behavior that could make them tremendously useful for ultra fast electronic applications. We report nonlinear electron transport in ultrashort channel graphene devices. We observe this nonlinear response up to room temperature, with zero applied magnetic field, on a readily accessible oxide substrate. This makes the nanogap technology we utilize of great potential for achieving extremely scaled high-speed atomically thin devices.

KEYWORDS: Graphene, 2D Materials, Electronic Transport, Material Properties, Nanoscience

Author's signature: Mathias J. Boland

Date: November 27, 2016

PHYSICAL AND ELECTRONIC PROPERTIES OF NANOSCALE 2D MATERIALS

By
Mathias J. Boland

Director of Dissertation: Douglas R. Strachan

Director of Graduate Studies: Christopher Crawford

Date: November 27, 2016

To my parents.

ACKNOWLEDGMENTS

This work would not have been possible without the guidance, support, and friendship of many people. I thank my advisor, Professor Doug Strachan, who has provided excellent support and guidance throughout my time as a graduate student. I have learned a great deal from him and discussions with him have always proved invaluable. I would like to thank my committee members, Professors Joe Brill, Kwok-Wai Ng, and Beth Guiton for always taking the time to provide me with useful feedback throughout my research. My lab partners provided me with continual support and friendship. Thank you to my current and past lab partners, including Patrick Hunley, Abhishek Sundararajan, Mohsen Nasseri, Javad Farrohki, and Armin Ansary. Thanks to all of my friends and fellow graduate students, who have made this journey much more enjoyable, especially Jon D'Emidio, John Gruenewald, and Kyle McCarthy. Finally I would like to thank my family for their continued love and support in all of my endeavors. Thank you Mom, Dad, Francesca, Josephine, and Nathaniel for always being there.

TABLE OF CONTENTS

Acknowledgments iii

Table of Contents iv

List of Tables vii

List of Figures viii

Chapter 1 Background 1
1.1 Motivation 1
1.2 Properties of 2D Materials 2
1.2.1 Graphene Structure 2
1.2.2 Tight Binding Approach for Graphene's Electronic Structure . 4
1.2.3 Transition Metal Dichalcogenides 12
1.3 Electronic Transport 13
1.3.1 Field Effect Transistors 13
1.3.2 Diffusive Transport 14
1.3.3 Ballistic Transport 16
1.3.4 Electrical Contacts 17
1.3.5 Klein and Chiral Tunneling 18

Chapter 2 Experimental Methods 22
2.1 Atomic Force Microscopy 22
2.1.1 Basic Principles 22
2.1.2 AC Mode 22
2.1.3 Contact Mode 25
2.2 Scanning Electron Microscopy 28
2.2.1 SEM Emitter Types 30
2.2.2 Beam Sample Interaction 31
2.2.3 Electron Beam Lithography 35
2.3 Electrical Measurements 38
2.4 Raman Spectroscopy 38

Chapter 3 Striped Nanoscale Friction and Edge Rigidity of MoS_2 Layers . . 43
3.1 Introduction 43
3.2 Experimental Details 45
3.2.1 Sample Preparation 45
3.2.2 Lateral Force Microscopy Measurements 45
3.3 Results and Discussion 46
3.3.1 Elastic Response of MoS_2 Edges 46
3.3.2 Nanoscale Frictional Stripes 49

3.4 Conclusions 60

Chapter 4 Nonlinear Ballistic Transport in an Atomically Thin Material . . . 62
4.1 Introduction 62
4.2 Results and Discussion 63
4.3 Methods 78
4.3.1 Sample Fabrication 78
4.3.2 Nanogap Formation 78
4.3.3 Electrical Measurements 79
4.4 Gate Hysteresis 79
4.5 Nonlinear Ballistic Model 81
4.6 Inflection points 84
4.7 Gate Coupling Estimate 84
4.8 Detailed Comparison of Nonlinear Transport Between Experiments and Theory 87
4.9 Transmission Through Device, Contact Resistance, and Discussion on Phase Coherent Effects 92
4.9.1 Effective Transmission Through Device 92
4.9.2 Contact and Series Resistances 93
4.9.3 Discussion on Phase Coherent Effects 95
4.10 Conclusions 97

Chapter 5 Electrical Coupling Between Low Dimensional Nanoscale Materials 98
5.1 Introduction 98
5.2 Electrical Contacts 98
5.2.1 Momentum Conservation at Electrode Interfaces 100
5.3 Transport Between Carbon Nanotubes and Graphene 102

Appendix A Electron Beam Lithography 105
A.1 Silicon Wafer Preparation 105
A.2 2D Material Preparation 106
A.3 Lithography 107
A.4 Development 108
A.5 Overlay Patterns 109

Appendix B Lateral Force Microscopy Calibration 111

Appendix C Experimental Determination of Field Effect Mobility 112

References 114

Vita 126
Education 126
Professional Experience 126
Publications 126
Contributed Talks 127

Poster Presentations 127

LIST OF TABLES

1.1 Graphene Tight Binding Parameters 12
1.2 Mobilities for Selected Materials 15

2.1 Comparison of Electron Emitter Types 31

A.1 Sample EBL Parameters 108

LIST OF FIGURES

1.1 Graphene Lattice 3
1.2 Graphene Reciprocal Lattice 6
1.3 Graphene Dispersion Relation 10
1.4 Contour Plots of Graphene Dispersion Relation 11
1.5 Transition Metal Dichalcogenide Structure 13
1.6 Typical Graphene Field Effect Transistor Geometry 14
1.7 Graphene Tunneling Behavior 20

2.1 AFM Schematic 23
2.2 Lennard-Jones Potential 24
2.3 AFM Force Curve 27
2.4 Lateral Force Microscopy Signal 29
2.5 Schematic Illustration of a Scanning Electron Microscope 32
2.6 Schematic Illustration of the Electron-Sample Interaction in a SEM . . . 33
2.7 Schematic of Electron Beam Lithography Process 37
2.8 Comparison of Raman $2D$ Spectra for Varying Graphene Thicknesses . . 41

3.1 LFM of a single layer MoS_2 step edge 48
3.2 Periodic frictional stripes 51
3.3 Comparison of LFM scans taken at a range of scan speeds 52
3.4 Independence of oscillation wavelength on LFM probe adhesion 53
3.5 Comparison of lateral force arising from the stripe features for various loads and scan rates with the same LFM probe 54
3.6 LFM images showing the effects of varying the scan angle on MoS_2 frictional features 56
3.7 AFM and LFM images showing frictional features at various locations on a MoS_2 flake 57

4.1 Overview and fabrication of an ultra-short channel graphene field effect transistor (GFET) 64
4.2 Nonlinear conductance of an ultra-short GFET. 67
4.3 Ultra-short channel GFET ballistic model. 71
4.4 Quantitative Comparison Between Inflection Points of Ultra-Short GFET and the Ballistic Theory. 74
4.5 Quantitative Comparison Between Nonlinear Response of Ultra-Short GFET and the Ballistic Theory. 75
4.6 Hysteresis of low-bias behavior of samples. 80
4.7 Quantitative comparison between nonlinear response of ultra-short GFET at 77 K and ballistic theory 89
4.8 Quantitative comparison between nonlinear response of ultra-short GFET at 77 K and ballistic theory (continued) 90

4.9 Quantitative comparison between nonlinear response of ultra-short GFET at 293 K and ballistic theory . . . 91
4.10 Effective device transmission of the ultra-short single-layer device in Fig. 4.1 . . . 93

5.1 Schematic Illustration of Electron Transfer From a Metallic Electrode to an Atomically Thin Material . . . 99
5.2 Schematic Illustration of Electron Transfer in a Graphene-Graphene Contact 101
5.3 Scanning Electron Microscopy Image of Graphene with Etch Tracks . . . 103
5.4 Four Probe STM . . . 104
5.5 Preliminary Scanning Tunneling Microscopy Images of CNTs on Graphene 104

A.1 Silicon Wafer . . . 106

Chapter 1 Background

1.1 Motivation

Since the creation of the first transistor by Bardeen, Brattain, and Shockley in 1947 [1], there has been a continual push towards scaling electrical components down in size. As the size scale approaches the size of the constituent atoms, quantum mechanical effects become dominant. The isolation of two dimensional materials has resulted in a surge of research interest in the diverse physical and electronic properties realized in these reduced dimensional materials. Since the isolation of graphene by Geim *et al.* [2], the number of atomically-thin materials being researched has grown to include electrical insulators (hexagonal boron nitride), semiconductors (transition metal dichalcogendes (TMDs) such as MoS_2 and WSe_2), and semimetals (graphene). The focus of much of this research has been on the properties of these materials when the lateral dimensions are >100 nm [3]. The properties in the <100 nm regime remain more elusive [4]. In this work we focus on electrical and physical interactions in this regime.

Chapter 1 presents an introduction to properties of 2D materials that are relevant to this work. Chapter 2 provides a background of experimental equipment and techniques used in this work. In Chapter 3 we investigate nanoscale frictional and elastic properties of the 2D material MoS_2 using lateral force microscopy [5]. In Chapter 4 we fabricate sub-20 nm scale graphene transistors and show evidence for nonlinear ballistic transport [6]. Chapter 5 presents a discussion of ongoing work related to the electrical coupling between nanoscale materials.

1.2 Properties of 2D Materials

1.2.1 Graphene Structure

Graphene is a two dimensional sheet of carbon atoms arranged in a honeycomb pattern [3] as shown in Figure 1.1. This structure is formed from a hexagonal lattice with two atoms per unit cell, labeled A and B in Figure 1.1. To see the origin of this structure, we look at bonding between carbon atoms. Carbon atoms have 6 electrons, which in isolation configure to $1s^2 2s^2 2p^2$. The $1s^2$ electrons are close to the nucleus, and thus do not play a role in binding. The four outer electrons, $2s^2$ and $2p^2$, are responsible for the chemical bonds in carbon materials. When binding with other carbon atoms, these orbitals tend to hybridize, with sp^1 hybridization found in acetylene (C_2H_2), sp^2 orbitals found in graphene, carbon nanotubes, fullerenes, and aromatic rings (benzene), or sp^3 orbitals formed in diamond.

Hybridized Orbitals

Hybridization takes place as follows. In carbon's ground state, there are two electrons in the 1s orbital (1 spin up and 1 spin down), and two electrons in the 2s orbital. The remaining two electrons are in the 2p orbitals which are ~ 4 eV higher in energy than the 2s orbitals. There is one electron each in the $2p_x$ and $2p_y$ states, leaving the $2p_z$ state empty. When carbon atoms are brought close together, it becomes energetically favorable for one of the 2s electrons to become excited to the $2p_z$ state. When the atoms bond, the 2s state forms a quantum superposition with n of the 2p states, resulting in $n + 1$ degenerate sp^n hybridized orbitals. The resulting covalent bonds save more than the ~ 4 eV energy cost of promoting the 2s electron to 2p.

The sp^2 hybridized orbitals in graphene result in 3 filled sp^2 σ-bonds in plane, and a half filled, out of plane π-bond formed between the p_z electrons. The sp^2 orbitals

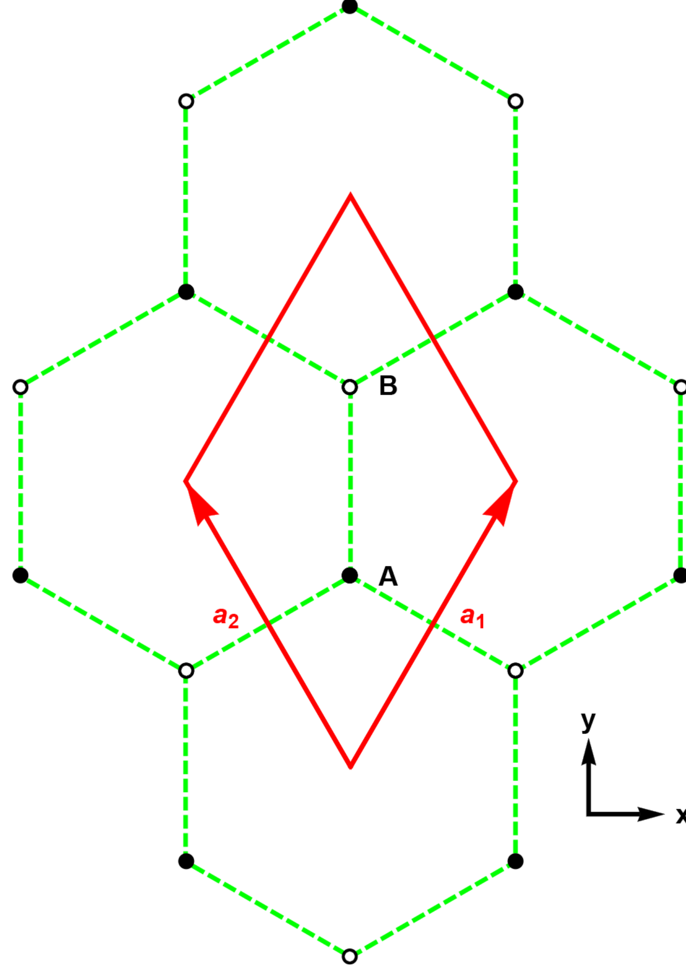

Figure 1.1: Schematic of graphene's real space lattice. The red diamond is graphene's primitive unit cell, $\mathbf{a}_1$ and $\mathbf{a}_2$ are the lattice vectors. A (filled circles) and B (hollow circles) denote the two atoms in graphene's basis.

are a superposition of the 2s, 2p$_x$, and 2p$_y$ wavefunctions:

$$|\psi_{sp^2,i}\rangle = a_i\,|\psi_s\rangle + b_i\,|\psi_{p_x}\rangle + c_i\,|\psi_{p_y}\rangle\,, \qquad i = 1, 2, 3, \tag{1.1}$$

where $|\psi_{sp^2,i}\rangle$ is the hybridized wavefunction, $|\psi_s\rangle$, $|\psi_{p_x}\rangle$, $|\psi_{p_y}\rangle$ are the 2s, 2p$_x$ and 2p$_y$ wavefunctions, respectively, and a_i, b_i, and c_i are normalization constants. Since there are 3 wavefunctions with 3 normalization constants, a total of 9 are required. Six of these can be found by imposing orthonormality on the wavefunctions:

$$\langle\psi_{sp^2,i}|\psi_{sp^2,j}\rangle = \delta_{ij}, \tag{1.2}$$

where δ_{ij} is the Kronecker Delta. We additionally require the contribution from the 2s wavefunctions to have equal strength, giving $a_1 = a_2 = a_3 = a$. Finally, we choose one of the hybridized wavefunction to point in the x-direction, giving $c_1 = 0$. These conditions yield

$$\langle \psi_{sp^2,1} | \psi_{sp^2,1} \rangle = a^2 + b_1^2 = 1, \tag{1.3a}$$

$$\langle \psi_{sp^2,2} | \psi_{sp^2,2} \rangle = a^2 + b_2^2 + c_2^2 = 1, \tag{1.3b}$$

$$\langle \psi_{sp^2,3} | \psi_{sp^2,3} \rangle = a^2 + b_3^2 + c_3^2 = 1, \tag{1.3c}$$

$$\langle \psi_{sp^2,1} | \psi_{sp^2,2} \rangle = a^2 + b_1 b_2 = 0, \tag{1.3d}$$

$$\langle \psi_{sp^2,1} | \psi_{sp^2,3} \rangle = a^2 + b_1 b_3 = 0, \tag{1.3e}$$

$$\langle \psi_{sp^2,2} | \psi_{sp^2,3} \rangle = a^2 + b_2 b_3 + c_2 c_3 = 0. \tag{1.3f}$$

Solving these simultaneous equations for a, b_i, and c_i and substituting into Equation (1.1) yields the three sp^2 wavefunctions:

$$|\psi_{sp^2,1}\rangle = \frac{1}{\sqrt{3}} |\psi_s\rangle + \sqrt{\frac{2}{3}} |\psi_{p_x}\rangle , \tag{1.4a}$$

$$|\psi_{sp^2,2}\rangle = \frac{1}{\sqrt{3}} |\psi_s\rangle - \frac{1}{\sqrt{6}} |\psi_{p_x}\rangle + \frac{1}{\sqrt{2}} |\psi_{p_y}\rangle , \tag{1.4b}$$

$$|\psi_{sp^2,2}\rangle = \frac{1}{\sqrt{3}} |\psi_s\rangle - \frac{1}{\sqrt{6}} |\psi_{p_x}\rangle - \frac{1}{\sqrt{2}} |\psi_{p_y}\rangle . \tag{1.4c}$$

These wavefunctions lie in the xy-plane at 120° to one another. The remaining half filled p$_z$ orbitals form a delocalized π-bond, responsible for low energy electron transport.

1.2.2 Tight Binding Approach for Graphene's Electronic Structure

Graphene's honeycomb lattice structure results in a linear low energy electronic dispersion, rather than the more typical quadratic one. This can be seen through a tight binding calculation of graphene's band structure for the π and π^* bands [7].

The electron states in a periodic crystal are of the form

$$\psi_{n\mathbf{k}}(\mathbf{r}) = \sum_{i,l} c_{n\mathbf{k}il} \chi_{\mathbf{k}il}(\mathbf{r}), \tag{1.5}$$

where the Bloch states, $\chi_{\mathbf{k}il}(\mathbf{r})$, follow Bloch's theorem

$$\chi_{\mathbf{k}il}(\mathbf{r} + \mathbf{R}) = e^{\mathbf{ik\cdot R}} \chi_{\mathbf{k}il}(\mathbf{r}), \tag{1.6}$$

with lattice vectors $\mathbf{R}$, wavevector $\mathbf{k}$, coefficient $c_{\mathbf{k}il}$, and band index n [8, chapter 8]. The subscript i labels atoms in the basis, and l labels atomic orbitals. These Bloch states can be written as linear combinations of atomic orbitals, $\phi_l(\mathbf{r} - \mathbf{t}_i - \mathbf{R})$,

$$\chi_{\mathbf{k}il}(\mathbf{r}) = \frac{1}{\sqrt{N}} \sum_{\mathbf{R}} e^{\mathbf{ik\cdot R}} \phi_l(\mathbf{r} - \mathbf{t}_i - \mathbf{R}), \tag{1.7}$$

where N is the number of lattice sites and $\mathbf{t}_i$ are the basis vector to the ith atom in the unit cell. For the case of graphene the half filled p_z orbitals are responsible for graphene's low energy transport, so $\phi_l = \phi_{p_z}$ and the index l can be dropped. Combining Equations 1.5 and 1.7 results in

$$\psi_{n\mathbf{k}}(\mathbf{r}) = \frac{1}{\sqrt{N}} \sum_{i} c_{n\mathbf{k}i} \sum_{\mathbf{R}} e^{\mathbf{ik\cdot R}} \phi(\mathbf{r} - \mathbf{t}_i - \mathbf{R}). \tag{1.8}$$

The single particle Schrödinger equation is then $H\psi_{n\mathbf{k}}(\mathbf{r}) = E_{n\mathbf{k}}\psi_{n\mathbf{k}}(\mathbf{r})$, with Hamiltonian H, and energy $E_{n\mathbf{k}}$. The coefficients $c_{\mathbf{k}i}$ are found with the variational method by minimizing the expectation value of the energy.

$$\begin{aligned} &\langle \psi_{ni\mathbf{k}}(\mathbf{r}) | H | \psi_{nj\mathbf{k}}(\mathbf{r}) \rangle = E_{n\mathbf{k}} \langle \psi_{ni\mathbf{k}}(\mathbf{r}) | \psi_{nj\mathbf{k}}(\mathbf{r}) \rangle \Rightarrow \\ &\sum_{ij} (\langle \chi_{i\mathbf{k}}(\mathbf{r}) | H | \chi_{j\mathbf{k}}(\mathbf{r}) \rangle - E_{n\mathbf{k}} \langle \chi_{i\mathbf{k}}(\mathbf{r}) | \chi_{j\mathbf{k}}(\mathbf{r}) \rangle) c_{n\mathbf{k}j} = 0. \end{aligned} \tag{1.9}$$

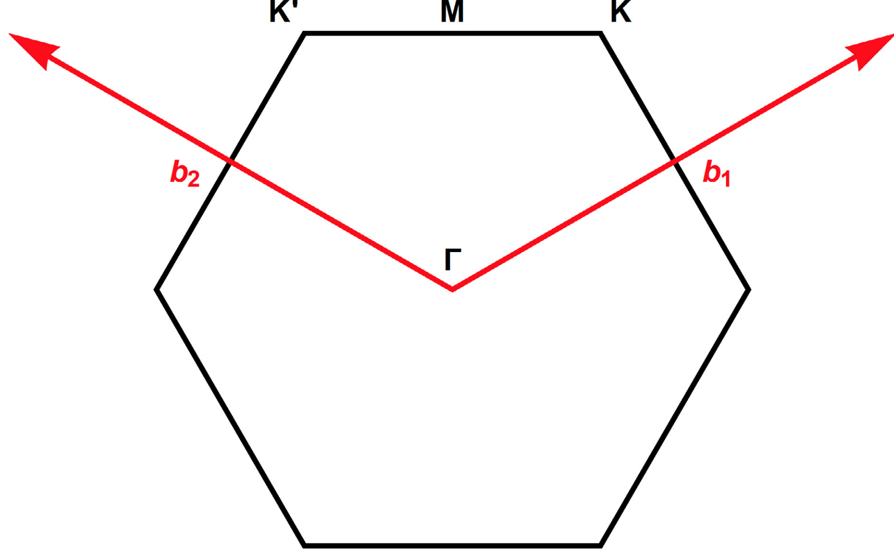

Figure 1.2: Schematic representation of graphene's reciprocal lattice. The red arrows b_1 and b_2 are the reciprocal lattice vectors. High symmetry points of the brillouin zone are labeled Γ, K, K', and M.

The term $\langle\chi_{i\mathbf{k}}(\mathbf{r})|\chi_{j\mathbf{k}}(\mathbf{r})\rangle$ becomes

$$\begin{aligned}\langle\chi_{i\mathbf{k}}(\mathbf{r})|\chi_{j\mathbf{k}}(\mathbf{r})\rangle &= \frac{1}{N}\sum_{\mathbf{R},\mathbf{R}'} e^{-\mathrm{i}\mathbf{k}\cdot\mathbf{R}} e^{\mathrm{i}\mathbf{k}\cdot\mathbf{R}'} \langle\phi(\mathbf{r}-\mathbf{t}_i-\mathbf{R})|\phi(\mathbf{r}-\mathbf{t}_j-\mathbf{R}')\rangle \\ &= \frac{1}{N}\sum_{\mathbf{R},\mathbf{R}'} e^{\mathrm{i}\mathbf{k}\cdot(\mathbf{R}'-\mathbf{R})} \langle\phi(\mathbf{r}'-\mathbf{t}_i)|\phi(\mathbf{r}'-\mathbf{t}_j-(\mathbf{R}'-\mathbf{R}))\rangle \\ &= \frac{1}{N} N\sum_{\mathbf{R}''} e^{\mathrm{i}\mathbf{k}\cdot\mathbf{R}''} \langle\phi(\mathbf{r}'-\mathbf{t}_i)|\phi(\mathbf{r}'-\mathbf{t}_j-\mathbf{R}'')\rangle \\ &= \sum_{\mathbf{R}} e^{\mathrm{i}\mathbf{k}\cdot\mathbf{R}} \langle\phi(\mathbf{r}'-\mathbf{t}_i)|\phi(\mathbf{r}'-\mathbf{t}_j-\mathbf{R})\rangle \\ &= S_{ij}(\mathbf{k}),\end{aligned} \tag{1.10}$$

where $\mathbf{r}' = \mathbf{r} - \mathbf{R}$ is used in the second line and $\mathbf{R}'' = \mathbf{R}' - \mathbf{R}$ is used in the third line. The sum over $\mathbf{R}$ results in a factor of N in the third line due to the lack of explicit $\mathbf{R}$ dependence. In the last line, $\mathbf{R}''$ is relabeled $\mathbf{R}$. $S_{ij}(\mathbf{k})$ are the overlap matrix elements, while the terms $\langle\phi(\mathbf{r}'-\mathbf{t}_i)|\phi(\mathbf{r}'-\mathbf{t}_j-\mathbf{R})\rangle$ are the overlap integrals. The overlap integrals are commonly used as a fitting parameter, rather than calculated. The onsite integrals are unity since the atomic wave functions are normalized. The nearest neighbor integral is labeled s_0, the next nearest neighbor integral is s_1, and

so on. The term $\langle\chi_{i\mathbf{k}}(\mathbf{r})|H|\chi_{j\mathbf{k}}(\mathbf{r})\rangle$ in (1.9) is,

$$\begin{aligned}
\langle\chi_{i\mathbf{k}}(\mathbf{r})|H|\chi_{j\mathbf{k}}(\mathbf{r})\rangle &= \frac{1}{N}\sum_{\mathbf{R},\mathbf{R}'} e^{-i\mathbf{k}\cdot\mathbf{R}}e^{i\mathbf{k}\cdot\mathbf{R}'}\langle\phi(\mathbf{r}-\mathbf{t}_i-\mathbf{R})|H|\phi(\mathbf{r}-\mathbf{t}_j-\mathbf{R}')\rangle \\
&= \frac{1}{N}\sum_{\mathbf{R},\mathbf{R}'} e^{i\mathbf{k}\cdot(\mathbf{R}'-\mathbf{R})}\langle\phi(\mathbf{r}'-\mathbf{t}_i)|H|\phi(\mathbf{r}'-\mathbf{t}_j-(\mathbf{R}'-\mathbf{R}))\rangle \\
&= \frac{1}{N}N\sum_{\mathbf{R}''} e^{i\mathbf{k}\cdot\mathbf{R}''}\langle\phi(\mathbf{r}'-\mathbf{t}_i)|H|\phi(\mathbf{r}'-\mathbf{t}_j-\mathbf{R}'')\rangle \qquad (1.11)\\
&= \sum_{\mathbf{R}} e^{i\mathbf{k}\cdot\mathbf{R}}\langle\phi(\mathbf{r}'-\mathbf{t}_i)|H|\phi(\mathbf{r}'-\mathbf{t}_j-\mathbf{R})\rangle \\
&= H_{ij}(\mathbf{k}),
\end{aligned}$$

with $H_{ij}(\mathbf{k})$ being the Hamiltonian matrix elements. When looking at equivalent orbitals on the same atom, the terms $\langle\phi(\mathbf{r}'-\mathbf{t}_i)|H|\phi(\mathbf{r}'-\mathbf{t}_j-\mathbf{R})\rangle$ gives the onsite energy, ϵ. For the case of nearest neighbor interactions with distance $\mathbf{d}_{nn}$, these terms gives the nearest neighbor hopping elements γ_0. In the case of graphene, $\epsilon = \epsilon_{2p}$, where ϵ_{2p} is the energy contributed by the p_z orbital. For graphene these have the form

$$\begin{aligned}
\langle\phi(\mathbf{r}'-\mathbf{t}_i)|H|\phi(\mathbf{r}'-\mathbf{t}_j-\mathbf{R})\rangle = \delta_{ij}\delta(\mathbf{R}=0)\epsilon_{2p} \\
+\,\delta((\mathbf{t}_i-\mathbf{t}_j-\mathbf{R})-\mathbf{d}_{nn})\gamma_{0ij} \\
+\,\delta((\mathbf{t}_i-\mathbf{t}_j-\mathbf{R})-\mathbf{d}_{nnn})\gamma_{1ij} \qquad (1.12)\\
+\,...+\delta((\mathbf{t}_i-\mathbf{t}_j-\mathbf{R})-\mathbf{d}_{n^m})\gamma_{mij},
\end{aligned}$$

with γ_0, γ_1, and γ_m being the hopping elements for nearest, next nearest, and mth nearest neighbors. The onsite and hopping energies are often treated as free parameters, rather than being calculated directly. Equation (1.9) now becomes

$$\sum_{ij}(H_{ij}(\mathbf{k})-E(\mathbf{k})S_{ij}(\mathbf{k}))=0, \qquad (1.13a)$$

$$\mathbf{H}(\mathbf{k})-E(\mathbf{k})\mathbf{S}(\mathbf{k})=0, \qquad (1.13b)$$

where $\mathbf{H}(\mathbf{k})$ is a matrix of the Hamiltonian matrix elements and $\mathbf{S}(\mathbf{k})$ is the overlap matrix. Nontrivial solutions are found when the determinant of (1.13b) equals zero:

$$|\mathbf{H}(\mathbf{k})-E(\mathbf{k})\mathbf{S}(\mathbf{k})|=0. \qquad (1.14)$$

The sum in Equation (1.13a), runs over the atoms in graphene's primitive unit cell. Graphene's real space lattice can be seen in Figure 1.1. There are two atoms in its primitive unit cell, labeled A and B, resulting in a 2×2 matrix for Equation (1.14).

$$\begin{vmatrix} H_{AA}(\mathbf{k}) - E(\mathbf{k})S_{AA}(\mathbf{k}) & H_{AB}(\mathbf{k}) - E(\mathbf{k})S_{AB}(\mathbf{k}) \\ H_{BA}(\mathbf{k}) - E(\mathbf{k})S_{BA}(\mathbf{k}) & H_{BB}(\mathbf{k}) - E(\mathbf{k})S_{BB}(\mathbf{k}) \end{vmatrix} = 0, \tag{1.15}$$

where H_{AA}, H_{BB}, S_{AA}, and S_{BB} correspond to matrix elements with interactions between only A and only B sites, while H_{AB}, H_{BA}, S_{AB}, and S_{AB} correspond to matrix elements between A and B sites. Since the carbon atoms at graphene's A and B sites are equivalent, and the Hamiltonian matrix is Hermitian, $H_{AA} = H_{BB}$, $S_{AA} = S_{BB}$, $H_{BA} = H^*_{AB}$, and $S_{BA} = S^*_{AB}$. This simplifies Equation 1.15 to

$$\begin{vmatrix} H_{AA}(\mathbf{k}) - E(\mathbf{k})S_{AA}(\mathbf{k}) & H_{AB}(\mathbf{k}) - E(\mathbf{k})S_{AB}(\mathbf{k}) \\ H^*_{AB}(\mathbf{k}) - E(\mathbf{k})S^*_{AB}(\mathbf{k}) & H_{AA}(\mathbf{k}) - E(\mathbf{k})S_{AA}(\mathbf{k}) \end{vmatrix} = 0. \tag{1.16}$$

Solving Equation 1.16 for $E(\mathbf{k})$ results in two energy eigenvalues,

$$\begin{aligned} E^{\pm}(\mathbf{k}) &= \frac{2E_1 - E_2 \pm \sqrt{(-2E_1 + E_2)^2 - 4E_3E_4}}{2E_4}, \\ E_1 &= H_{AA}S_{AA}, \\ E_2 &= H_{AB}S^*_{AB} + H^*_{AB}S_{AB}, \\ E_3 &= H^2_{AA} - |H_{AB}|^2, \\ E_4 &= S^2_{AA} - |S_{AB}|^2. \end{aligned} \tag{1.17}$$

The positive (negative) solution corresponding to the conduction (valence) band. We now find expressions for H_{AA}, S_{AA}, H_{AB}, and S_{AB} for the case of nearest and next nearest neighbor interactions. Graphene's two lattice vectors, shown in Figure 1.1 are given by

$$\mathbf{a}_1 = a_0 \left(\frac{\sqrt{3}}{2}, \frac{3}{2} \right), \tag{1.18a}$$

$$\mathbf{a}_2 = a_0 \left(-\frac{\sqrt{3}}{2}, \frac{3}{2} \right), \tag{1.18b}$$

where a_0 is graphene's nearest neighbor spacing. Since the nearest neighbors for A (B) sites are B (A) sites, these will correspond to H_{AB} (H_{BA}). A's nearest neighbors are located at $\mathbf{a}_{AB1} = \mathbf{a}_0$, $\mathbf{a}_{AB2} = -\mathbf{a}_1 + \mathbf{a}_0$, and $\mathbf{a}_{AB3} = \mathbf{a}_1 - \mathbf{a}_0$, where $\mathbf{a}_0 = a_0(0, 1)$. H_{AB} is then given by

$$\begin{aligned} H_{AB} &= \gamma_0(e^{\mathbf{ik}\cdot\mathbf{a}_0} + e^{\mathbf{ik}\cdot(-\mathbf{a}_1+\mathbf{a}_0)} + e^{\mathbf{ik}\cdot(\mathbf{a}_1-\mathbf{a}_0)}) \\ &= \gamma_0(e^{\mathbf{ik}\cdot\mathbf{a}_0} + 2\cos(\mathbf{k}\cdot(\mathbf{a}_0 - \mathbf{a}_1))). \end{aligned} \tag{1.19}$$

$H^*_{AB} = H_{BA}$ is given by

$$\begin{aligned} H^*_{AB} = H_{BA} &= \gamma_0(e^{-\mathbf{ik}\cdot\mathbf{a}_0} + e^{-\mathbf{ik}\cdot(-\mathbf{a}_1+\mathbf{a}_0)} + e^{-\mathbf{ik}\cdot(\mathbf{a}_1-\mathbf{a}_0)}) \\ &= \gamma_0(e^{-\mathbf{ik}\cdot\mathbf{a}_0} + 2\cos(\mathbf{k}\cdot(\mathbf{a}_0 - \mathbf{a}_1))). \end{aligned} \tag{1.20}$$

Similarly, the overlap matrix elements S_{AB} and $S^*_{AB} = S_{BA}$ are given by

$$\begin{aligned} S_{AB} &= s_0(e^{\mathbf{ik}\cdot\mathbf{a}_0} + e^{\mathbf{ik}\cdot(-\mathbf{a}_1+\mathbf{a}_0)} + e^{\mathbf{ik}\cdot(\mathbf{a}_1-\mathbf{a}_0)}) \\ &= s_0(e^{\mathbf{ik}\cdot\mathbf{a}_0} + 2\cos(\mathbf{k}\cdot(\mathbf{a}_0 - \mathbf{a}_1))). \end{aligned} \tag{1.21}$$

and

$$\begin{aligned} S^*_{AB} = S_{BA} &= s_0(e^{-\mathbf{ik}\cdot\mathbf{a}_0} + e^{-\mathbf{ik}\cdot(-\mathbf{a}_1+\mathbf{a}_0)} + e^{-\mathbf{ik}\cdot(\mathbf{a}_1-\mathbf{a}_0)}) \\ &= s_0(e^{-\mathbf{ik}\cdot\mathbf{a}_0} + 2\cos(\mathbf{k}\cdot(\mathbf{a}_0 - \mathbf{a}_1))). \end{aligned} \tag{1.22}$$

The elements H_{AA} and H_{BB} contain the onsite energies and the six next nearest neighbor interactions, resulting in,

$$\begin{aligned} H_{AA} = H_{BB} &= \epsilon_{2p} + \gamma_1(e^{\mathbf{ik}\cdot\mathbf{a}_1} + e^{\mathbf{ik}\cdot\mathbf{a}_2} + e^{\mathbf{ik}\cdot(\mathbf{a}_2-\mathbf{a}_1)} + e^{-\mathbf{ik}\cdot\mathbf{a}_1} + e^{-\mathbf{ik}\cdot\mathbf{a}_2} + e^{\mathbf{ik}\cdot(\mathbf{a}_1-\mathbf{a}_2)}) \\ &= \epsilon_{2p} + 2\gamma_1(\cos(\mathbf{k}\cdot\mathbf{a}_1) + \cos(\mathbf{k}\cdot\mathbf{a}_2) + \cos(\mathbf{k}\cdot(\mathbf{a}_2 - \mathbf{a}_1))). \end{aligned} \tag{1.23}$$

Similarly,

$$\begin{aligned} S_{AA} = S_{BB} &= 1 + s_1(e^{\mathbf{ik}\cdot\mathbf{a}_1} + e^{\mathbf{ik}\cdot\mathbf{a}_2} + e^{\mathbf{ik}\cdot(\mathbf{a}_2-\mathbf{a}_1)} + e^{-\mathbf{ik}\cdot\mathbf{a}_1} + e^{-\mathbf{ik}\cdot\mathbf{a}_2} + e^{\mathbf{ik}\cdot(\mathbf{a}_1-\mathbf{a}_2)}) \\ &= 1 + 2s_1(\cos(\mathbf{k}\cdot\mathbf{a}_1) + \cos(\mathbf{k}\cdot\mathbf{a}_2) + \cos(\mathbf{k}\cdot(\mathbf{a}_2 - \mathbf{a}_1))). \end{aligned} \tag{1.24}$$

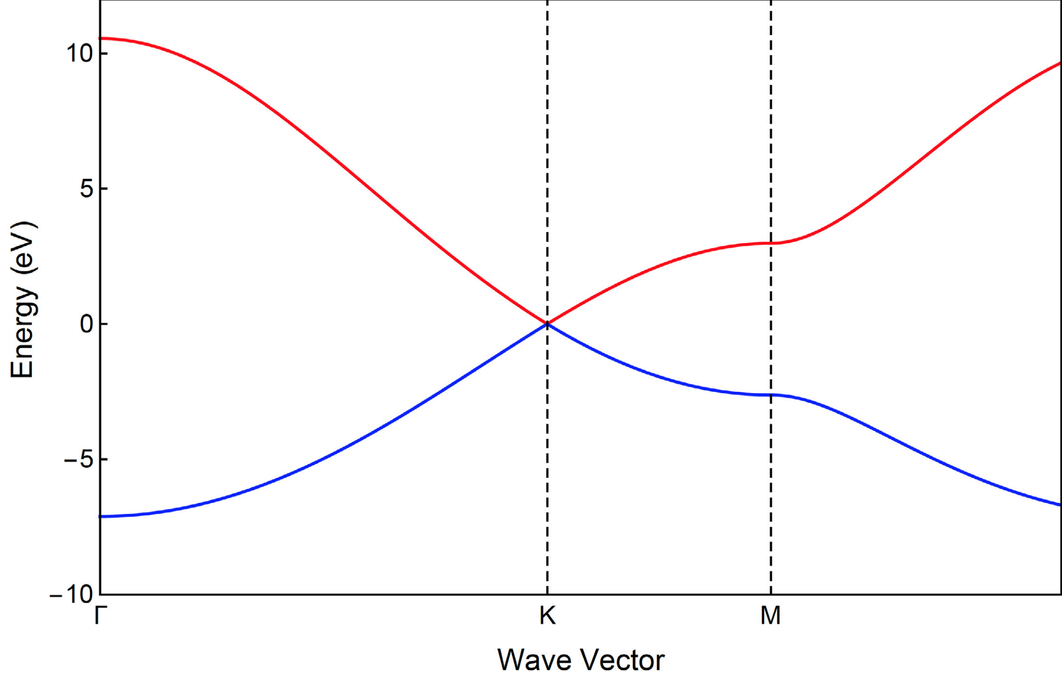

Figure 1.3: Plot of graphene's dispersion relation through high symmetry points, as calculated through the tight binding method with nearest and next nearest neighbors. Red corresponds to the π^* band and blue corresponds to the π band. The Fermi level is at 0 eV for intrinsic (undoped) graphene.

Inserting Equations (1.19)-(1.24) into Equation (1.17) results in an expression for graphene's dispersion relation. The results of these next nearest neighbor tight binding calculations are shown in Figures 1.3 and 1.4. These were calculated using the parameters shown in Table 1.1, taken from Ref. [7]. Of particular interest for electron transport is the linear behavior near the K points, also known as the Dirac points. The parabolic dispersion found in most semiconductors results in massive charge carriers. In contrast, graphene's linear dispersion near the K points results in massless charge carrier that follow the relativistic Dirac equation with a Fermi velocity of $v_F \sim 10^6$ m/s [9]. Near the K points, this dispersion can be approximated as,

$$E = \pm\hbar v_F \sqrt{k_x^2 + k_y^2}. \tag{1.25}$$

The valence and conduction bands meet at a point, resulting in a zero band gap semiconductor. This linear dispersion is responsible for a variety of phenomenon,

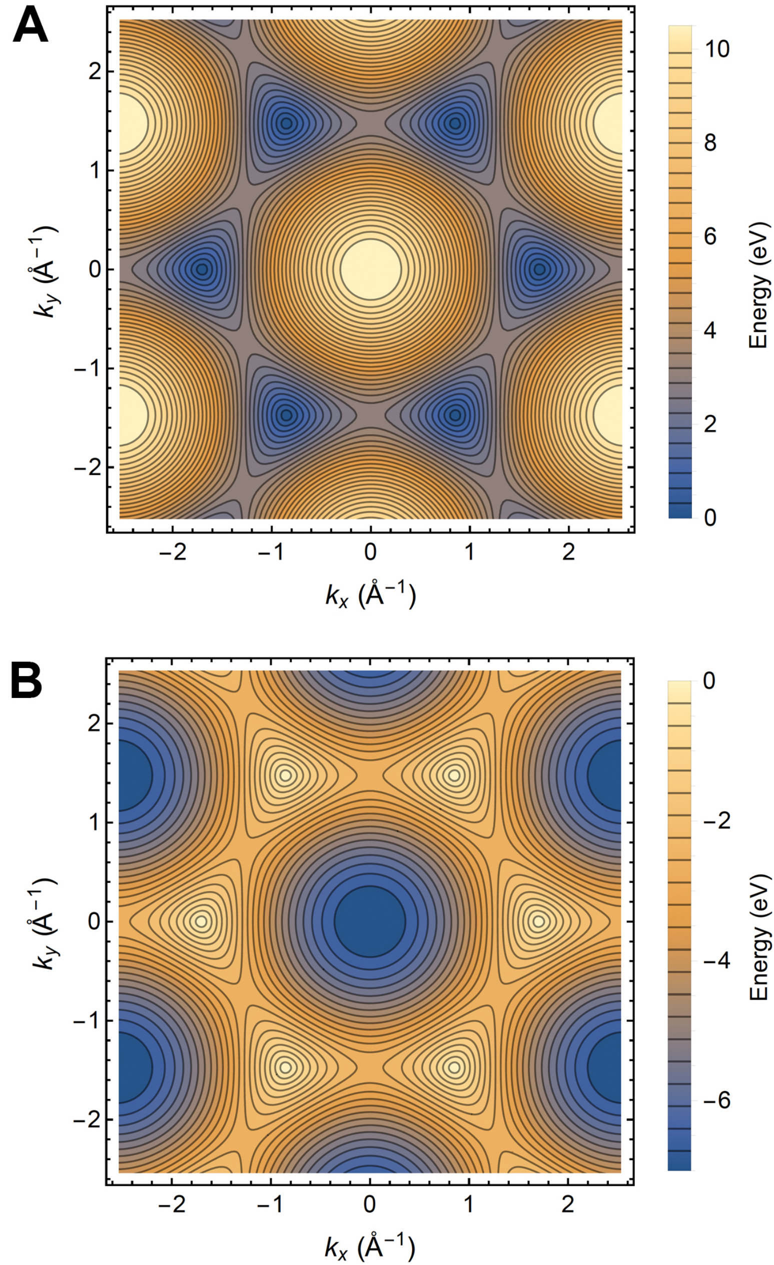

Figure 1.4: Contour plots of graphene's dispersion relation as calculated through the tight binding method with nearest and next nearest neighbors. A) shows the π^* band and B) shows the π band.

such as graphene's high carrier mobility and Klein tunneling, that is, the ability for charge carriers to tunnel through barriers with unity transmission [10].

In the case of bilayer graphene, coupling between layers results in a quadratic band

Table 1.1: Graphene Tight Binding Parameters

$\lvert\mathbf{a_1}\rvert$, $\lvert\mathbf{a_2}\rvert$	$\mathbf{a_0}$	$\epsilon_{\mathbf{2p}}$	$\gamma_{\mathbf{0}}$	$\gamma_{\mathbf{1}}$	$\mathbf{s_0}$	$\mathbf{s_1}$
2.46 Å	1.42 Å	-0.36 eV	-2.78 eV	-0.12 eV	0.106 eV	0.001 eV

touching at the K points. While still a zero band gap semiconductor, the massive charge carriers can drastically alter the transport properties compared to single layer graphene. One example is when charge carriers are incident upon a barrier. In this case bilayer graphene exhibits chiral tunneling [10], where normally incident charge carriers have a transmission of zero.

1.2.3 Transition Metal Dichalcogenides

The transition metal dichalcogenides (TMDs) are another class of 2D laminar materials which have recently garnered considerable interest. TMDs follow the chemical form MX_2, where M is transition metal, usually molybdenum (Mo) or tungsten (W), and X is an atom from the chalcogen group, usually sulphur (S), selenium (Se), or tellurium (Te). Unlike graphene, TMDs have a band gap, which makes them attractive for transistor applications where the band gap allows them to be turned off. Monolayer MoS_2 has a direct bandgap of $\sim$ 1.8 eV, while interlayer coupling in multilayers result in an indirect bandgap of decreasing energy down to 1.29 eV for bulk MoS_2 [11, 12]. In MoS_2, the Mo d-orbitals are principally responsible for conduction [13].

The general physical structure of TMDs is shown in Figure 1.5. Like graphite, TMDs have strong intralayer bonds. Unlike graphene, monolayer TMDs are three atoms thick, with a layer of M atoms sandwiched between two layers of X atoms. Interlayer coupling is due to van der Waals (vdW) interactions. This allows for the mechanical exfoliation of TMDs, similar to graphene. Additionally, the weak interlayer coupling allows layers to slide past one another, allowing for their widespread

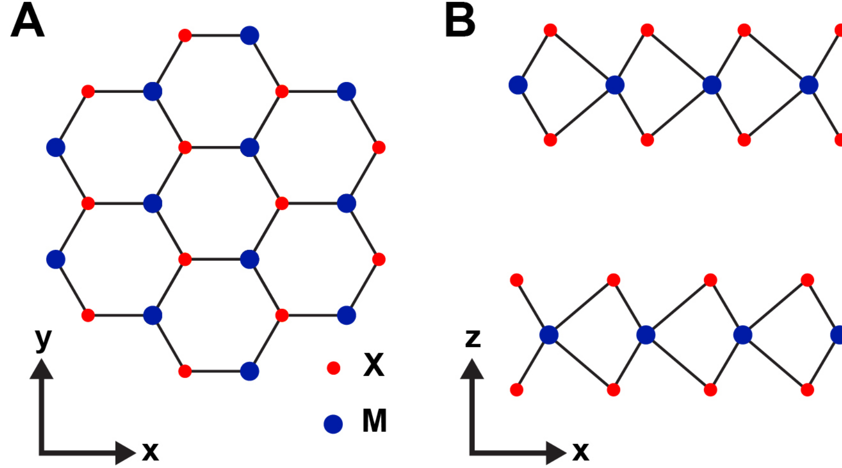

Figure 1.5: Schematic illustration of the crystal structure of transition metal dichalcogenides. Blue circles correspond to transition metal atoms and red circles correspond to chalcogen group atoms. (A) shows the structure in the xy-plane for a single layer, while (B) shows a cross section of the xz-plane for a bilayer.

use as dry lubricants [14].

1.3 Electronic Transport

1.3.1 Field Effect Transistors

One of the most widely used semiconductor device is the field effect transistor (FET). These transistors form the basis for most of the current computer chips manufactured today. FETs are three terminal devices consisting of a source, drain, and gate electrode as shown in Figure 1.6. The source and drain electrodes are used to apply a bias voltage across the semiconducting channel. The gate electrode is separated from the channel material with a dielectric layer. When a voltage is applied between the gate and the channel an electric field is formed between them. This in effect acts as a parallel plate capacitor, which allows the gate to control the charge, and thus the carrier density in the channel.

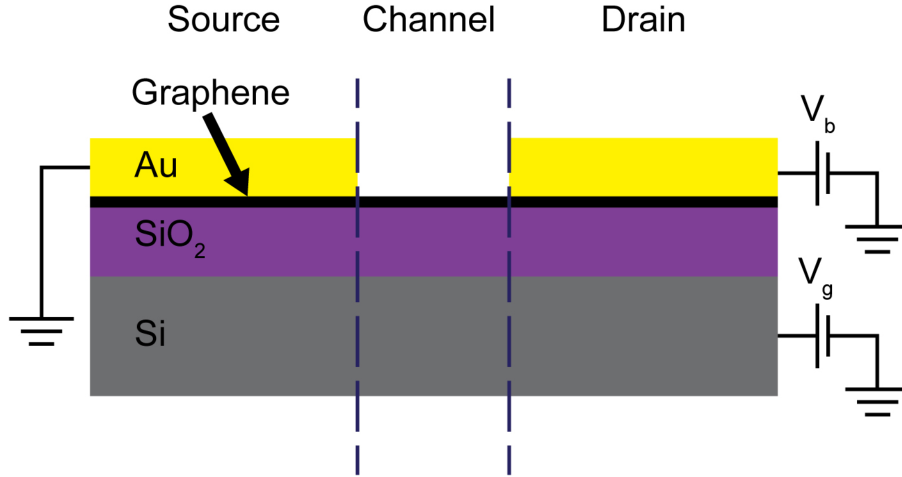

Figure 1.6: Schematic diagram of a typical graphene field effect transistor (GFET). A bias voltage is applied across the source and drain contacts, while a gate voltage is applied to the silicon backgate. An insulating SiO_2 layer separates the graphene channel from the backgate.

1.3.2 Diffusive Transport

With no applied field, conduction electrons in a metal travel with random thermal motion with average speed $\langle v \rangle$. When an electric field is applied, the electrons gain an additional drift velocity, v_d. As the electrons travel through the material, there is a finite distance they travel before being scattered given by

$$\lambda = \langle v \rangle \tau, \tag{1.26}$$

where τ is the mean scattering time. The average distance they travel is called the mean free path, λ. When the mean free path of the charge carriers is much shorter than the device dimensions, transport is said to be in the diffusive regime. Under these conditions scattering plays an important role in transport. When there are multiple scattering mechanisms, the Matthiessen rule can be used to find the effective mean scattering time. The Matthiessen rule is given by

$$\frac{1}{\tau} = \frac{1}{\tau_1} + \frac{1}{\tau_2} + \frac{1}{\tau_3} + \ldots, \tag{1.27}$$

where τ_1, τ_2, τ_3 are the mean scattering times for each scattering mechanism.

Table 1.2: Mobilities for Selected Materials

Material	**Electron Mobility, μ_e, (cm^2 V^{-1} s^{-1})**	**Hole Mobility, μ_h, (cm^2 V^{-1} s^{-1})**
Graphene, intrinsic	>100,000	>100,000
Graphene, on SiO_2	10,000-15,000	10,000-15,000
MoS_2, on PMMA	480	480
Silicon	1,450	500
Germanium	3,900	1,900
Gallium arsenide	8,000	400

Electron Mobility

An important parameter for electronic transport in semiconductors is the carrier mobility μ [15]. This is defined as the ratio of the carrier drift velocity v_d to the applied electric field E.

$$\mu = \frac{v_d}{E}. \tag{1.28}$$

The mobility of a material is related to its conductivity. Current density J is given by

$$J = \rho v_d, \tag{1.29}$$

where ρ is the charge carrier density, and v_d is the drift velocity. Charge density can be written as

$$\rho = ne + pe, \tag{1.30}$$

where e is the electron charge, n is the electron density, and p is the hole density. The rate of change of the average velocity of the charge carriers in an applied electric field E is

$$\frac{\mathrm{d}v_d}{\mathrm{d}t} = \frac{eE}{m^*} + \frac{v_d}{\tau}, \tag{1.31}$$

where m^* is the effective carrier mass and τ is the mean scattering time. The term eE/m^* is due to the electric field and v_d/τ is due to scattering. This rate should be

zero in the steady state, giving

$$v_d = -\frac{\tau e}{m^*} E. \tag{1.32}$$

Combining Equations (1.29), (1.30), and (1.32) yields,

$$J = (n + p)\frac{e^2 \tau}{m^*} E. \tag{1.33}$$

Conductivity σ is defined as $\sigma = J/E$, so we have

$$\sigma = (n + p)\frac{e^2 \tau}{m^*}. \tag{1.34}$$

Combining Equations (1.28) and (1.32) gives an alternate expression for μ:

$$\mu = -\frac{\tau e}{m^*}. \tag{1.35}$$

From Equations (1.34) and (1.35), we see that mobility is related to conductivity by

$$\sigma = n\mu_e e + p\mu_h e, \tag{1.36}$$

where μ_e is the mobility of electrons and μ_h is the mobility of holes. Table 1.2 shows the carrier mobility of selected materials. Graphene's high intrinsic mobility makes it an attractive choice for electronic applications requiring high speed switching.

1.3.3 Ballistic Transport

In contrast to the diffusive case, when the device scale approaches the mean free path length, coherent effects become dominant. The Landauer-Büttiker formalism can be used to describe transport under these circumstances [16]. Each transverse mode contributes a conductance quantum, $G_0 = \frac{2e^2}{h} \approx 7.75 \times 10^{-5}$ S. Ballistic current through a channel with $M(E)$ modes is found with,

$$I = \frac{2e^2}{h} \int_{-\infty}^{\infty} M(E)[f_S(E) - f_D(E)] \, \mathrm{d}E, \tag{1.37}$$

where $f_S(E)$ and $f_D(E)$ are the Fermi distributions in the source and drain.

1.3.4 Electrical Contacts

The interface between two materials, for example a metal-semiconductor junction, is associated with an increased resistance, known as a contact resistance. When a metal and a semiconductor are brought together, the bands of the semiconductor will bend, resulting in an ohmic (non-rectifying) type contact or a Schottky (rectifying) type contact [17]. Based on a simple band model, the height of the Schottky barrier between a metal and semiconductor can be predicted based on the Schottky-Mott rule

$$\Phi_{Bn} = \Phi_{\mathrm{m}} - \chi_{\mathrm{s}}, \tag{1.38}$$

where Φ_{Bn} is the Schottky barrier height, Φ_{m} is the metal work function, and χ_{s} is the semiconductor electron affinity [18]. Based on Equation (1.38), ohmic contacts exist when $\Phi_{\mathrm{m}} < \chi_{\mathrm{s}}$, while a Schottky barrier will exist when $\Phi_{\mathrm{m}} > \chi_{\mathrm{s}}$. This simplified approach often does not hold with materials showing Schottky barriers even when the Schottky-Mott rule predicts an ohmic contact. In many systems, this failure of Equation (1.38) is attributed to Fermi level pinning due to metal induced gap states (MIGS) [18, 19]. At the surface of a semiconductor there exist virtual gap states (VGS), which are Bloch wavefunctions with complex wavevectors located in the bulk band gap. Virtual gap states are not normalizable, and thus virtual, in the bulk, but are normalizable, and thus correspond to real states when the wavefunctions exponentially decay. At a metal-semiconductor interface the metal's wavefunctions overlap into the semiconductor. This results in an exponential decay of the metal's states around the semiconductor's Fermi level in its band gap. This forms a continuum of MIGS in the semiconductor from the VGS. This continuum of states in the band gap acts as a metal with the same Fermi level as the semiconductor. Thus the Fermi level is 'pinned' to the Fermi level of the semiconductor. This results in a Schottky barrier height equal to the energy difference between the semiconductor conduction band and the Fermi level [19].

1.3.5 Klein and Chiral Tunneling

Due to graphene's Dirac-like dispersion relationship, electrons in graphene can tunnel through normally incident potential barriers with perfect transmission, rather than with the usual exponential decay, in a process called Klein tunneling [10]. In bernal stacked bilayer graphene, the addition of a single atomic layer results in chiral tunneling, where normally incident electrons have a transmission probability of zero. These stark differences can result in distinct transport behavior between devices made with single and bilayer graphene.

The difference in transmission behavior of single layer graphene compared to bilayer graphene is due to differences of their pseudospin. Graphene's low energy charge carriers obey the Dirac equation,

$$-\mathrm{i}\hbar v_F(\sigma \cdot \nabla)\psi = E\psi \tag{1.39}$$

with Fermi velocity, v_F, of $\sim 10^6\,\mathrm{m\,s^{-1}}$ and pseudospin operator, $\sigma = (\sigma_x, \sigma_y)$, with Pauli matrices σ_x and σ_y. For single layer graphene, the two pseudospin components correspond to electrons occupying the A or B sites, rather than the electron spin occupying an up or down state. In the case of bilayer graphene, the bands split into four quadratic bands, with one of the conduction bands touching one of the valence bands at the K-points, and the other conduction (valence) band shifted up (down) by $\sim 0.39\,\mathrm{eV}$. For this section we only consider the two touching bands, which are responsible for low energy transport. In this case, the two components of the pseudospin correspond to the B-site on the upper layer and the A-site on the lower layer [20]. Near the K-point, single layer graphene's nearest neighbor tight binding Hamiltonian can be written as

$$H_{slg} = v_F \begin{pmatrix} 0 & p_x - \mathrm{i}p_y \\ p_x + \mathrm{i}p_y & 0 \end{pmatrix}. \tag{1.40}$$

Likewise, bilayer graphene's Hamiltonian can be written as

$$H_{blg} = \frac{-1}{2m^*} \begin{pmatrix} 0 & (p_x - \mathrm{i}p_y)^2 \\ (p_x + \mathrm{i}p_y)^2 & 0 \end{pmatrix}, \tag{1.41}$$

with effective electron mass, m^* [20]. Equations (1.40) and (1.41) act on the two component spinors

$$|\psi^{\pm}_{slg}\rangle = \frac{1}{\sqrt{2}} \begin{pmatrix} \pm e^{-\mathrm{i}\phi} \\ 1 \end{pmatrix}, \tag{1.42a}$$

$$|\psi^{\pm}_{blg}\rangle = \frac{1}{\sqrt{2}} \begin{pmatrix} \pm e^{-2\mathrm{i}\phi} \\ 1 \end{pmatrix}, \tag{1.42b}$$

where the plus and minus signs correspond to the two energy states, and $\phi = \arg(k_x + \mathrm{i}k_y)$ indicates the direction of the wavevector k. To find a relationship between the direction of the pseudospin and the direction of the wavevector, we find the polarization vector [20]

$$\mathbf{P} = \begin{pmatrix} \langle\psi|\sigma_x|\psi\rangle \\ \langle\psi|\sigma_y|\psi\rangle \\ \langle\psi|\sigma_z|\psi\rangle \end{pmatrix}, \tag{1.43}$$

where σ_x, σ_y, and σ_z are the Pauli matrices. Applying Equation (1.43) to the wavefunctions in Equations (1.42a) and (1.42b) results in

$$\mathbf{P}^{\pm}_{slg} = \pm \begin{pmatrix} \cos\phi \\ \sin\phi \\ 0 \end{pmatrix}, \tag{1.44a}$$

$$\mathbf{P}^{\pm}_{blg} = \pm \begin{pmatrix} \cos 2\phi \\ \sin 2\phi \\ 0 \end{pmatrix}, \tag{1.44b}$$

where the plus and minus signs correspond to electrons and holes, respectively. Equation (1.44a) indicates that the pseudospin for single layer graphene is confined to the

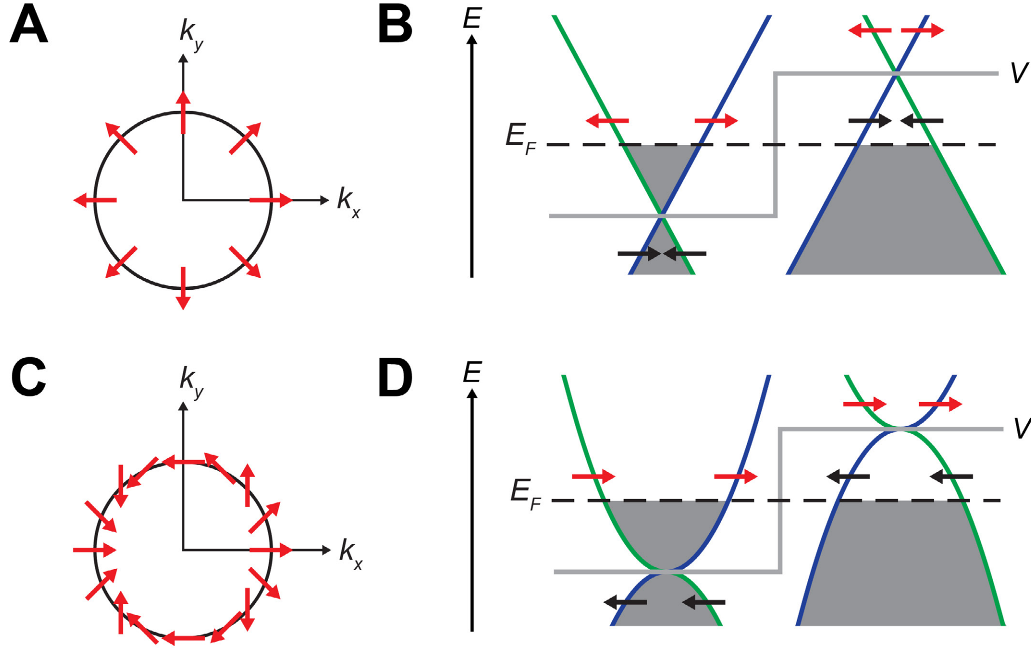

Figure 1.7: Graphene Tunneling Behavior. (A) Direction in k-space of the pseudospin vector for electron states near the K-point in single layer graphene. Hole states have opposite pseudospin direction. (B) Band skematic of single layer graphene near a potential barrier, V. States with group velocities moving rightward (leftward) are denoted by blue (green) lines. The pseudospin direction of electron (hole) states are indicated by red (black) arrows. On the left side of the barrier, the Fermi level E_F is in the conduction band, so electron states are responsible for transport. On the right side of the barrier, hole states are responsible for conduction. The pseudospin of rightward moving electronstate on the left side of the barrier matches the pseudospin of the corresponding rightward moving hole state on the right side of the barrier. This leads to perfect transmission through the barrier. (C) Same as (A), but for bilayer graphene. The pseudospin vector makes two full rotations around the K-point. (D) Same as (B), but for bilayer graphene. In contrast to the linear dispersion of single layer graphene, bilayer graphene has a parabolic dispersion. In this case the pseudospins in adjacent states are opposite, so there are no available states. This leads to perfect reflection at the barrier.

k_x-k_y plane, and is locked so that it is always parallel to the k-vector for electrons (see Figure 1.7A) and anti-parallel to the k-vector for holes. Note that this relationship is reversed at K'. In bilayer graphene, $\phi \to 2\phi$, so the pseudospin makes two revolutions as the k-vector is rotated around the K point once, as shown in Figure 1.7C. This difference in pseudospin is key to the transport behavior at potential barriers. As

illustrated in Figure 1.7B, the matching of pseudospin in single layer graphene allows for perfect transmission through barriers for normally incident electrons. The bilayer case, illustrated in Figure 1.7D, has no matching pseudospin in the barrier, resulting in nearly zero transmission for normally incident electrons. If the barrier is narrow compared to the Fermi wavelength, there can be transmission in the bilayer case due to evanescent modes.

Copyright© Mathias J. Boland, 2016.

Chapter 2 Experimental Methods

2.1 Atomic Force Microscopy

Since its invention by Binning [21] in 1986, the Atomic Force Microscope (AFM) has become a standard tool used to probe the nanoscale features of materials. A wide range of associated techniques have arisen, giving the ability to probe an array of properties including: topography, force, friction, electrostatic and magnetic force gradients, surface potential, work function, charge, piezoelectric properties, surface capacitance, local resistivity, and local magnetic fields [22].

2.1.1 Basic Principles

Atomic Force Microscopy works by scanning an atomically sharp probe located on the end of a cantilever over the surface of a sample. A laser, or columnized light from a superluminescent diode (SLD), is reflected off the back surface of the cantilever and onto a photosensitive detector (PSD) as illustrated in Figure 2.1. This 'optical lever' causes small changes in cantilever angle to result in large changes of laser position on the PSD allowing for very sensitive height measurements. The cantilever height is precisely controlled by a z-piezo stack. Depending on the imaging mode, a variety of parameters are held constant under feedback. In the case of non-contact mode the cantilever amplitude is usually held fixed, while in the case of contact mode, it is usually the deflection that is held fixed. An image is then formed by raster scanning the probe across the sample using a set of xy-piezo stacks.

2.1.2 AC Mode

In AC mode, the probe is oscillated near its resonant frequency and held a small distance above the sample, rather than being dragged across the sample. Feedback

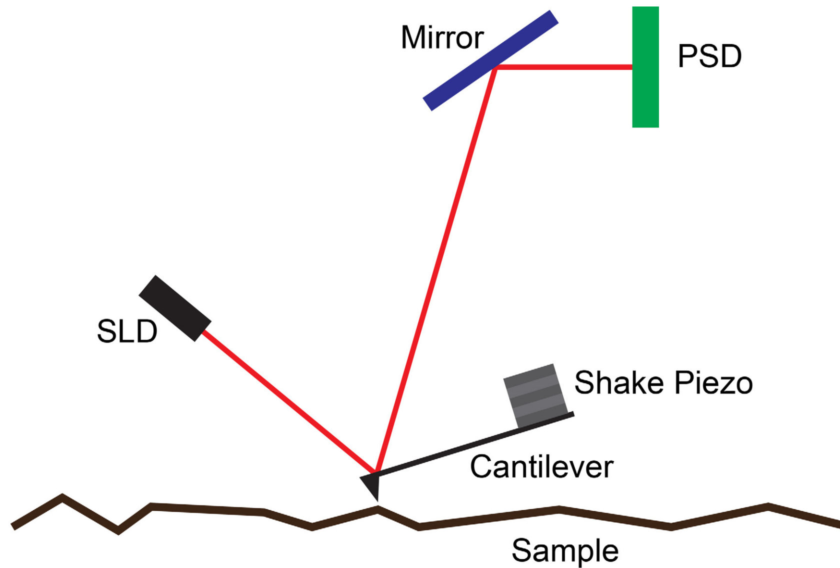

Figure 2.1: Schematic illustration of an atomic force microscope. Small deflections of the cantilever result in large deflections on the PSD due to the optical lever effect. The cantilever, SLD, mirror, and PSD are all rigidly attached to a z-piezo (not shown), so that changes in z-position do not effect the optical path.

is usually maintained on the oscillation amplitude measured by the PSD by raising or lowering the cantilever with the z-piezo. The amplitude of a driven cantilever is dependent on the force gradient acting on it. By maintaining a fixed amplitude, the sample-probe distance is kept constant, and the topography is deduced based on the z-piezo position. This requires that the potential between the probe and surface does not vary much across the sample. This can be monitored with the phase difference between the sinusoidal driving force and the measured cantilever motion. The sign of the phase shift indicates whether attractive of repulsive force gradients are dominating, so changes in the phase can indicate changes in the probe-sample interaction.

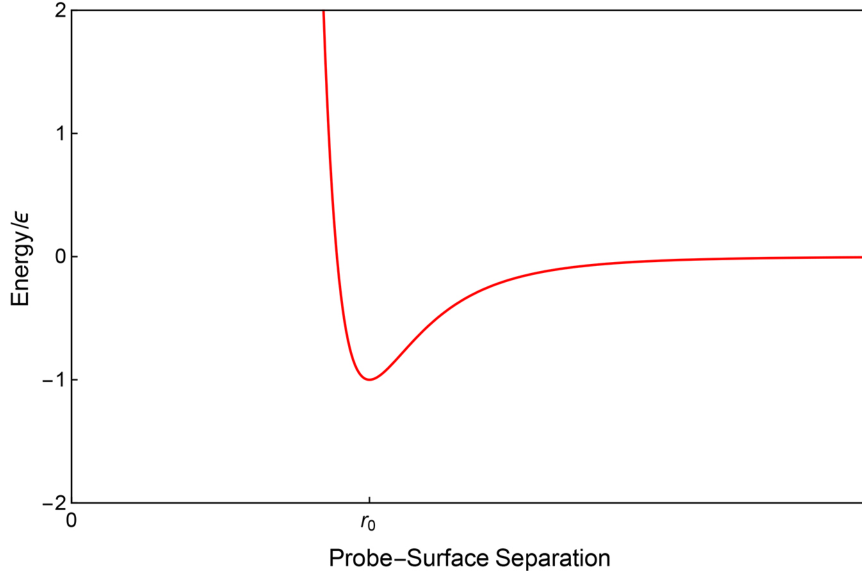

Figure 2.2: Lennard-Jones potential due to Van der Waals interactions between an AFM probe and sample. r_0 is the equilibrium separation between the probe and sample. For separations greater than this point the probe feels predominantly attractive forces, while smaller separations result in repulsive forces. At very large separations the net force is approximately zero.

Surface-Probe interaction

The interaction between an AFM probe and a surface can be modeled with the Lennard-Jones potential

$$V = \varepsilon[\left(\frac{r_0}{r}\right)^{12} - 2\left(\frac{r_0}{r}\right)^{6}], \tag{2.1}$$

where ε is the energy depth of the potential well, r is the probe-surface separation, and r_0 is the probe-surface separation where the potential is minimized. The r^{-12} term describes the short range Pauli repulsion while the r^{-6} describes the long range attractive van der Waals interaction. This potential is shown in Figure 2.2.

Attractive Mode

Attractive mode operates in the attractive regime, where the r^{-6} term in the Lennard-Jones potential dominates. In this mode the cantilever is driven above its resonance frequency, ω_0, with a low amplitude. The lower amplitude of this imaging mode

results in low wear on probe and very low forces on the sample. In order to image in attractive mode with the MFP-3D AFM in our lab, the cantilever is first tuned to a frequency above ω_0, where the amplitude is 10% less than the amplitude at ω_0. The target amplitude is set to 200 mV. When imaging, the amplitude set point is set to $\sim$ 60 % of the previously set target amplitude or $\sim$ 120 mV.

Repulsive Mode

When imaging in repulsive mode the cantilever is oscillated close to the sample where the r^{-12} term in the Lennard-Jones potential dominates. In this mode the cantilever is driven below its resonance frequency with a large amplitude. Repulsive mode can result in more wear on the probe and higher forces on the sample than attractive mode, but generally has somewhat higher resolution. In order to image in repulsive mode with the MFP-3D AFM in our lab, the procedure is generally the same as with attractive mode, but with different parameters. The cantilever is initially tuned to a frequency below ω_0 where the amplitude is 5% less than the amplitude at ω_0. The target amplitude is set to 1 V. When imaging, the amplitude set point is set to $\sim$60 % of the previously set target amplitude or $\sim$600 mV.

2.1.3 Contact Mode

In contact mode the AFM probe is not oscillated, but rather dragged along the sample surface. Feedback is maintained on the vertical deflection of the cantilever. The deflection is dependent on amount of flexure in the cantilever, so by maintaining a constant deflection, a constant force between the probe and sample is maintained. Contact mode is useful to rapidly determine topography of hard samples, though a soft sample may be damaged by this imaging mode. The direct contact with the surface allows one to determine frictional forces through lateral force microscopy (LFM). This imaging mode also allows for the nanomanipulation of some samples,

such as carbon nanotubes, where it is possible to push and flex the CNTs around a substrate.

In order to determine the applied load between the probe and the sample it is necessary to calibrate the relationship between the deflection of the cantilever and the force between the cantilever and the sample. This requires the determination of the cantilever's spring constant k, as well as the inverse optical lever sensitivity, $InvOLS$. The inverse optical lever sensitivity relates the z-displacement of the cantilever to the deflection signal measured by the PSD with the relationship

$$InvOLS = \frac{z - displacement \ [\mathrm{nm}]}{Deflection \ [\mathrm{V}]}. \tag{2.2}$$

The InvOLS is found by taking a force curve, where the cantilever is lowered until it is brought into contact with a hard sample surface, such as graphite, and then lifted back up, as shown in Figure 2.3. When the cantilever is in the 'free air' regime, where it is far from the surface, the long range forces acting on the cantilever are approximately zero, so the force curve is expected to be flat with no change in deflection. Generally, there will be some mechanical coupling between the deflection signal and the z-displacement. This is called virtual deflection, and can be corrected by fitting a line to the free air region and then subtracting this from subsequent force curves. When the probe becomes very close to the surface, attractive forces pull the cantilever downwards, causing it to 'snap' onto the surface, resulting in a abrupt decrease in deflection. As the cantilever is lowered further, it obeys Hooks law $F = k\Delta z$, and the deflection increases linearly as the cantilever is lowered. The InvOLS can then be found by taking the inverse of this slope, as in Equation (2.2).

The cantilever's spring constant can be obtained through various methods [23], such as the Sader method [24], where the spring constant of a rectangular cantilever in air is found to be

$$k = 0.1906\rho_f b^2 L Q_f \Gamma_i(\nu_k)(2\pi\nu_k)^2, \tag{2.3}$$

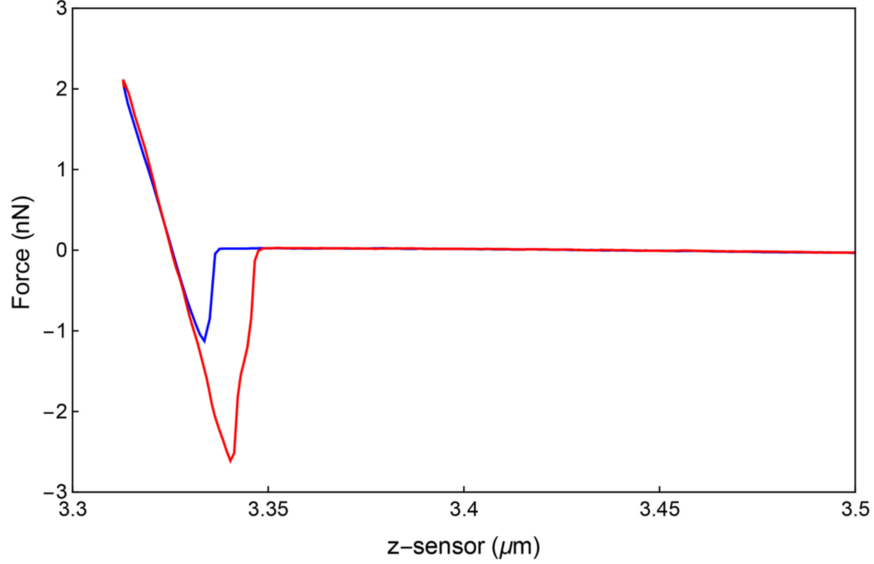

Figure 2.3: Example of an AFM Force curve. The red curve corresponds to the approach of the cantilever, while the blue curve corresponds to the retraction.

with quality factor Q_f, density of air ρ_f, resonance frequency ν_k, cantilever length L and width b, and imaginary part of the hydrodynamic function $\Gamma_i(\nu_k)$. Since the Sader method requires knowledge of the cantilever's dimensions, a thermal method that does not require this is often used instead. The thermal method works by applying the equipartition theorem to the fundamental resonant mode of the cantilever. The thermal energy is then related to spring constant k and the cantilever's mean-square deflection $\langle z^2 \rangle$ by

$$\frac{1}{2}k_B T = \frac{1}{2}k \langle z^2 \rangle , \tag{2.4}$$

with temperature T and Boltzmann constant k_B. In order to apply the thermal method, the InvOLS must first be determined as discussed above. The cantilever is then retracted 100 μm from the sample so it is not influenced by any long range interactions. The thermal tune is preformed by recording the amplitude of oscillations due to thermal fluctuations vs. frequency. A gaussian can then be fit to the fundamental resonant peak, resulting in values for the resonant frequency ν_k, quality factor Q_f,

and amplitude $z(\nu_k)$. The spring constant, k, can then be calculated using

$$k = \frac{2}{\pi} \frac{k_B T \, Q_f}{z^2(\nu_k)} \frac{\Delta\nu}{\nu_k}, \tag{2.5}$$

where $\Delta\nu$ is the frequency resolution and $z^2(\nu_k)$ is the square of the amplitude at the resonant frequency [23].

Lateral Force Microscopy

In addition to topography, contact mode imaging can allow for the measurement of local frictional forces. This is known as lateral force microscopy (LFM). In LFM the horizontal deflection of the cantilever is related to the lateral force experienced by the probe. The fast scan direction should be chosen to be perpendicular to the long axis of the cantilever. Both topographical and frictional variations result in a lateral deflection of the cantilever, as illustrated in Figure 2.4. Topographical and frictional features can be separated by comparing the trace (left to right) and retrace (right to left) LFM scans. Purely topographic features cause the cantilever to twist in the same direction regardless of scan direction, while frictional features cause the cantilever to twist in a scan direction dependent direction. Subtracting the LFM trace signal from the LFM retrace signal approximately doubles the frictional signal, while minimizing the effects of topography. The coefficient of friction can by obtained using

$$\mu = \alpha \frac{V_t - V_r}{2(L + A)}, \tag{2.6}$$

where α is the LFM calibration coefficient (see Appendix B), V_t and V_r are the LFM trace and retrace signals, L is the applied load, and A is the adhesion measured with a force curve as in Figure 2.3.

2.2 Scanning Electron Microscopy

Scanning electron microscopy (SEM) is utilized for both device fabrication as well as sample characterization. Since the de Broglie wavelength of moving electrons is

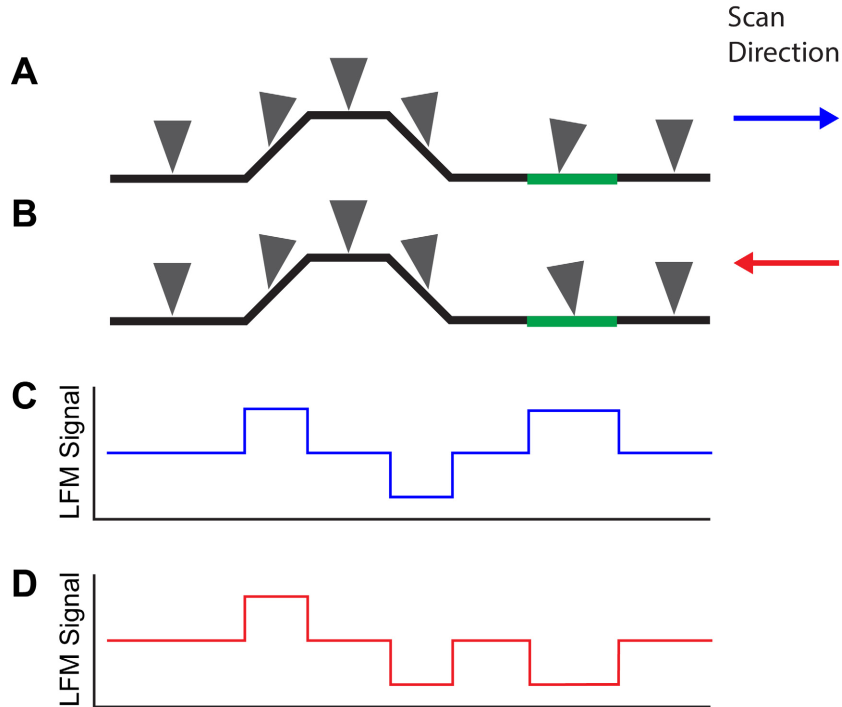

Figure 2.4: Lateral Force Microscopy Signal. Schematic illustration of the lateral deflection of a LFM probe as it moves over frictional (green region) and topographic features for the trace (A) and retrace (B) directions. (C) and (D) show the associated LFM signal for trace and retrace, respectively.

potentially much smaller than that of visible light, electrons are attractive for high resolution microscopy. While optical microscopes have resolution limits on the order of the wavelength of visible light, 0.5 µm, SEMs can achieve resolutions on the order of 1 nm with a magnification range of 100× to 300,000× [25]. This high resolution is utilized in sample fabrication through electron beam lithography (EBL). Scanning electron microscopes operate by focusing a beam of electrons through electromagnetic lenses onto a sample. This focused electron beam is raster scanned across the sample to create an image. The interaction between the incident electrons and the sample produces a number of electrons including backscattered electrons and secondary electrons, as well as x-rays. These can be detected to produce high resolution images, or analyzed in various forms of spectroscopy.

2.2.1 SEM Emitter Types

The electron beam is emitted from an electron gun, which typically uses either a thermionic emission, field emission, or Schottky type emitter. A comparison of these emitters can be found in Table 2.1. In order to liberate electrons from the surface of a material, they need to be given an energy greater than or equal to the material's work function. In a thermionic emitter, this energy is provided by thermal energy. This is usually achieved by Joule heating as a result of flowing a high current through the filament, generating a temperature of $\sim 2700\,\mathrm{K}$. By heating the emitter filament, some of the electrons are given enough energy to jump over the work function barrier. An anode, positioned below the filament, produces a voltage between itself and the filament, known as the extraction voltage and is usually in the range of a few kilovolts. This potential draws the electrons away from the filament, towards the sample chamber. A second anode, below the first, produces the accelerating voltage, usually in the range of 0.5-30 kV [25]. Thermionic emitters are relatively inexpensive, can be operated at higher pressures than other emitters, and have high beam current stability. However, they have a large virtual source diameter, resulting in a larger beam spot size and lower resolution. Compared to other emitter types, the high temperature results in a larger spread in the energy of the electrons, which can result in chromatic aberration.

In a field emitter, instead of thermally exciting electrons over the work function barrier, a strong electric field is used to cause the electrons to tunnel through the barrier. A strong field is created by applying a high voltage across a sharp emitter tip ($\sim 100\,\mathrm{nm}$). Field emitters require a ultra high vacuum (UHV) in the gun chamber, but benefit from low energy spread, a small virtual source diameter and a long life span. This results in relatively high resolutions and low chromatic aberration.

The Raith e-Line system used for this work utilizes a Schottky type emitter, which acts as a field-assisted thermionic emitter. In this type of emitter a sharp tungsten

Table 2.1: Comparison of Electron Emitter Types

Emitter Type	**Thermionic**	**Field Emission**	**Schottky**
Material	W	W	ZrO/W
Source Temperature (K)	2500-2900	300	1800
Work Function (eV)	4.5	4.5	2.8
Energy Spread (eV)	1 – 3	0.2 – 0.3	0.3 – 1.0
Virtual Source Diameter (nm)	$>10^4$	3 – 5	15 – 25
Operating Vacuum (Pa)	10^{-4}	10^{-9} – 10^{-11}	10^{-8} – 10^{-9}
Beam Current Stability (%)	<1	4 – 6	<1
Typical Life (h)	40 – 100	>2000	>2000

Adapted from reference [25]

⟨100⟩ tip is coated with zirconium oxide to lower its' work function. The tip is then welded onto a tungsten filament. Electron emission is then due to a combination of the applied extraction field as well as thermionic emission due to heating from the filament. Schottky type emitters have many of the benefits of the field emission emitters, with the additional benefit of very low beam current flickering (high beam current stability), making them ideal for electron beam lithography where current stability is important for a uniform electron dose.

2.2.2 Beam Sample Interaction

When the electron beam (primary electrons) reaches the sample, there are a variety of interactions which produce an array of signal types, including Auger electrons, secondary electrons ($E < 50\,\text{eV}$), backscattered electrons ($E > 50\,\text{eV}$), and X-rays, as shown in Figure 2.6A [26]. These various interactions take place over a characteristic volume. An approximate relation for the penetration depth, R_{pd}, of an electron

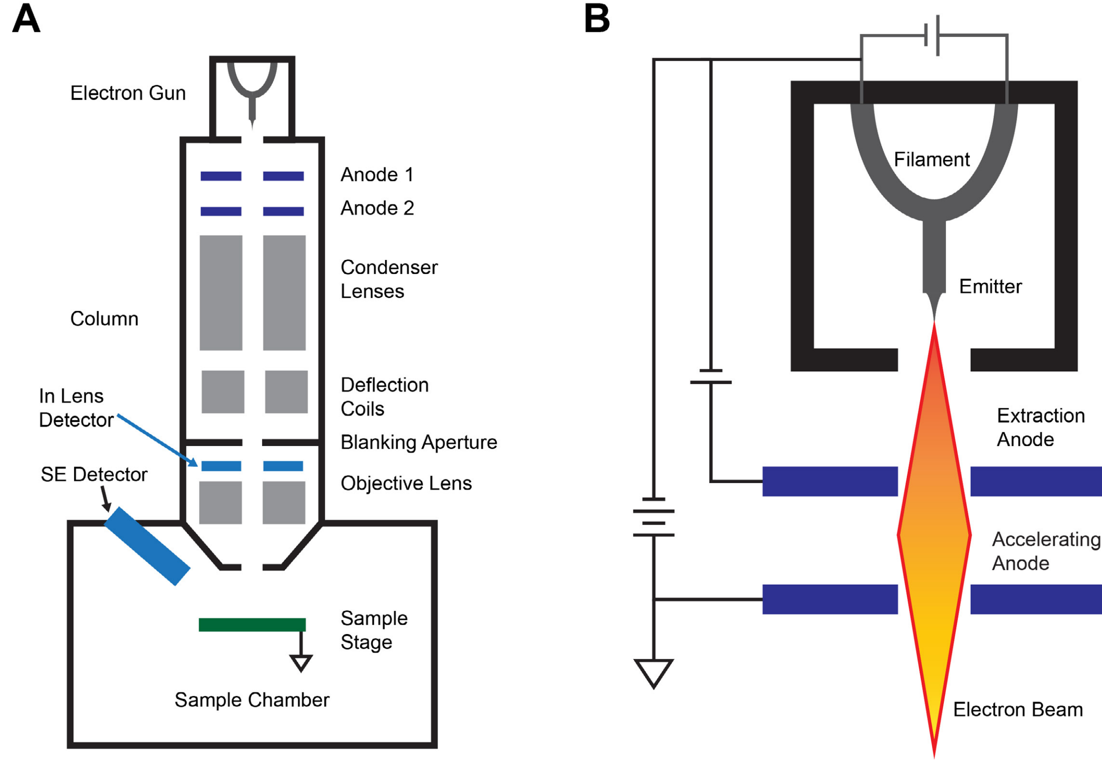

Figure 2.5: Schematic illustration of a scanning electron microscope. (A) Overview of the electron gun, column, and chamber. (B) Detail of the electron gun.

incident upon a thick, flat sample is the Kanaya-Okayama relation,

$$R_{pd}\ (\mu\text{m}) = 0.0276 \frac{A E_0^{5/3}}{\rho Z^{8/9}} \cos\theta, \tag{2.7}$$

where A is the atomic weight (g/mole), Z is the atomic number, ρ is the density (g/cm^3), θ is the angle of incidence measured from normal, and E_0 is the incident beam energy in keV [26, 27]. For the case of a normally incident beam on silicon, this produces a penetration depth of $\sim 1.4\,\mu\text{m}$ and $\sim 8.6\,\mu\text{m}$ when $E_0 = 30\,\text{keV}$ and $10\,\text{keV}$, respectively.

Backscattered Electrons

Backscattered electrons (BSE) are electrons with energy greater than 50 eV, which have been deflected back, out of the sample. These are the result of primary electrons undergoing elastic scattering events with the atomic nuclei in the sample. Elements

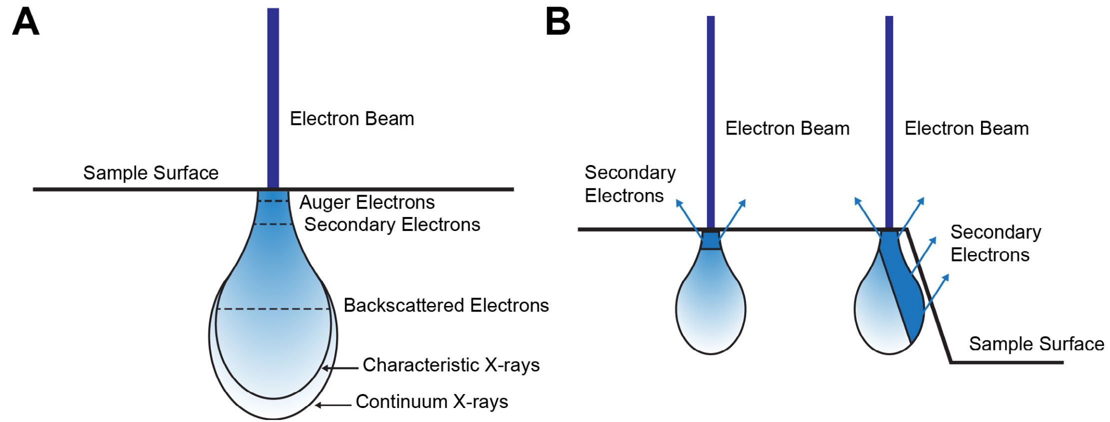

Figure 2.6: Schematic illustration of the electron-sample interaction in a SEM. (A) Illustration of the various signal types, showing the relative depths at which they can escape the sample. (B) The edge effect for secondary electrons. When the beam is close to an edge, a larger region of the interaction volume is close to the surface, resulting in more SE escaping and a brighter signal near the edge.

with high atomic number backscatter at a higher rate than those with low atomic number, so BSEs are useful for detecting differences in the elemental composition of samples. The depth that the BSEs come from varies based on sample details, but it is strongly dependent on the atomic number and the primary beam penetration depth R_{pd}. For an electron beam normally incident on gold, 90% of backscattered electrons come from a depth less than $\sim 0.17 R_{pd}$, while that figure is $\sim 0.29 R_{pd}$ for carbon [26]. This gives a general escape depth in the range of hundreds of nanometers to a few micrometers. The lateral distribution of backscattered electrons exiting the sample can extend a good fraction of R_{pd} away from the incident beam location, resulting in a lowering of resolution.

Secondary Electrons

The primary method of imaging with an SEM is through detection of secondary electrons (SE), which have energies of less than 50 eV. Secondary electrons are the result of inelastic scattering between energetic electrons and the electrons in the sample, resulting in the ejection of outer shell electrons in insulators, or conduction electrons in

metals. The majority of the secondary electrons have kinetic energies in the range of 2 – 5 eV, with 90 % less than 10 eV [26]. Both primary and backscattered electrons can produce SEs, resulting in a large number being produced, and a large signal. Secondary electrons produced by primary electrons are labeled SE_1, while those produced by backscattered electrons are labeled SE_2. The escape depth of secondary electrons is dependent on their mean free path, λ, with the escape probability p given by

$$p \approx \exp(-\frac{z}{\lambda}), \tag{2.8}$$

with z being the SE depth [26]. This results in a maximum escape depth of roughly 5λ, with most SEs coming from within a mean free path, which is $\sim 1 - 2$ nm for metals and ~ 10 nm for insulators [26,28]. The large signal and relatively short escape depth results in a higher resolution than other imaging modes, with SE_1 having higher resolution than SE_2. Secondary electron images show increased brightness on inclines and near edges, an phenomenon known as the edge effect. This is due to a larger surface area being within the escape depth of the interaction volume for a tilted edge than a normal one, as illustrated in Figure 2.6B. The relative number of escaping secondary electrons, $n_{SE}(\theta)$, roughly follows

$$n_{SE}(\theta) = n_0 \sec(\theta), \tag{2.9}$$

with surface angle θ, and n_0 equal to the number of escaping SEs for a normally incident beam [26].

Secondary electrons are usually detected using an Everhart–Thornley detector (E–T detector) [29]. An E–T detector detects electrons using a scintillator material, which produces light when struck by electrons. The scintillator is usually held at a positive voltage to accelerate the SEs onto it. This light is directed down a waveguide into a photomultiplier tube. In the photomultiplier tube, the photons are converted to electrons through the photoelectric effect and accelerated into a chain of dynodes

by electric field. Each time electrons strike a dynode, secondary electrons are emitted, creating a cascade effect that results in a gain of between 10^5 – 10^6. At the end of the chain the electrons strike an anode, resulting in an electric signal.

Auger Electrons and X-rays

Auger electrons are primarily produced very close to the sample surface (on the order of nanometers). When a high energy electron scatters with an electron in the inner shell of an atom, it can cause that electron to be ejected. This leaves a vacancy which will be filled by a second electron from a higher energy shell. The energy released by the second electron can be in the form of an emitted X-ray, or by the ejection of a third electron known as an Auger electron. Auger electrons are used in Auger electron spectroscopy (AES), which is useful for chemical characterization of the surfaces of a sample. Energy dispersive X-ray spectroscopy (EDX) is another spectroscopy technique that can be used for elemental analysis of materials. X-rays emitted in the above process have an energy equal to the energy released by the second electron in the above process, thus producing peaks at specific energies. These X-rays are called characteristic X-rays and have an escape depth of several micrometers. At increased depths, the X-rays lose energy due to interactions with the material, resulting in a continuous background signal that is not indicative of the atomic energy transitions.

2.2.3 Electron Beam Lithography

In this work, we use electron beam lithography (EBL) to pattern nanoscale electrical contacts on 2D materials. In EBL, a polymer, known as the resist, is spin coated onto a substrate and selectively exposed to a high energy electron beam in a SEM. For the case of a positive resist, the regions of the resist exposed to the electron beam become more soluble in a solvent (developer) and are removed during development, leaving

exposed regions. A metal is then deposited on top of resist and exposed regions of the chip. The remaining resist can be removed in a solvent, leaving metal only on regions that were originally exposed to the electron beam, as illustrated in Figure 2.7. Specific process steps can be found in Appendix A.

One of the most commonly used positive electron beam resists is poly(methyl methacrylate) (PMMA). PMMA consists of long polymer chains which undergo chain-scission reactions as a result of interactions with electrons during lithography [30]. These chain-scission reactions result in the long polymer chains breaking up into many shorter chains, which makes the PMMA more soluble. PMMA has a high resolution, on the order of 10 nm, but suffers from a relatively low sensitivity, meaning it needs a larger electron beam dose, on the order of 200 $\mu A\,s\,cm^{-2}$, to fully expose it. When exposed to very high electron doses, 5000–7000 $\mu A\,s\,cm^{-2}$, PMMA undergoes crosslinking reactions, resulting in the polymer chains binding together, which makes it difficult to remove with solvents [31]. In this case, PMMA can act as a negative resist, where the developer removes the unexposed regions.

When resist is exposed to an electron beam, the effects of forward scattering, backscattering, and secondary electron production play an important role in the resolution limits of EBL. Forward scattering of the incident beam results in an increase in effective beam diameter as the beam moves into the resist. This effect increases with increasing resist thickness and decreases with increasing beam energy [30]. The majority of the resist exposure is the result of secondary electrons. The large quantity of secondary electrons around the incident beam are responsible for an increase in spot size to around 10 – 20 nm.

Backscattered electrons can travel large distances from the incident beam, which results in the "proximity effect". This proximity effect is particularly detrimental in regions near large exposed regions. In the areas near the intentionally exposed regions, the exposure due to backscattered electrons is cumulative, resulting in an

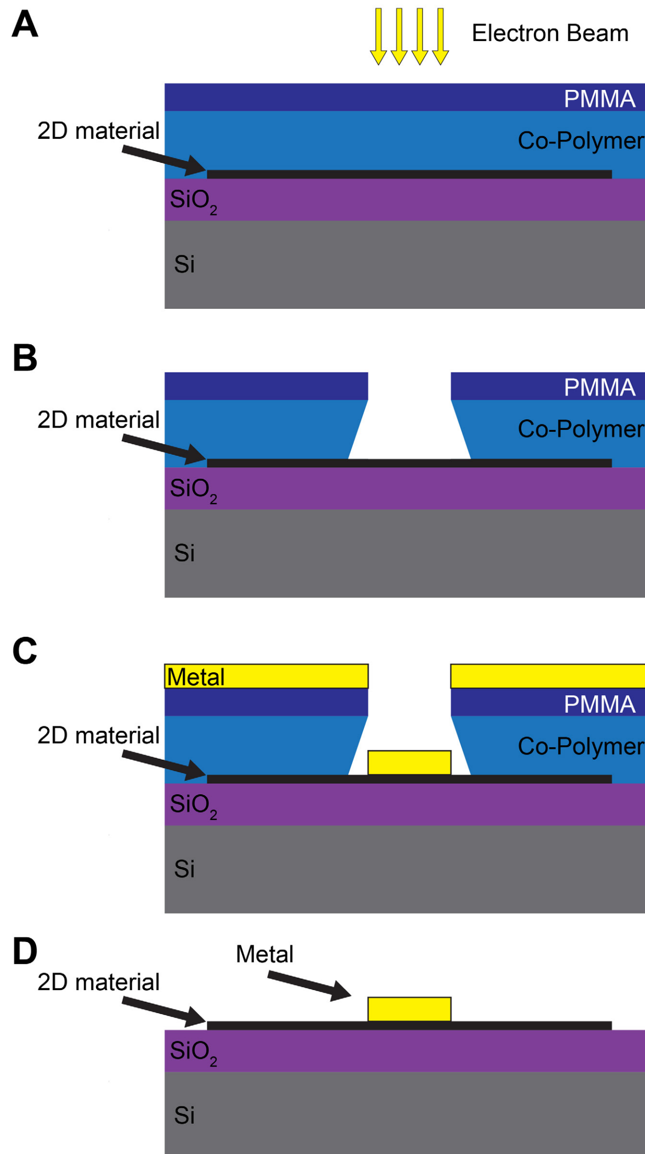

Figure 2.7: Schematic illustration of the electron beam lithography process. (A) PMMA/co-polymer stack is spin coated on top of a silicon wafer with 2D material sample. Regions where metallic leads are desired are exposed to an electron beam. (B) The wafer is placed in a developer, which removes the PMMA/co-polymer that had previously been exposed to the electron beam. (C) Metal is deposited on the chip by electron beam evaporation. (D) In the liftoff step, the wafer is immersed in a solvent to remove the PMMA/co-polymer stack along with the metal resting on the PMMA.

expansion of the exposed region and a contraction of the unexposed region. This can inadvertently connect regions and reduce resolution.

For this work, a double layer resist structure was used to aid in the liftoff step. A lower molecular weight co-polymer is spin coated on the bottom, with a higher molecular polymer on top. The lower molecular weight is more sensitive than the higher molecular weight PMMA. This setup results in under cut of the co-polymer beneath the PMMA, as illustrated in Figrue 2.7. The undercut makes it so the deposited metal does not directly contact the sides of the resist, while leaving the PMMA as a high resolution mask above. This helps to ensure a clean liftoff.

2.3 Electrical Measurements

Electrical measurements are generally performed under vacuum in a Lakeshore cryogenic probe station. This system allows for stable cryogenic temperatures and precise positioning of electrical contact probes. Contact probes are connected to ammeters and voltmeters with coaxial cables with BNC connectors. Current is measured by a Keithley 6517A electrometer/high resistance meter, which is also responsible for providing gate voltages. Bias voltages are measured with a Keithley 2182A nanovoltmeter as well as a National Instruments BNC 2120 DAQ. Both the electrometer and the nanovoltmeter are controlled with in-house LabVIEW routines.

2.4 Raman Spectroscopy

Raman spectroscopy probes the vibrational modes of a crystal through inelastic photon-phonon scattering. When light is incident on a material, some of the incident photons undergo scattering. The predominant scattering mechanism is elastic scattering, known as Rayleigh scattering, where the incident photon energy is equal to the reflected photon energy. A small percentage of the photons scatter with phonons

in the system resulting in a reflected photon with either lower energy (Stokes Raman scattering) or higher energy (anti-Stokes Raman scattering) than the incident photon.

Stokes and Anti-Stokes Raman scattering can be understood through the strain dependence of the electric polarizability [17]. The polarizability α associated with the phonon is related to the induced dipole moment $\mathbf{P}$ and the incident electric field of the photon, $\mathbf{E}$, through the equation:

$$\mathbf{P} = \alpha \cdot \mathbf{E}. \tag{2.10}$$

We take the time dependent electric field to be given by $E(t) = E_0 \cos(\omega t)$, with amplitude E_0, angular frequency ω, and time t. The dipole moment is then

$$P(t) = \alpha \cdot E_0 \cos(\omega t). \tag{2.11}$$

The atomic polarizability can be expanded in terms of the phonon amplitude u for small u, giving:

$$\alpha = \alpha_0 + \frac{\partial \alpha}{\partial u}\bigg|_{u=0} u + \ldots \tag{2.12}$$

If we take the time dependent phonon amplitude to be a harmonic oscillator with displacement $u(t) = u_0 \cos(\Omega t)$, where Ω is the phonon frequency, then the polarizability becomes:

$$\alpha(t) = \alpha_0 + \frac{\partial \alpha}{\partial u}\bigg|_{u=0} u_0 \cos(\Omega t) + \ldots \tag{2.13}$$

To first order, the induced dipole moment is then

$$\begin{aligned} P(t) &= \alpha_0 E_0 \cos(\omega t) + \frac{\partial \alpha}{\partial u}\bigg|_{u=0} u_0 \cos(\Omega t) E_0 \cos(\omega t) \\ &= \alpha_0 E_0 \cos(\omega t) + \frac{1}{2}\frac{\partial \alpha}{\partial u}\bigg|_{u=0} u_0 E_0 [\cos((\omega - \Omega)t) + \cos((\omega + \Omega)t)], \end{aligned} \tag{2.14}$$

where we have used the relation $\cos(a)\cos(b) = \frac{1}{2}[\cos(a-b) + \cos(a+b)]$ in the second line. An oscillating dipole moment results in the emission of EM radiation. The first term corresponds to the Rayleigh scattering at frequency, ω, equal to the incident photon. The second part has two terms and is responsible for Raman scattering. The

term corresponding to photons emitted at frequency $\omega - \Omega$ is the Stokes scattering and the term corresponding to photons emitted at $\omega + \Omega$ is the anti-Stokes scattering.

Experimentally, Raman spectroscopy is accomplished by focusing incident laser on a sample through an optical microscope. In our lab we utilize a HeNe laser with wavelength $\lambda = 633$ nm. Laser power on the sample is kept < 4 mW through the use of a variable neutral density filter to avoid damage to the sample [32]. The reflected light travels back through the microscope, where it encounters a notch filter that filters out the Rayleigh scattered light, which would otherwise overwhelm the Raman signal. The light is then sent through a spectroscope where the spectra can be recorded on a CCD sensor.

Graphene and Graphite have three prominent Raman peaks, labeled D, G, and $2D$. The G peak occurs at ~ 1575 cm^{-1} and is due to the zone center E_{2g} mode [33]. The D peak, which occur at ~ 1350 cm^{-1} is due to zone-boundary phonons. These phonons violate the Raman fundamental selection rule, so they are not seen in a perfect crystal. Crystal defects, or termination of the crystal structure in the form of edges, are required to loosen the selection rule. Because of this, the D peak is useful for determining the purity of graphene samples as well as edge purity and crystal orientation [34]. The $2D$ peak occurs at ~ 2700 cm^{-1} and is the result of a double resonance process involving two phonons around the K-point [32]. The double resonance process involves a electron-hole excitation, two electron-phonon scattering events and an electron-hole recombination. This process results in a dependence on the electronic structure of the graphene for the $2D$ peak. Monolayer graphene's single π and π^* bands result in a peak with a single component, while the splitting of bilayer graphene's bands results in a four component peak. Figure 2.8 shows the evolution of the line shape of the $2D$ peak from single layer graphene to bulk graphite. This transition makes the $2D$ peak very useful for accurately determining the layer thickness of graphene sheets, particularly given the thickness variation AFM

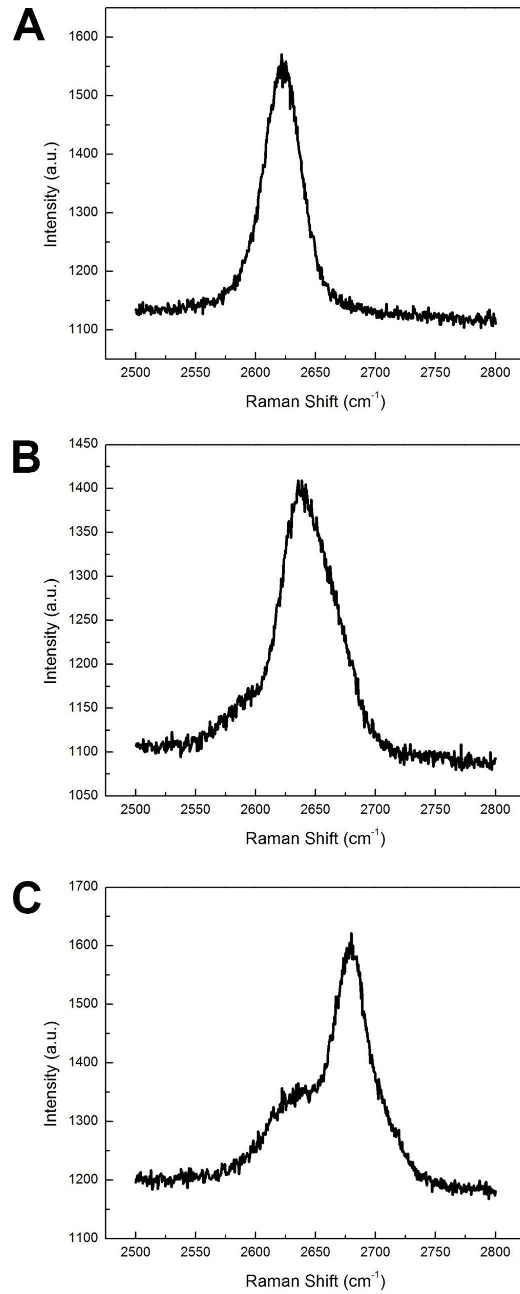

Figure 2.8: Comparison of Raman $2D$ spectra for varying graphene thicknesses. (A) shows the graphene $2D$ peak. (B) $2D$ peak for bilayer graphene. (C) $2D$ peak for bulk graphite.

measurements give due to the chemical contrast between graphene and the SiO_2 substrates [32].

Copyright© Mathias J. Boland, 2016.

Chapter 3 Striped Nanoscale Friction and Edge Rigidity of MoS_2 Layers[1]

3.1 Introduction

There is tremendous interest in reducing the overall size of machines and their components to attain the smallest moving devices possible [35]. However, at these extremely reduced dimensions the mechanical properties of the nanoscale surfaces bring new challenges in their control and understanding [36, 37]. As machines are reduced in size towards this nanoscale regime, atomically-thin laminar materials are becoming increasingly attractive as ultra-thin coatings that could modify and protect the mechanical component surface properties (such as the local friction and elasticity), while maintaining the overall nanoscale topographical features [38–42]. Two of the most important laminar materials in modifying surface mechanical properties are graphite and MoS_2, as these have long been used as dry solid lubricants in large-scale applications due to the ability of their van der Waals (vdW) coupled layers to slide against each other [14]. There has long been interest in the behavior of few-layer and atomically-thin films of such laminar materials [43, 44] which has received recent extensive renewed interest [3]. Moreover, using these materials as atomically-thin mechanical coatings has been made much more achievable due to recent advances in the synthesis [45] and controlled placement [46] of few-layer fillms of these laminar materials. To fully exploit this growing class of potential atomically-thin nanomechanical coatings, it is critically important that the nanoscale mechanical properties of these materials be understood [39].

Towards this effort, there have been a number of advances in understanding the nanoscale mechanical properties of these atomically-thin laminar materials. This in-

[1] Reproduced from Mathias J. Boland, *et al.*, *Striped Nanoscale Friction and Edge Rigidity of MoS_2 Layers*, RSC Adv., 2015, 5, 92165, DOI: 10.1039/c5ra20617k with permission from the Royal Society of Chemistry

cludes single asperity investigations of laminar materials frictional properties, [47,48] extreme strength and elastic properties, [49] delamination, [50,51] anisotropic friction and puckering of their surfaces, [48, 52] and localized frictional spikes at their step edges [53,54]. It has also been demonstrated that multi-layer [55] and single layer [53] films of these laminar materials can effectively eliminate underlying nanoscale frictional spikes associated with step edges when they are used as coatings. Recent work has shown that covered edges of these materials have very different physical and chemical properties in comparison to exposed ones [56,57] which show increased friction in the presence of absorbed water [58]. Moreover, the sharpness of the asperity in contact with an edge has been shown to play an important role in the local mechanical properties in the vicinity of a laminar materials edge [53, 57, 59, 60]. Through the use of an extremely sharp asperity it was shown that an exposed edge of graphene could be flexed and result in its stick-slip, [53] as also suggested by molecular dynamic simulations [61]. Possibly related to this behavior at step edges have been recent reports of a striped stick-slip phase on graphite surfaces that is thought to result from the localized puckering of its surface [62,63]. While anisotropic sliding has been observed on MoS_2 [64] (as it has on graphite surfaces [65]), localized nanoscale stick-slip and periodic frictional modulations have not yet been observed in this laminar material.

Here we report the elasticity of MoS_2 edges and a striped frictional phase at the nanometer scale in this laminar material. We find that sharp lateral force microscopy (LFM) tips can effectively flex the edges of MoS_2, with results consistent with out-of-plane bending. These results show that MoS_2 edges are slightly stiffer compared to those of graphene, a result which may be partly due to the stronger vdW interactions of MoS_2 layers. We also observe a periodic striped frictional phase on MoS_2 surfaces having a wavelength of $\sim 4\,\text{nm}$. The striped frictional phase is shown to be robust over regions greater than $\sim 100\,\text{nm}$ and remain fixed to the underlying MoS_2 upon variation of the fast scan direction. Our experimental results suggest that this

nanoscale periodic frictional phase of MoS_2 could be due to a striped strain field that varies the local puckering of the atomically-thin material in the presence of an asperity, and as a result modifies the local friction. Such robust modulations of an atomically-thin material could have application in controlling the surface mechanical properties at the nanoscale with long-range order.

3.2 Experimental Details

3.2.1 Sample Preparation

Silicon substrates with a 300 nm oxide layer were placed in an ultrasonic cleaner with acetone, isopropyl alcohol, and deionized water for 3 minutes each, followed by UV-ozone cleaning in a NovaScan PSD Series Digital UV Ozone System for 15 minutes. MoS_2 (obtained through SPI Supplies) was then mechanically exfoliated onto the silicon substrates. After exfoliation, the samples underwent CVD processing consisting of a constant gas flow rate of 380 sccm Ar and 340 sccm H_2 at 400 °C for one hour to remove tape residue.

3.2.2 Lateral Force Microscopy Measurements

The LFM measurements were performed using an Asylum Research MFP-3D atomic force microscope (AFM) with PPP-LFMR and PPP-CONTSCR probes manufactured by Nanosensors. Both types of probes have nominal force constants of 0.2 N/m, resonant frequencies of 23 kHz, and a tip radius of curvature less than 10 nm. During LFM operation the probe is placed in contact with the sample surface and the fast scan direction is chosen to be perpendicular to the cantilever beam while both lateral and vertical deflections are measured. Prior to each LFM measurement the adhesion force between the probe tip and the sample is measured. During each scan the net force, F_{net} is kept constant. Here, F_{net} is defined as the sum of the normal

load applied to the tip, L, and the adhesion force between the tip and the surface, All measurements were taken in ambient laboratory conditions (temperature $\sim$ 20 °C).

To investigate the frictional response of MoS_2 edges we start with sharp LFM probes, as determined through measurement of the probes adhesion force, [53] and focus on single layer MoS_2 step edges. LFM probes are observed to catch atomic step edges when the adhesion force is $\leq$2 nN. In order to maintain the sharp probes, we limit LFM scan sizes to <1 µm, and avoid scanning over the SiO_2 substrate, which is observed to increase the adhesion force. LFM scans are performed with the fast scan direction perpendicular to the cantilever. Both the lateral and vertical deflections of the probe are monitored with a laser that reflects off the cantilever and onto a four-quadrant position sensitive detector (PSD). The vertical deflection is controlled through a feedback loop in order to maintain a constant load force as well as provide topographical information. As an LFM probe is scanned along a surface, lateral forces acting on the probe cause torsional rotation of the cantilever, resulting in a lateral deflection of the laser spot at the PSD.

Calibration of the lateral voltage signal (V_{lat}) is performed using a low load method introduced in Ref. [53] that assumes a vertical adhesion for atomically-thin laminar materials, rather than the usual normal adhesion [66, 67]. Since this calibration technique is performed at low loads, $\sim$ 4 nN, and over atomically smooth materials, the probes remain sharp and exhibit minimal changes in adhesion over the course of the calibration.

3.3 Results and Discussion

3.3.1 Elastic Response of MoS_2 Edges

Figure 3.1 shows the results of lateral force microscopy (LFM) measurements of a MoS_2 step edge consisting of 10 layers on the left of a step (measured to be $\sim$ 6.5 nm thick relative to the SiO_2 substrate using an AFM) and 9 layers on the right

(measured to be ~ 5.9 nm thick), as schematically illustrated in Fig. 3.1(a). Figure 3.1(b) shows a corresponding round-trip line scan of the measurement across the step-edge with $F_{net} = 8.26$ nN, where the blue line is the trace scan from left to right, while the red retrace scan is from right to left. For this low-adhesion tip (with $A = 1.8$ nN) we observe LFM measurements that demonstrate stick-slip behavior for loads greater than ~ 4 nN. The line scan in Fig. 3.1(b) shows an ~ 11 nm wide region of increased signal at the MoS_2 edge in the retrace (stepping-up) direction accompanied with a large lateral signal, while a significantly smaller signal is observed in the trace (stepping-down) direction. Moreover, the larger retrace signal has a roughly linear signal as a function of distance, as expected for a spring obeying Hookes law. Such behavior is consistently observed at the MoS_2 edge, as seen in the LFM trace and retrace scan images in Figs. 3.1(c) and 3.1(d), respectively. The graded dark region in Fig. 3.1(d) is the spring loading (stick) of the MoS_2 edge while the abrupt contrast change on its left is the MoS_2 edge abruptly slipping under the LFM tip.

Using the calibration of the LFM tip, as discussed above in Experimental details, we are able to deduce the effective spring constant through the slope of the LFM retrace signals, as in Fig. 3.1(b), which gives $k = 0.350 \pm 0.063$ nN/nm for the MoS_2 edge. This spring constant and the displacement yield a stored elastic energy of $\frac{1}{2}kx^2 \approx 132$ eV, which is similar to the values seen for graphene (~ 90 eV) [53]. Given reported values of the Youngs modulus $E \approx 0.27$ TPa, Poisson ratio $\nu \approx 0.27$, and thickness $t = 0.65$ nm of MoS_2, we estimate the in-plane strain energy for an $x = 10$ nm displacement as $\frac{\pi t}{8}\frac{E}{1-\nu^2}x^2 \approx 46{,}000$ eV [53,68]. This energy is much larger than that measured with the cantilever, indicating the MoS_2 edge is likely bending out-of-plane (as depicted in Fig. 3.1(a)), rather than in-plane [53]. The fact that the effective spring constant for flexing the MoS_2 edge is slightly larger than that measured for graphene (0.29 ± 0.11 N/m) [42] may be partially due to the larger vdW adhesion of MoS_2 (2.1 eV/nm^2) as compared to graphene (0.9 eV/nm^2) [69].

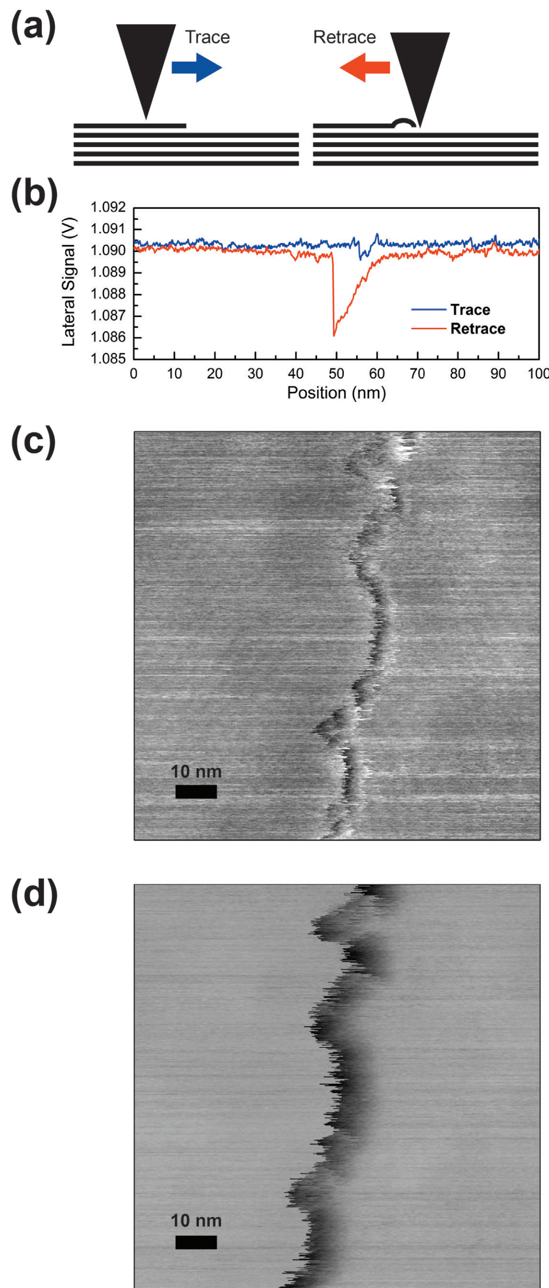

Figure 3.1: LFM of a single layer MoS_2 step edge. (a) Schematic of round-trip LFM line scan taken over a single-layer step-edge of MoS_2. As illustrated by the schematic, the MoS_2 film has one extra layer on the left. (b) Round-trip LFM line scans where the blue step-down trace scan is from left to right and the red step up retrace scan is from right to left, consistent with the schematic in (a). LFM trace images over the same step edge are shown in (c) for the trace direction and (d) for the retrace direction. Measurements in (b)-(d) were made with a net load of $F_{net} = 8.3$ nN for a LFM tip with a 1.6 nN adhesion.

Insight into the stick-slip response of the MoS_2 step edge can be obtained by using the model for bending laminar materials proposed in Ref. [53] which is based on the approximate low-load analytic form of the Schwoebel-Ehrlich energy barrier in the vicinity of an atomic step-edge [60,70,71]. This energy barrier is approximated by $U = \varepsilon\{-\text{erf}(x/b_1)+\text{erf}([x-c]/b_2)\}$, [60] where ε is a constant of order an eV, b_1 represents the effective width of the MoS_2 edge ($x \equiv 0$), which should be on the order of the tip apex radius, and b_2 and c are constants which represent a slow recovery of the potential away from the edge which should be larger than b_1. For a tip moving into a step edge, the slip point occurs at the point where $\frac{d^2U}{dx^2} = -k$. Previously, it was found that assuming an atomically-sharp asperity of $b_1 \approx 0.1$ nm (with $b_2 = c = 10b_1$) and a reasonable energy barrier of $\varepsilon = 2$ eV for an atomically-thin segment of a graphene edge yields a stick-slip distance of ~ 11 nm, in good agreement with the experimentally observed value [53]. For the case of a MoS_2 edge using the same normal load, the calculation of the stick-slip distance must be modified by using the slightly larger measured spring constant. In addition, one could expect a larger energy barrier at the MoS_2 edge in comparison to a graphene edge, since the physical step height is greater. To account for this larger barrier we take ε of the MoS_2 edge to be the value used previously for graphene scaled by the ratio of the thicknesses, i.e., $\varepsilon = \frac{0.65\text{ nm}}{0.335\text{ nm}} \times 2.0\,\text{eV} \approx 3.9\,\text{eV}$. This modified barrier height, combined with the measured spring constant yield an expected stick-slip distance of ~ 19 nm, in order of magnitude agreement with the ~ 11 nm observed experimentally in Fig. 3.1. The deviation between the calculated and measured stick-slip distances is likely due to the rough estimate of the barrier energy, ε, and width, b_1.

3.3.2 Nanoscale Frictional Stripes

In the vicinity of the MoS_2 edges we also observe modulated nanoscale frictional stripes. Such stripes are slightly apparent in the LFM trace image of Fig. 3.1(c), but

become easier to discern as F_{net} is decreased. Figure 3.2 shows LFM images obtained with a nN where the frictional stripes are clearly discernable for both the trace (Fig. 3.2(a)) and retrace (Fig. 3.2(b)) scans. These features consist of modulations of the lateral signal with a wavelength of $\sim$ 4.1 nm, an order of magnitude larger than the MoS_2 lattice constant (0.315 nm). Figures 3.2(c) and (d) show the lateral signal at the locations marked by the blue and red lines in Figs. 3.2(a) and (b). Although crossing the step edge results in an abrupt change in angle of the frictional stripes by approximately 57°, it does not result in a noticeable change in the modulation length scale (*i.e.*, the wavelength). Moreover, these frictional features appear continuous over the scan region and show long-range order greater than $\sim$ 100 nm. It is likely that the relative orientation of the stripes is related to the hexagonal symmetry of the MoS_2. While the observed angles are not exactly at 60 degree intervals, this slight orientational deviation from that expected for the six-fold symmetric MoS_2 lattice is consistent with the reported angular deviations of stripes observed on graphene, which are thought to arise from slight grain boundary misalignments [62].

This striped frictional phase appears robust to various methods of probing its LFM response. For example, the scan rate of the LFM measurement over the MoS_2 surface appears to make no noticeable effect, as seen in Fig. 3.3. Despite a factor of three variation in scan rate (from 0.15 Hz to 0.45 Hz) in going from Fig. 3.3(a) to 3.3(c), there is no appreciably change in the wavelength of these features, as verified through the use of a 2D Fast Fourier Transform (2D FFT) in Fig. 3.3(d). This FFT shows peaks at wave number magnitudes that are all approximately 0.25 nm^{-1}, thus having the same wavelength regardless of scan rate, as shown in Fig. 3.3(e). The identification of the peaks in the FFT with the stripes in the LFM images is confirmed by selectively eliminating these Fourier components (circled in the FFT inset in Fig. 3.3(f)) and then taking the inverse transform, which (as a result) no longer contains the associated stripes on the right-hand side of the step. The fact that

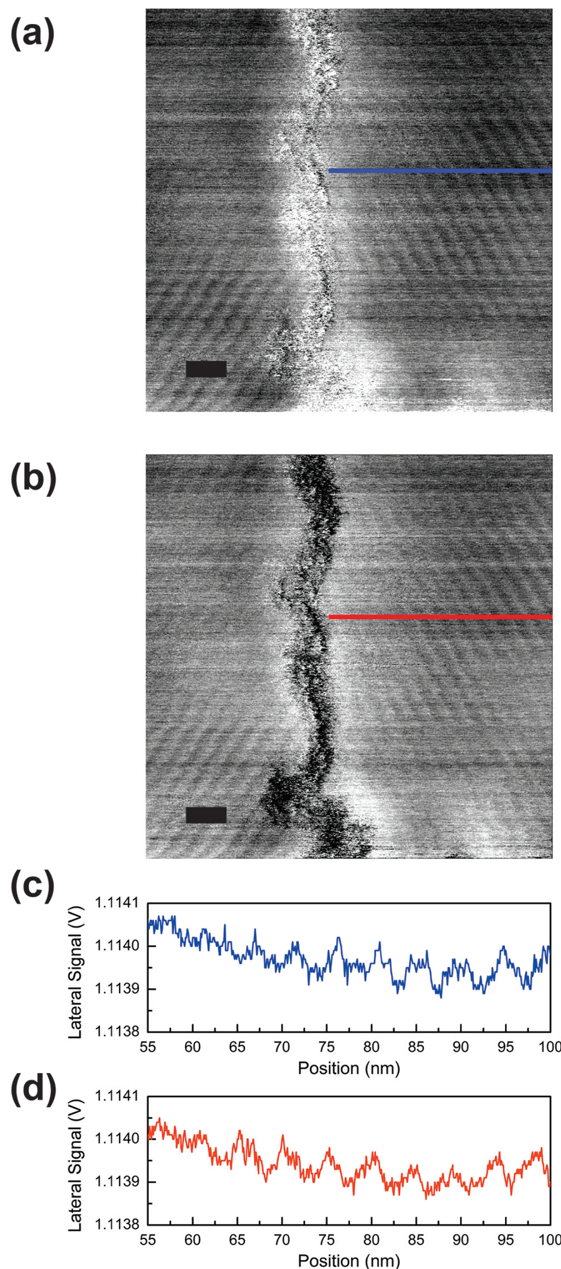

Figure 3.2: Periodic frictional stripes. (a) LFM trace image of MoS_2 showing parallel frictional stripes. The MoS_2 on the right (left) side is $\sim$ 6.5 nm (5.9 nm) thick ($\sim$ 10 (9) layers) as determined through AFM topography measurements. Upon crossing a step edge (the brighter vertical line) the angle of the stripes abruptly changes. (b) Same as (a), for the retrace direction. (c) and (d) are the average of 10 LFM scans at the locations specified by the blue and red lines in (a) and (b), respectively. These line scans show a 4.6 nm wavelength, which after correcting for the 27 $^\circ$ angle between the line scan and the direction perpendicular to the oscillations gives a wavelength of 4.1 nm. Adhesion and of the probe were 4.45 nN and 1 nN, respectively. Scale bars are 10 nm.

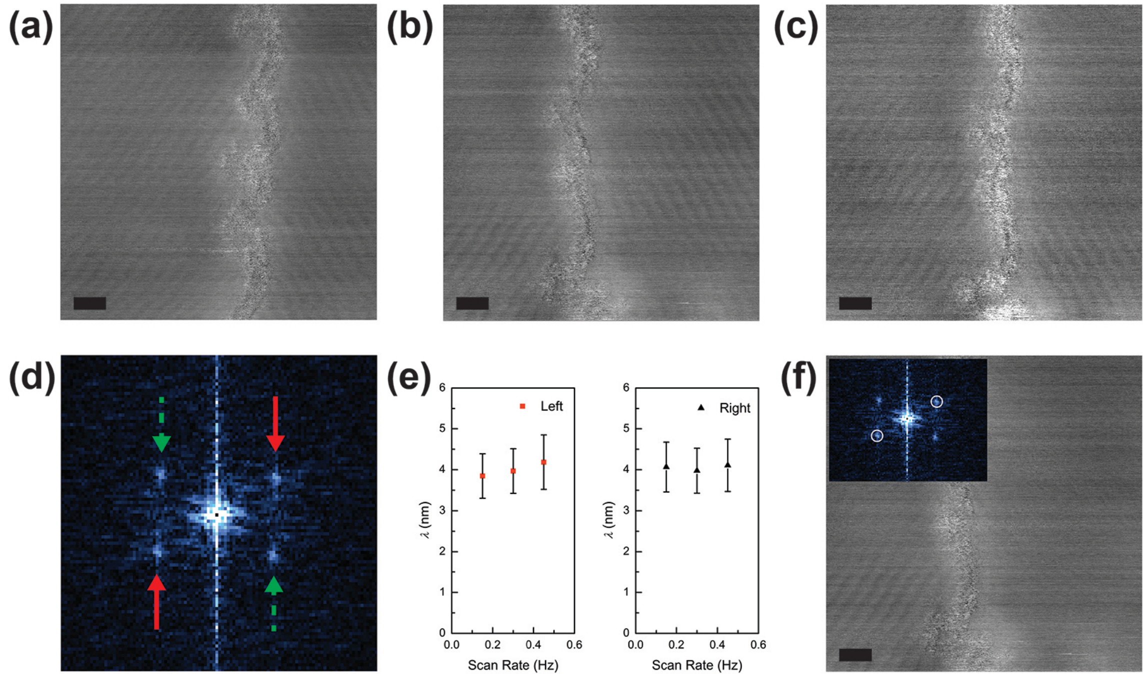

Figure 3.3: (a)-(c) LFM trace images of the same MoS_2 region as in Fig. 3.2 taken at a range of scan speeds, with similar adhesions and net loads. (a) LFM trace with a scan speed of 0.15 Hz, adhesion of 4.35 nN, and F_{net} of 1.01 nN. (b) Image taken with a scan speed of 0.30 Hz, adhesion of 4.45 nN, and of 1.0 nN. (c) Image taken with a scan speed of 0.45 Hz, adhesion of 4.13 nN, and of 1.37 nN. (d) FFT of (b) with the peaks marked with the solid red (dashed green) arrows corresponding to the stripes on the right (left) side of the step edge (central bright vertical region) in (b). These peaks occur at wave number magnitudes of 0.252 nm^{-1} and 0.253 nm^{-1}, corresponding to wavelength of 3.97 nm and 3.95 nm for the features on the right and left side, respectively. (e) Wavelength as a function of scan rate for features to the left (red squares) and right (black triangles) of the step edge, showing no dependence between scan rate and wavelength. (f) Selective removal of the circled peaks in the FFT (inset) with the resulting subsequent inverse transform showing that the associated stripes are removed from the image. All scales bars are 10 nm.

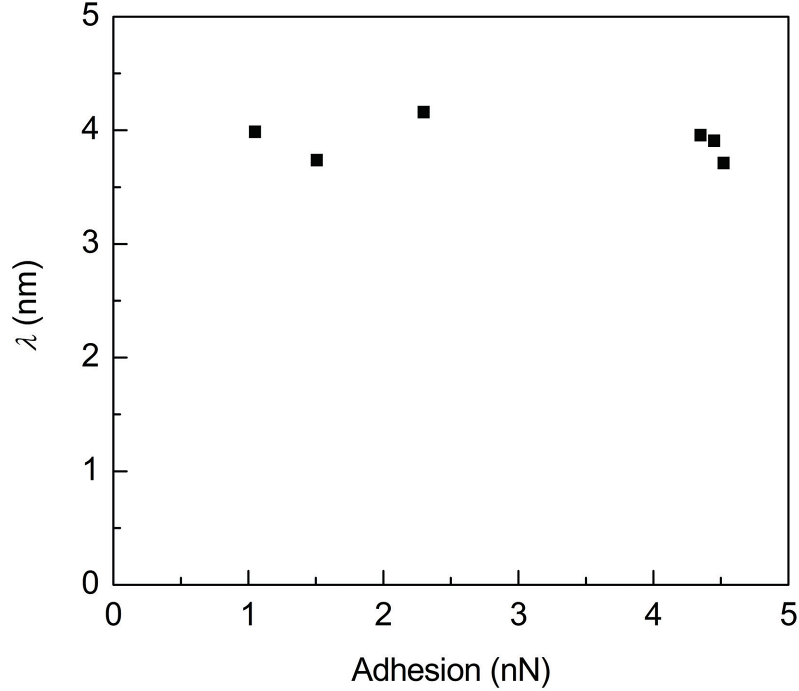

Figure 3.4: Plot showing that the wavelength of oscillations, λ, is relatively independent of the adhesion of the LFM probes used. The wavelength is measured with tips having different adhesions.

the wavelength is independent of scan rate indicates that these nanoscale frictional stripes are not due to extrinsic artifacts, such as periodic noise in the imaging system. More evidence that the stripes do not depend strongly on the details of the probe comes from the fact that LFM tips with different adhesions measure the same (~ 4.1 nm) periodicity, as seen in Fig. 3.4.

The amplitude of these frictional stripes also appears relatively insensitive to the scan parameters. In Fig. 3.5(a) we plot the RMS modulation of the lateral signal associated with the stripes (δV_{lat}) and the calibrated lateral force (δF_{lat}) as a function of scan rate in the vicinity of the step edge. (δV_{lat} is determined by taking the square root of the integral of the modulus squared of the associated FFT peaks.) This plot shows that the amplitude of the stripes is relatively insensitive to the speed of the LFM tip. Likewise, Fig. 3.5(b) also shows that the overall net load of the tip, F_{net} (from 1.42 nN to 8.26 nN), does not have an appreciable effect on the amplitude of the

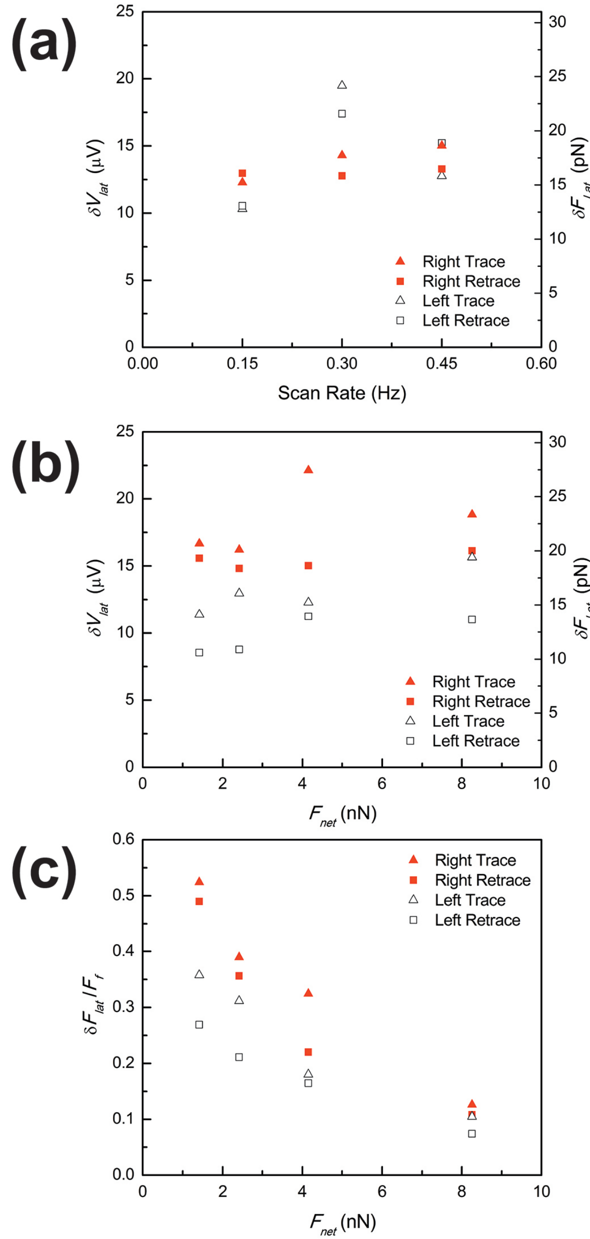

Figure 3.5: Comparison of lateral force arising from the stripe features for various loads and scan rates with the same LFM probe. (a) Plot showing the RMS lateral voltage signal and corresponding lateral force of the stripe features as a function of scan rate, as determined through the FFT of the LFM signal. (b) Plot of the RMS lateral voltage and force arising from the stripes on the right (red) and left (black) side of the step edge as a function of F_{net}. For all four F_{net} values plotted, the same LFM probe was used, and the adhesion remained between 1.31 nN and 1.71 nN. (c) Plot of the ratio of the RMS lateral force due to the periodic stripes to the average frictional force, F_f, as a function of F_{net}.

stripes. In contrast, the background average frictional force between the surface and the probe increases roughly linearly, with the form $F_f \approx \mu F_{net}$, where μ is found to be ~ 0.022. Thus, as shown in Fig. 3.5(c), the relative size of the modulated lateral force due to the stripes to the background frictional signal, $\delta F_{lat}/F_f$, decreases in magnitude as F_{net} is increased. This variation in the ratio is likely the reason that the striped frictional phase is much more readily apparent at low F_{net}.

Also attesting to the intrinsic nature of the lateral force modulations is the fact that the stripes appear fixed to the MoS_2 lattice, as is shown by rotating the sample below the tip. Figure 3.6(a) shows a LFM retrace image with the fast scan direction perpendicular to the step edge. The frictional variation on either side of the step edge are approximately $\pm 30°$ from the vertical. Upon rotation of the sample by $\sim 30°$ clockwise (Fig. 3.6(b)) the features to the right of the step edge are perpendicular to the fast scan direction. Thus, they appear to rotate with the sample and their relative orientation is determined by the MoS_2 surface, rather than the scan angle of the tip (which remains the same between Figs. 3.6(a) and 3.6(b)). It is also apparent from the rotated scan in Fig. 3.6(b) that the amplitude of the stripes is dependent on their orientation with respect to the scan direction. This nanoscale frictional dependence on the scan angle could be related to the long-range (average) frictional dependence of single asperity tips on a strained and puckered surface of graphene, which has also been shown to be anisotropic [52].

Over the range of several hundred nanometers these modulated frictional features we observe appear to be ordered with some domains greater than 200 nm. To probe the long-range variation of these domains, we make LFM measurements at locations separated by several microns on the ~ 5.2 nm thick flake of MoS_2 shown in the AFM image in Fig. 3.7(a). Figs. 3.7(b) and 3.7(c) show lateral trace images of the flake at the locations marked in Fig. 3.7(a) by the solid red and blue dashed arrows, respectively. These two locations are separated by $\sim 2.5\,\mu$m on a single terrace and

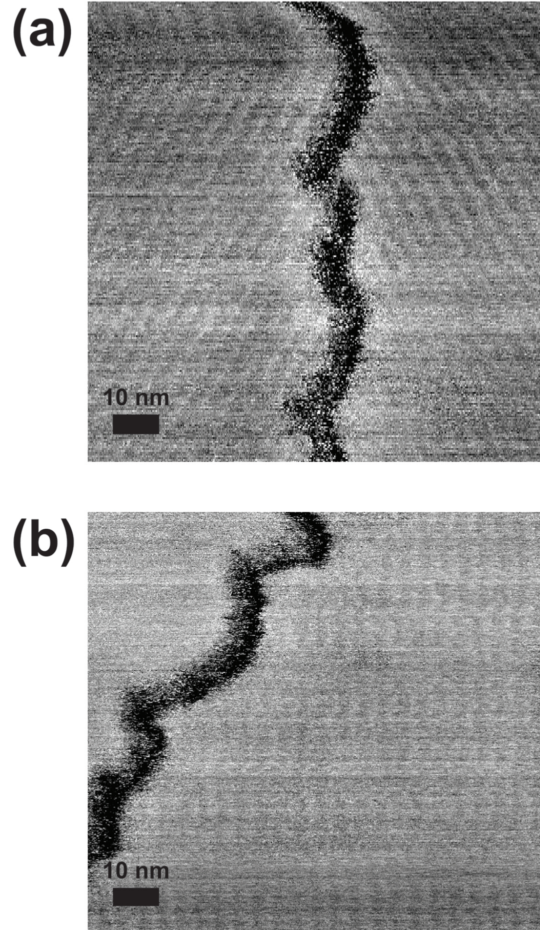

Figure 3.6: LFM images showing the effects of varying the scan angle on the MoS_2 frictional features. (a) LFM retrace image with the LFM probe scanning perpendicular to the MoS_2 step edge, showing frictional features on both sides of the step edge. (b) LFM retrace after the sample was rotated $\sim 30°$ clockwise. Frictional features on the right side of the step edge rotate with the sample and appear nearly perpendicular to the fast scan direction. The features on the left side of the step edge, which have been rotated so that they are closer to being parallel to the fast scan direction, are no longer visible. For reference, the red arrows in (a) and (b) mark the same point on the sample. Scale bars are 10 nm.

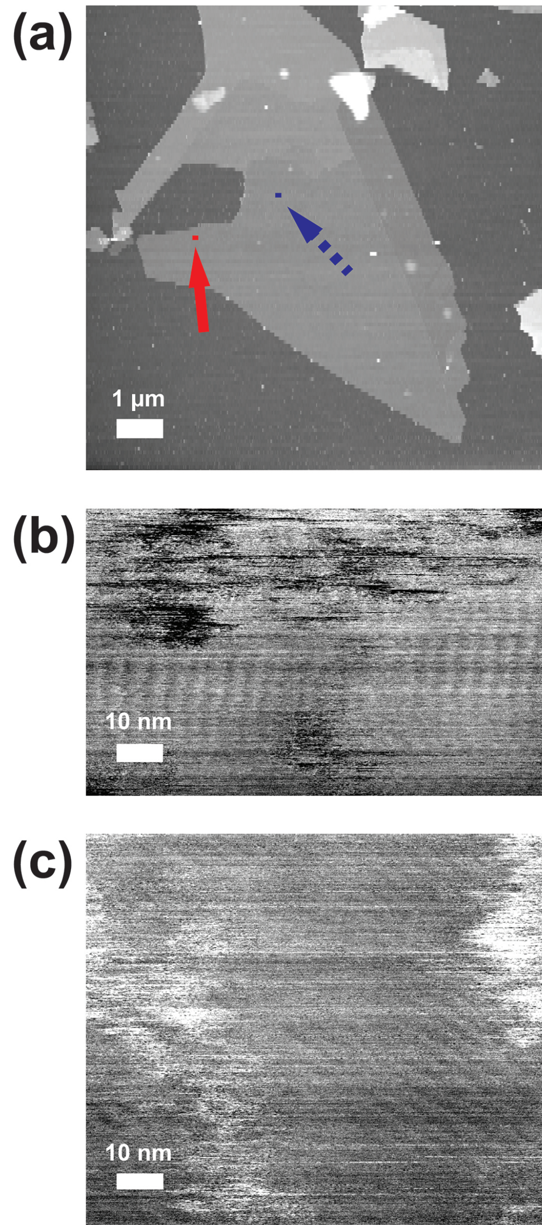

Figure 3.7: AFM and LFM images showing frictional features at various locations on a MoS_2 flake. (a) Tapping mode AFM height image of a MoS_2 flake. (b) Lateral trace image taken at the location marked by the solid red arrow showing frictional features perpendicular to the fast scan direction. (c) Lateral trace image taken at the location marked by the dashed blue arrow. The frictional features at this location appear rotated $\sim 55^{\circ}$ relative to those in (b). The data in (a)-(c) were taken at the same scan angle, with the same probe.

there are no step edges between them. Relative to the nearly vertically-oriented frictional features seen in Fig. 3.7(b), the frictional features seen in Fig. 3.7(c) are rotated $\sim 55\,°$, indicating that the orientation is not maintained on the scale of several microns.

The stripes we observe seem to arise from the actual MoS_2 and do not appear to be due to any topographical distortions of its surface, such as microscopic corrugation, wrinkles, or ripples [72–76]. Although some of our contact mode LFM measurements have a very small striped topographical signal smaller than 0.05 nm in magnitude according to simultaneously acquired AFM height measurements, it seems likely that it is a measurement artifact due to a slight crosstalk from the lateral to vertical scanning probe signal resulting from slight misalignment of the PSD [77]. If the modulated friction signal were, instead, due to an actual height variation of the MoS_2 surface, we would expect the amplitude of the modulation to increase linearly with increasing load applied by the tip, [66] in contrast to the roughly constant behavior observed in Fig. 3.5(b). Another possible artifact that we exclude is poor feedback control, where a small surface corrugation could result in a modulated F_{net} if feedback were lost yielding a spatially varying F_f. However, such an extrinsic feedback issue seems inconsistent with our measurements, as it would likely depend on scan frequency, in contrast with the results in Fig. 3.4. Moreover, estimating the variation in the frictional force using a conservative upper-bound estimate of 0.05 nm as a possible height modulation (and assuming the measured 0.022 background friction coefficient and the 0.2 N/m vertical spring constant of the cantilever) gives a value two orders of magnitude smaller for the stripes than the signal we measure with LFM. Thus, we conclude that the measured modulated frictional stripes do not appear to directly stem from surface topographical variations.

Instead, our results suggest that the striped LFM signal is due to coupling of the asperity to a modulated strain on the surface of MoS_2. Related to this possibility,

it has recently been suggested that a single asperity tip could indirectly couple *via* a puckered region to strained graphene and its resulting ripples, leading to large (micron) scale anisotropic friction [52]. Like the observed stripes we report here, that previous work did not see direct topographic evidence for any atomic- or nanoscale modulations. Instead, it was suggested that possible strain and ripples within the graphene are only detectable via a puckered region below an asperity as it slides over the surface [52]. The frictional stripes we observe seem to be consistent with a similar underlying mechanism, but with a much smaller (∼4 nm) nanoscale modulation.

The stripe features we observe on MoS_2 also have intriguing similarities to recent reports of nanoscale modulated stick-slip of an asperity dragged over a graphite surface [62, 63]. As with our results here on MoS_2, this previous work showed a modulation of the lateral signal along equally spaced parallel stripes with a length scale of approximately 4 nm. Like the report of anisotropic friction on graphene, [52] it was suggested that puckering underneath an asperity is a sensitive probe of local strain fields, which in the case of graphite results in nanoscale stick-slip events in an ordered arrangement of stripes [62, 63]. Similar to our report here and the anisotropic friction of Ref. [52], this strain field is only readily apparent through lateral force measurements, and not through direct topographical measurement. Although these are intriguing similarities between our observations and those on graphite, there is an important distinction between the two. In the case of MoS_2, evidence for stick-slip events in the vicinity of the stripes is not apparent in the experiments, as it is for graphite [62]. Moreover, we also do not see any evidence of the associated scan speed dependence observed for the stripes in graphite related to stick-slip events, [63] suggesting that we are in fact observing a modulated friction at the 4 nm scale. The source of this difference could be due to the stiffer MoS_2 layers (in comparison to graphite) that do not allow for the puckered region under an asperity to be easily caught by the tip. Despite this lack of stick slip for MoS_2, the puckering underneath

an asperity still appears in our measurements to be able to couple to the local strain resulting in a modulated friction. Overall, the surprisingly similar nanoscale spatial modulation of our lateral force and the previously reported striped stick-slip in graphite suggests there may be a common origin. Future experiments will need to determine if such nanoscale modulation is in fact a general property of such laminar materials and whether its properties can be suitably tuned for surface modification over extremely short length scales

3.4 Conclusions

In conclusion, we have observed extremely small-scale mechanical properties of the laminar material MoS_2 within the 10 nm size regime. Low-adhesion asperities have been shown to catch and flex the MoS_2 edges over a length of order 10 nm. These MoS_2 edges are found to be 20% stiffer than those of graphene, with strain energies consistent with out-of-plane bending. In the vicinity of these MoS_2 edges, we have also obtained the first experimental evidence for a modulated striped nanoscale frictional phase. These frictional stripes are modulated on the extremely small 4.1 nm length over domains greater than 100 nm. The ordered frictional stripes appear to be an intrinsic property of the MoS_2 surface layers, as the scanning properties of the asperity do not make a noticeable contribution to their modulation length. Our results suggest that the frictional stripes could be due to a modulation in the local strain in the MoS_2 that couples to the puckered region below a single asperity LFM tip. It is possible that these stripes are related to ripple strain that has been suggested as an underlying mechanism of electron scattering [73] and anisotropic friction in graphene [52].

A particularly significant aspect of our results is the fact that the ~ 4 nm length scale of the modulated friction we observe has intriguing similarities to recently reported stick-slip lateral force stripes on graphite, which are also thought to arise from coupling puckered surfaces to nanoscale strain fields [62, 63]. In addition to having

a very similar modulation length, our results and those of Refs. [62] and [63] only obtain a striped force modulation laterally, without appreciable topographic variation. This intriguing similarity raises the prospect that such ordered modulation of surface nanomechanical properties could be a general feature in the growing array of laminar materials. These results could have important implications to controlling and understanding the ultra-short nanomechanical features of MoS_2 that, due to its ubiquitous application as a dry-solid lubricant, is a promising material for future use as atomically-thin coatings to nanoscale machines. Moreover, while our work was under review we became aware of a recent manuscript posted on the arXiv [78] reporting observations of a striped phase on hexagonal BN (another laminar 2D material) and its relation to anisotropic friction which was attributed, alternatively, to surface adsorbates [79–83]. Taken together, this other work on BN and our results presented here on MoS_2, it suggests the fascinating possibility that nanoscale frictional stripes might be widely observable in the growing family of 2D materials.

Copyright© Mathias J. Boland, 2016.

Chapter 4 Nonlinear Ballistic Transport in an Atomically Thin Material[1]

4.1 Introduction

Since the advent of the electronics era, there has been a long-term trend of scaling electronic component sizes downwards in order to improve their performance and efficiency. Atomically-thin materials are ideal components of such extremely-scaled devices, [43] as these materials already have the smallest achievable thickness. Graphene, one such atomically-thin material consisting of sp^2-bonded carbon, [3] has been of particular interest for high-speed electronics [84–86]. Ultra-short graphene field effect transistors (GFETs) are promising for high speed applications due in part to their potential intrinsic nonlinear ballistic transport of charge carriers, [85–88] where the mean free path is comparable to the relevant channel length. This intrinsic nonlinear ballistic transport is determined principally by the dispersion relation (*i.e.*, the density of ballistic modes) of the material components, rather than the channel length or the extrinsic electron tunneling and transmission properties of the system, like Fabry-Perot interference effects commonly observed in phase coherent mesoscopic systems [16].

Previous work on atomically-thin materials has demonstrated nonlinearities due to diffusive drift-velocity saturation [89–92], extrinsic heating, [93] and the coupling of individual ballistic modes [94, 95]. Although the coupling of individual modes is an intrinsic ballistic effect, it is distinct from those resulting from mode density variations which have recently received attention as a way to achieve ballistic negative differential resistance (NDR) – an attractive property for ultra-short ballistic device

[1] Adapted, with permission, from Mathias J. Boland, *et al.*, *Nonlinear Ballistic Transport in an Atomically Thin Material*, ACS Nano, 2016, 10 (1), pp 1231-1239. DOI: 10.1021/acsnano.5b06546. Copyright 2016 American Chemical Society

applications, like high-speed switches and amplifiers [88]. As such, conclusive evidence of intrinsic nonlinear ballistic transport due to mode density variations in an atomically-thin material has remained elusive [85, 88, 96].

Here we show quantitative experimental evidence for intrinsic nonlinearity resulting from ballistic conduction due to a variation of the density of modes in an ultra-short channel of graphene. This behavior is shown to be distinctly different to that observed in similarly prepared ultra-short devices consisting of bilayer graphene channels. These results suggest that the addition of only one extra layer of an atomically-thin material can make a significant impact on the nonlinear ballistic behavior of ultra-short devices, which are possibly due to the very different chiral tunneling of their charge carriers [10]. We find that the nonlinear ballistic transport persists up to room temperature even while situated on a readily accessible SiO_2 substrate, making it achievable in technologically-relevant environments. Although ballistic transport has previously been reported in graphene, such behavior typical requires very low-temperatures, [97] suspended samples, [95], [98–100] or specially designed substrates [93, 101]. Moreover, ballistic behavior on a common oxide (like SiO_2) at technologically useful ambient temperatures is not typically clearly distinguishable, even for channels as short as 50 nm in length [102].

4.2 Results and Discussion

To achieve the ultra-short GFETs, as illustrated in a Fig. 4.1A, we utilize a metallic nanogap break junction positioned over either single-layer or bi-layer graphene. Such metallic nanogaps have been extensively used over the last two decades to investigate electrical conduction through single molecules and atoms [103]. To achieve the GFET structure on a solid substrate backed with a gate electrode as in Fig. 4.1A, we utilize a break junction formed through an electromigrated metallic nanogap situated on top of the single-layer and bi-layer graphene [104–106]. To avoid excessive heat dissipation

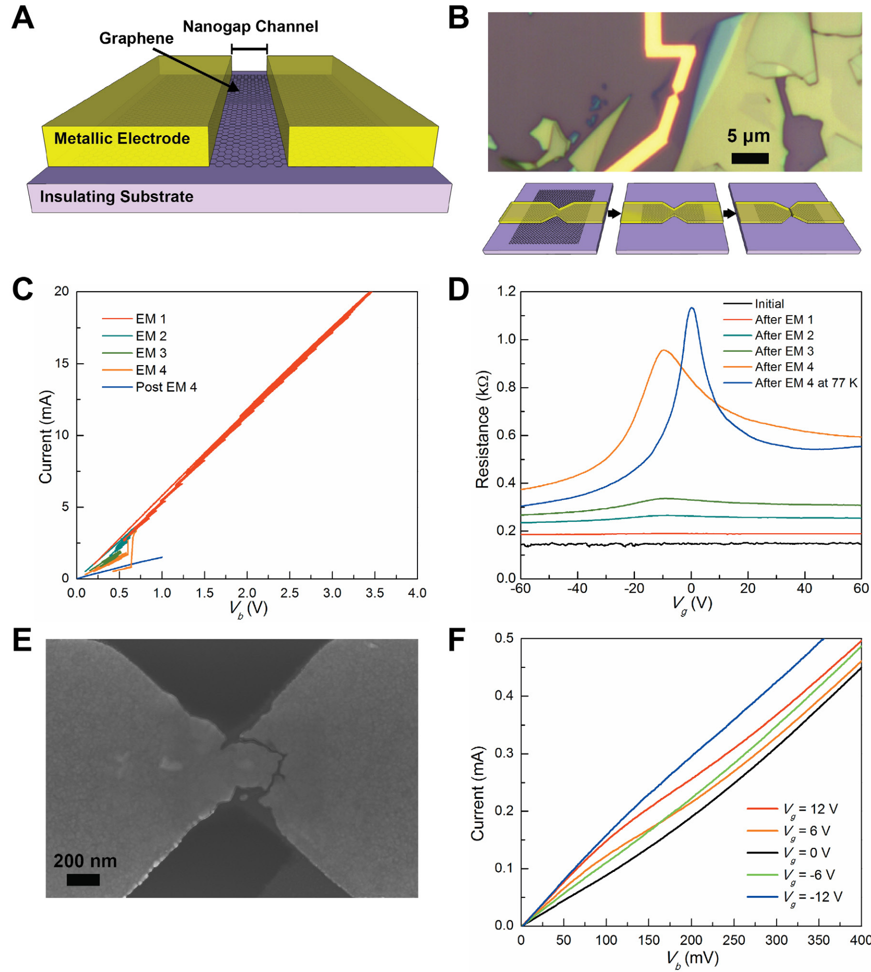

Figure 4.1: Overview and fabrication of an ultra-short channel graphene field effect transistor (GFET) (A) Schematic illustration of an ultra-short channel GFET. (B) Optical image of a Au metallic wire with a narrow (approximately 450 nm wide) constriction lithographically deposited onto the surface of a single layer of graphene. As outlined schematically below the image, the exposed graphene is etched away and a nanogap is formed using feedback controlled electromigration (FCE). (C) characteristics during FCE formation of the metallic nanogap on graphene. (D) Field effect of the device at various stages of the FCE shown in (C). (E) Scanning electron microscope image of the resulting nanogap after FCE and the electrical measurements have been performed. (F) Nonlinear current versus applied of the ultra-short GFET.

and thermal runaway during device formation, [104, 107, 108] which can damage the underlying graphene layers, we utilize feedback controlled electromigration (FCE) [104]. FCE has been shown to result in clean nanogaps with well-defined metallic interfaces [109] that can be simultaneously fabricated in parallel [110–112]. In the work we present here, the careful monitoring of the device evolution using FCE is critical to avoid damaging the underlying graphene, as large applied current densities and electric fields have previously been shown to breakdown these atomically-thin films [113–117]. The construction of the ultra-short channel GFET consists of the three-step process schematically outlined in Fig. 4.1B. First, a 30 nm thick Au nanowire with a narrow constriction is lithographically evaporated on top of exfoliated single-layer or bi-layer graphene, as shown in the optical image of a typical device in Fig. 4.1B. The sample is then plasma etched to remove exposed graphene, followed finally by application of FCE to produce a nanogap bridged only by the graphene in the vicinity of the constriction. FCE is performed by utilizing a sequence of voltage bias (V_b) ramps that slowly opens up a nanogap, [104] as shown in Fig. 4.1C for the construction of a single-layer GFET device. (See section 4.3 for details.) We monitor the progress of the nanogap graphene channel at various stages by investigating its electric field effect with a gate electrode, as shown in Fig. 4.1D for this single-layer sample. Initially, the structure shows negligible response as a function of gate voltage (V_g), but as FCE proceeds field effect becomes discernable indicating that the current is increasingly passing through the underlying graphene. Once the peak resistance of the device reaches about 800 Ω, the two-probe conductance of the device shows increased stability. At this stage, the gate dependence of the low-bias conductance is qualitatively similar to the behavior of a long-channel GFET device where a high resistance peak is observed. This behavior indicates that a metallic nanogap has fully opened and is bridged only by the underlying graphene channel. This is confirmed by a scanning electron microscope (SEM) image (taken after all the

electrical measurements discussed below have been performed) in Fig. 4.1E, which shows a nanogap between two Au electrodes on the single-layer graphene. Starting with 16 structures like that shown in Fig. 4.1B, we have successfully used FCE to form six GFETs, with four of these being robust enough to survive the high-bias investigation that follows. Although the success rate for producing GFETs with FCE is lower than for bare nanogaps, which is probably due to the possibility of damaging the underlying graphene, it is likely that the yield could be significantly improved in the future through fine tuning of the synthesis and feedback parameters.

While the low-bias behavior of the single-layer device in Fig. 4.1D resembles that of a long-channel GFET, the high-bias regime shows significant nonlinear deviations where the gate dependence diminishes, as seen in the $I-V_b$ curves in Fig. 4.1F. This is clearly observed by looking at the differential conductance as a function of V_b, shown in Fig. 4.2A at 77 K. This plot shows a low-bias conductance peak with significant gate dependence, whereas at higher biases the differential conductance loses its field effect. That is, these curves have low and high bias behaviors that are separated by a low differential-conductance quasi-saturation regime. The complete behavior of this nonlinear response as a function of gate and bias voltages can be investigated through differential conductance maps for both the 77 K (Fig. 4.2B) and room temperature (Fig. 4.2C) measurements. These differential conductance maps show that the quasi-saturation point, denoted as the value of V_b where the minimum in the differential conductance occurs, is symmetrically positioned about zero-bias and increases as the graphene channel is tuned away from it neutrality point.

Similar ultra-short devices consisting, instead, of bi-layer graphene show distinctly different nonlinear behavior, as seen in the differential conductance maps of one two such devices in Figs. 4.2D and F. In the bi-layer case, the prominent zero-bias conductance peak observed for single-layer devices is replaced by nonlinearities that more closely resemble the behavior of a conventional tunnel junction, where $\partial I/\partial V_b$ in-

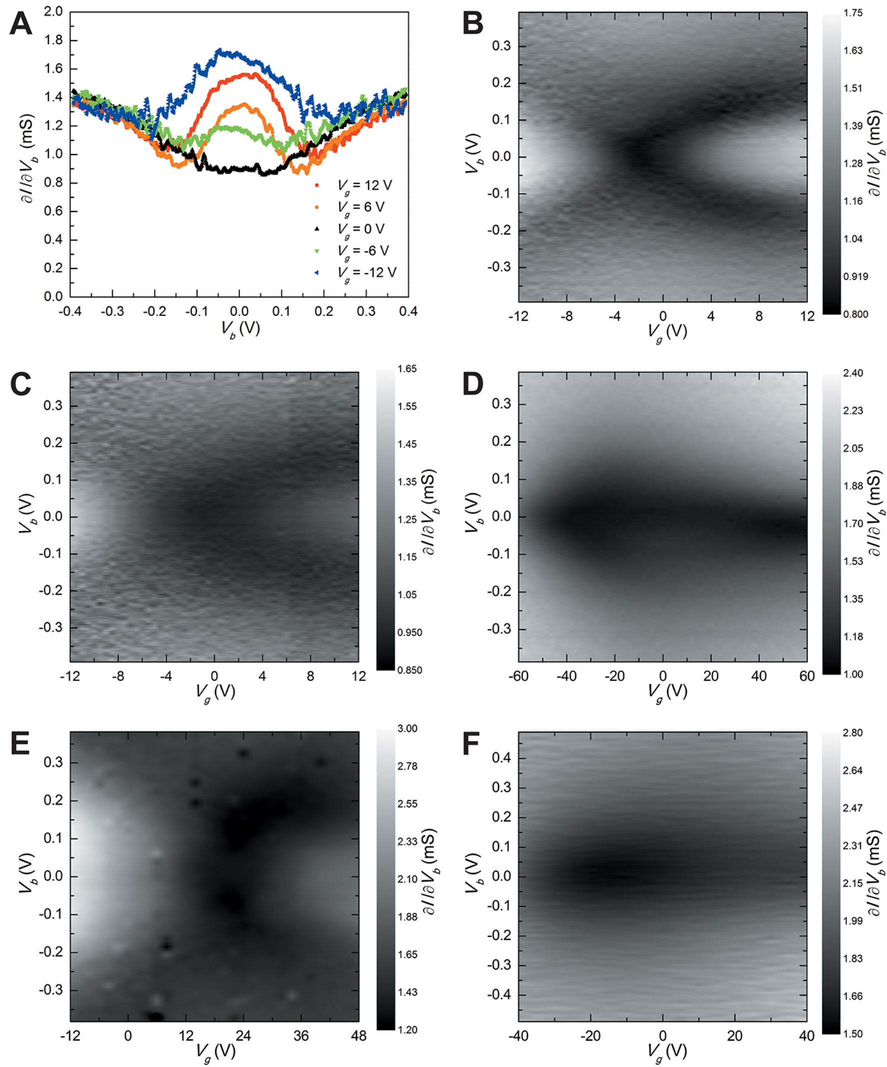

Figure 4.2: Nonlinear conductance of an ultra-short GFET. (A) Differential conductance of an ultra-short single-layer GFET for various gate voltages at 77 K. (B) Differential conductance map as a function of applied bias voltage and gate voltage at 77 K for the single-layer device in A. (C) Differential conductance map as a function of applied bias voltage and gate voltage at room temperature of 293 K for the single-layer device in A. (D) Differential conductance map as a function of applied bias voltage and gate voltage for a bi-layer GFET at 77 K showing distinct behavior compared to the single-layer device. (E) Differential conductance map as a function of bias voltage and gate voltage of a second single- layer device at 77 K showing qualitative agreement B. (F) Differential conductance map as a function of bias voltage and gate voltage of a second bilayer device at 293 K showing qualitative agreement with D.

creases as the bias voltage and (thus) the tunnel barrier is tilted [118]. We have, to date, measured in detail four nanogap GFETs, which include two single-layer and two bi-layer devices. (See Fig. 4.7 and section 4.8 for additional measurements.) Our measurements indicate that the addition of a single atomically-thin graphene layer (in going from one to two layers) makes a significant reproducible impact on the nonlinear behavior of these ultra-short devices. In the following discussion, we will focus on the behavior of one of the single-layer devices (the one shown in Fig. 4.1, Fig. 4.2B, and Fig. 4.2C) and show that the nonlinearities can be quantitatively described by an analytical model for an ultra-short ballistic graphene channel.

The observed transport characteristics of a single-layer device can be understood using the intrinsic ultra-short channel GFET ballistic model illustrated in Fig. 4.3 [88]. This intrinsic ballistic model ignores phase coherent effects, such as Fabry-Perot interference, that are not clearly discernable in our measurements. (For a more detailed discussion of possible coherent effects see section 4.9.3) In the intrinsic ballistic model we use, the graphene below the two metal electrodes acts as the source and drain to the device, with the channel consisting of the nanoscale graphene segment located in the nanogap between them, as can be seen schematically in Fig. 4.3A. These different regions are represented by the three linear graphene dispersion relations in Fig. 4.3B.

The average velocity of a state, which determines its direction, is given by $(1/\hbar)\nabla_k E$. [8] Those states in Fig. 4.3B with an average velocity having a component pointing from the source to drain are rightward going, and in the ballistic model are filled to the electrochemical potential of the source. Likewise, those states that have an average velocity component pointing in the opposite direction (*i.e.*, from drain to source) are leftward going and are only filled up to the electrochemical potential of the drain. While the states in the vicinity of the two K points of graphene have opposite pseudospin and chirality, the group velocities and filling of these two cones are equivalent

for the experimentally relevant energies close to the Dirac point. Thus, we only show one representative cone in each region of the model in Fig. 4.3. Moreover, due to the lack of scattering in a ballistic channel, the state occupation is not dependent on the location within the channel and, as a result, can be represented by the filling of a single Dirac cone.

Due to the doping of the graphene under the metallic electrodes, [119] the Fermi levels in the source and drain are offset from the neutrality point, as is depicted in Fig. 4.3B. By applying a positive gate voltage the Fermi level in the channel is increased in relation to the neutrality point, as depicted in Fig. 4.3B. The ballistic transport of such a system is specified by Landauer conduction and is determined by the minimum number of transverse modes at each relevant energy in either the source, drain, or channel (section 4.5). We assume that the metallic doping of the source and drain regions is large enough such that the channel always has the minimum number of transverse modes at all relevant energies for our experiments between the source and drain Fermi levels, μ_S and μ_D, which permits an analytic solution as a function of V_g and V_b. In this intrinsic model, when the drain voltage is increased (in going from Fig. 4.3B to Fig. 4.3C) while keeping V_g fixed, rightward going electron states are increased in the channel at the expense of leftward going states such that the total charge is kept approximately constant. The overall current, for a fixed source-drain bias voltage, is then given by the integrated number of modes between the source and drain Fermi levels. When the drain Fermi level is decreased to the point that it crosses the neutrality point of the channel the model predicts an inflection in the $I - V_b$ behavior, as is seen in the measurements in Fig. 4.2. The symmetry with respect to the source-drain voltage in the data can be understood through the ballistic model as arising from the oppositely applied V_b causing the channels neutrality point to pass the Fermi-level of the source. At larger source-drain biases the neutrality point is located between the source and drain Fermi levels (such as in Fig. 4.3D). In

this high-bias regime, the total current is relatively insensitive to the position of the neutrality point of the channel and diminished gate response beyond the inflection point is expected, in agreement with the data in Figs. 4.2A-C.

Figure 4.3E shows the calculated differential conductance map of the ballistic model as a function of bias and gate voltages. In addition to the linear dispersion of graphene, there are only three input parameters to the model two specified by well-determined geometrical aspects of the device while a third does not affect the nonlinear response. The first parameter is the transverse width of the device, which is directly measured to be 600 ± 40 nm using the image of the nanogap in Fig. 4.1E. The exact length of the nanogap (*i.e.*, the distance between the Au electrodes) appears to vary predominantly on the 10-20 nm scale over the width of the nanogap, consistent with previous reports of higher-resolution imaging of electromigrated nanogaps formed at room temperature [120]. Although the precise nanogap length is not clearly discernable in our SEM imaging, its value does not enter into the *intrinsic* ballistic behavior as long as it is short enough to maintain ballistic transport of the carriers.

The second required parameter is the gate-channel coupling which is directly given by the planar parallel plate value of $C_{ox} = 0.115\,\mathrm{fF\,\mu m^{-2}}$ for the 300 nm SiO_2 thickness used in our experiments. While sufficient gate coupling can be difficult to achieve in metallic nanogap devices, [121] we expect significant coupling over the entire width of our nanogap GFET due to the non-zero density of states in graphene and the fact that the channel is located on the same side as the gate electrode and should not be strongly screened. Supporting this view, a minimum nanogap length of ~ 0.36 nm required to achieve effective gate coupling can be estimated using the relevant density of states for graphene (see section 4.7) Since the nanogap channel should be more than an order of magnitude larger than this, we should be justified in utilizing the planar capacitance model with minimal variation of the capacitive coupling over its width due to changes in the gap length.

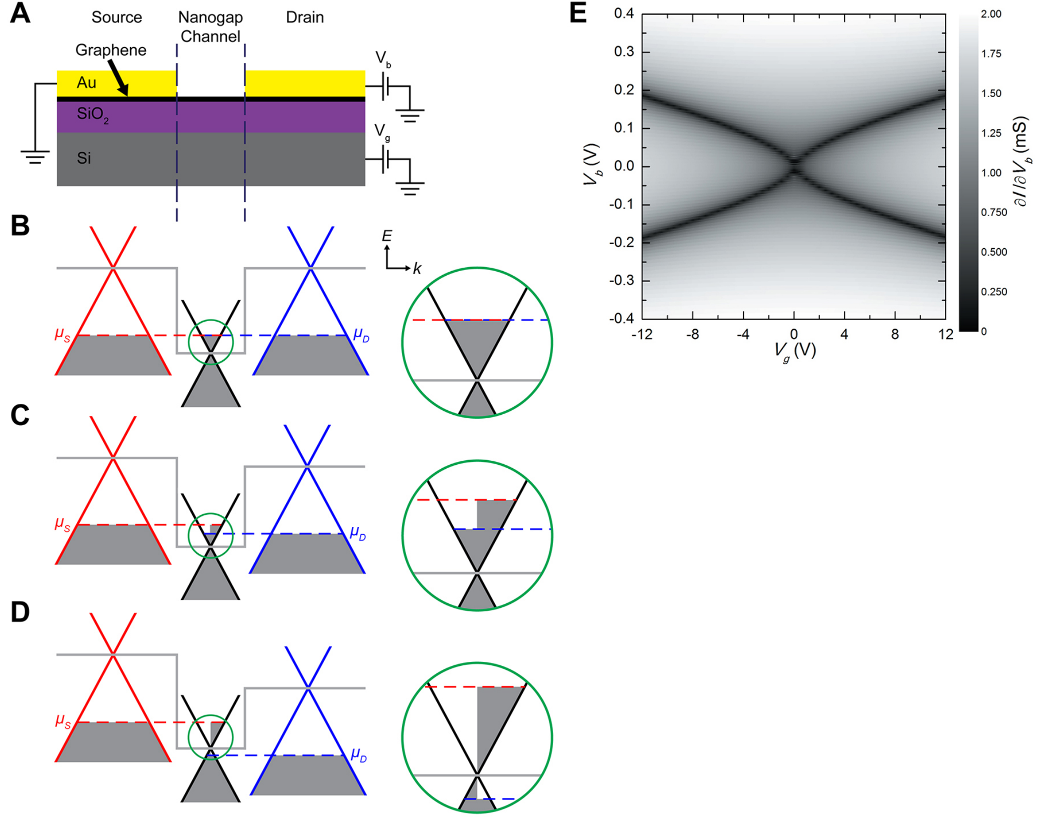

Figure 4.3: Ultra-short channel GFET ballistic model. (A) Device schematic showing the graphene nanogap channel and the source/drain contacts. V_g is applied to the doped Si substrate, while V_b is applied across the source and drain. (B) Band schematic of the three components of the ultra-short GFET. The light gray line indicates the relative locations of the graphene CNP in the source, channel, and drain. The regions circled in green are enlarged on the right for clarity. The red and blue dashed lines indicate the level of the electrochemical potentials of the source and drain, which set the quasi-Fermi levels for the rightward and leftward moving states in the channel, respectively. The source and drain are p-doped due to the overlapping metal, while the channels charge is determined by the underlying gate electrode. For a positive gate voltage, states are filled in the channel while the source and drain are held relatively constant by the metal. (C) For positive applied bias voltage, and with a fixed gate voltage, the drain Fermi-level is lowered such that the states on the channel keep the charge density approximately constant in the channel. (D) When the drain Fermi-level passes the neutrality point of the channel for high positive applied bias voltage, as shown in this illustration, the model predicts an inflection point in the $I - V_b$ behavior. (E) Calculated conductance map according to the ballistic model with an additional series resistor of $R_s = 350\ \Omega$.

In addition, the overall doping level of the nanogap channel should not affect the calculated response, apart from an overall shift in Fig. 4.3E along its horizontal gate axis. For our model calculation, we assume that the channel does not have an overall offset doping level, which is consistent with our measurements in Fig. 4.2B and reported *ab initio* calculations [122]. Although other calculations of a single thick electrode, in the vicinity of a gate, suggests that it could cause graphene to be strongly doped over long distances; [123] the actual doping is expected to be highly dependent on the overall geometry of the device. Specifically, *ab initio* computations of nanogap metallic electrode pairs with nanoscale thickness, [122] which are more relevant to our geometries, have found that doping only persists a few nanometers away from the electrode edges into the graphene channel, and that the CNP of a $\sim$ 10 nm long channel corresponds very closely to zero net doping when it is not in the immediate vicinity of a gate. Thus, the non-doped nanogap channel we model is consistent with the thinned electrodes that result from FCE-formed metallic nanogaps [109].

The final input parameter to the model is an effective series resistor R_s (chosen as 350 Ω for the calculations in Fig. 4.3E) that accounts for dissipation in the metal wire and scattering at the channel interfaces, but which does not contribute to the nonlinear behavior measured. While the value of R_s is expected to depend on the gate voltage (as discussed in section 4.9.2), a qualitative understanding of the differential conductance maps in Fig. 4.2B and Fig. 4.2C can be obtained through the use of a representative constant value for R_s of 350 Ω.

The results of the calculation using these parameters is shown in Fig. 3ED, which reproduces the salient features of the experimental data in Figs. 4.2A-C. Both show quasi-saturation that is symmetric with respect to V_b at increasing biases as V_g is increased. Moreover, like the experimental data, the calculated model reproduces the gate tunable zero-bias conductance peak experimentally measured in Figs. 4.2A-C. While the high-bias ballistic quasi-saturation model reproduces the principal features

of our ultra-short GFET, it neglects energy broadening, [88,124] which is apparent in the experiments in that the differential conductance dip is not as sharp at the inflection point as it is for the theory. Away from the inflection point, it is expected that the effects of energy broadening should be minimal, [88] and in this regime the nonlinear transport measurements can be quantitatively and unambiguously compared to the ballistic transport model, as follows.

To quantitatively compare the nonlinear transport measurements to the ballistic model, we investigate $\partial V_b/\partial I = R_S(T, V_g) + R_L(V_g + R_{NL}(V_{g,I}))$, where R_L is the low-bias linear ballistic resistance, and R_{NL} contains all the nonlinearities due to ballistic transport. Since the voltage drops across the nonlinear channel and the effective series resistance should add up to the total applied V_b, this analysis allows us to quantitatively compare the nonlinearities observed with those from the intrinsic ballistic model, without requiring prior knowledge of the value of R_S. To achieve this quantitative comparison, we compute $\partial V_b/\partial I$ from the measurements and subtract a constant resistance such that the data match the expected low-bias linear ballistic behavior. The results of this analysis for the 77 K data, at a V_g relative to the charge neutrality point of the channel (V_{CNP}) given by $V_g - V_{CNP}$ = -0.5 V, -2.5 V, and -4.5 V, are plotted in Fig. 4.5A, C, and E, and show excellent agreement with the computed ballistic nonlinearities. Moreover, the room temperature data also show excellent agreement with the same nonlinear ballistic model, as seen in Fig. 4.5B, D, and F, with just slightly increased broadening apparent in the vicinity of the inflection points. In the vicinity of the charge neutrality point of the channel (*i.e.*, when $|V_g - V_{CNP}| \lesssim 4$ V) the broadening obscures the minimum in $\partial V_b/\partial I$; however, we find that a R_s can still be subtracted from the measurements making it apparent that the high-bias nonlinearities show excellent agreement with the ballistic theory at both 77 K and room temperature, as is seen in Figs. 4.5A and 4.5B. The good agreement between the measured nonlinearities and the ballistic theory within the

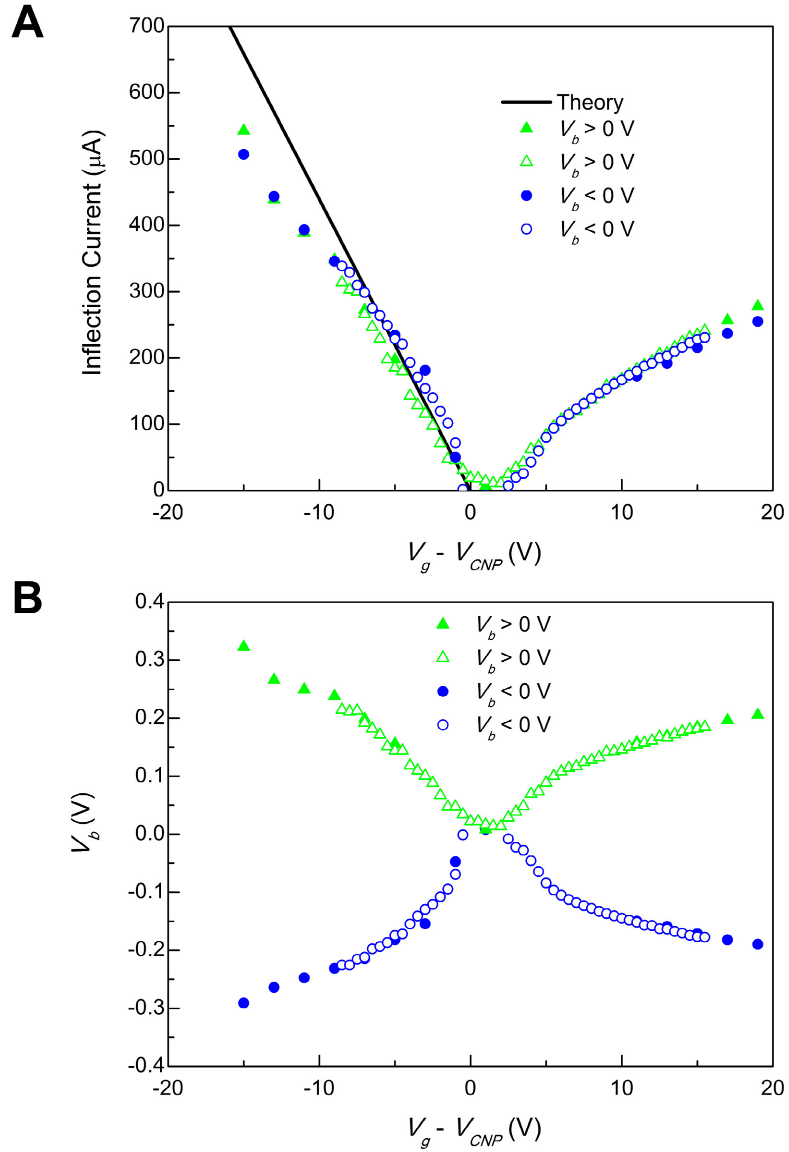

Figure 4.4: Quantitative comparison between inflection points of ultra-short GFET and the ballistic theory. We define the inflection point as the bias voltage where the $\partial V_b/\partial I$ reaches a minimum for a given gate voltage. (A) Current at the inflection point versus gate voltage for the ballistic theory (black line), and experiment (green triangles correspond to $V_b > 0$ and blue circles correspond to $V_b < 0$). Filled and hollow symbols correspond to data sets with larger and smaller gate sweep ranges, respectively. (B) Plot of V_b versus $V_g - V_{CNP}$ showing the location of the experimentally determined inflection points.

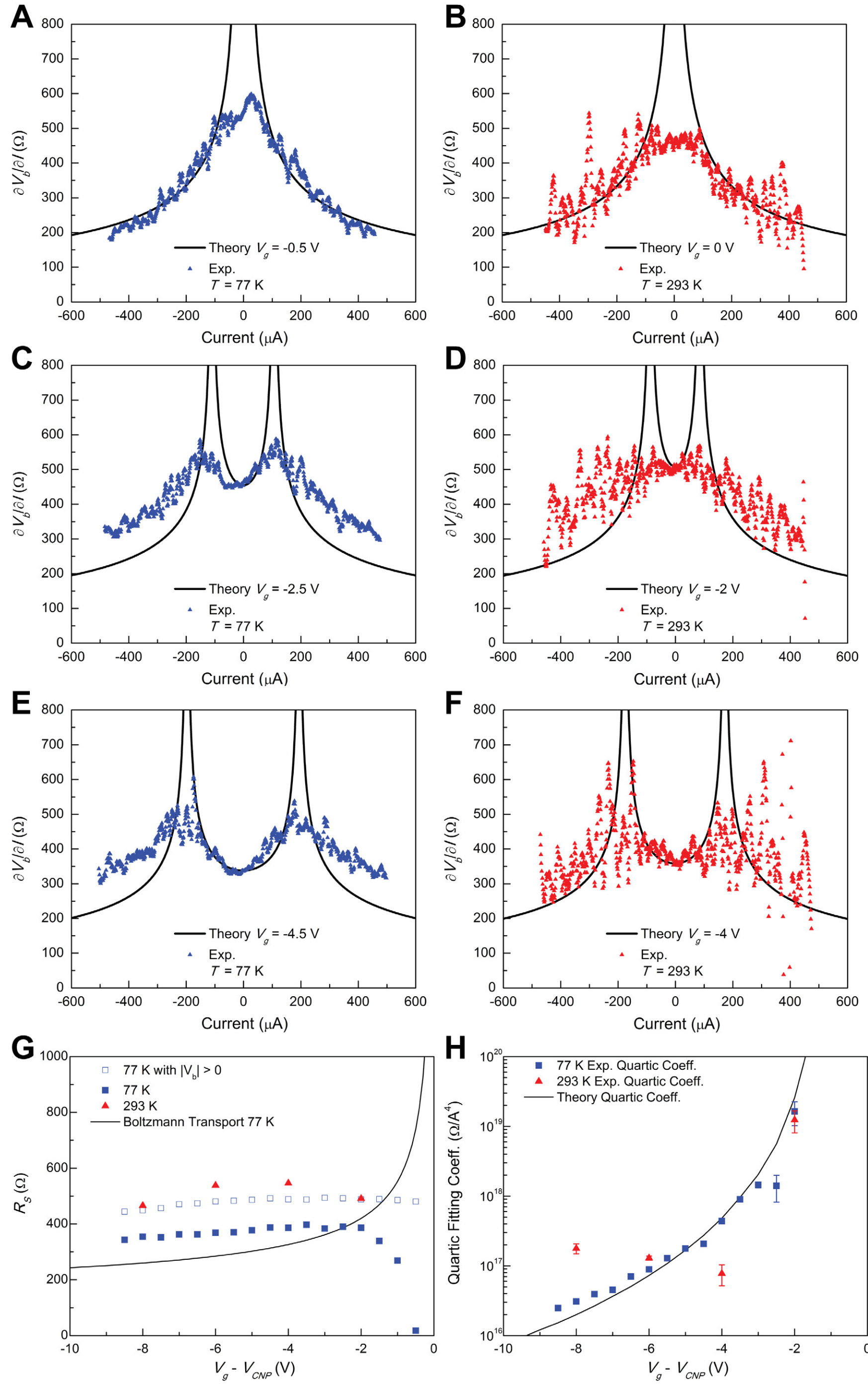

Figure 4.5: Quantitative comparison between nonlinear response of ultra-short GFET and the ballistic theory. (A-F) for the ballistic theory (solid lines) plotted against the experimentally determined values for measurements at 77 K (blue squares) and room temperature (red triangles) with a series resistance (R_S) subtracted off and plotted in (G). (H) Comparison between theory and experiment of the nonlinear quartic fitting coefficient determined within the inflection points for $V_g - V_{CNP} < 10$ V.

inflection points persists to negative gate voltages down to $\sim$ -8.5 V. Figures 4.5E and 4.5F show the excellent agreement within the inflection points at $V_g - V_{CNP} =$ -4.5 V and -4 V for 77 K and room temperature, respectively. (See section 4.8 for comparisons over the entire range.)

The subtracted R_s determined over an extended range of V_g in the above analysis is shown in Fig. 4.5G. The gate dependence of this series resistance can be understood to arise from scattering that might be expected to arise from channel interfaces that are not perfectly parallel. An estimate of the gate-dependence of the series resistance can be obtained by assuming this additional diffusive scattering is consistent with Matthiessens rule and given by the Boltzmann transport resistance of graphene (see section 4.9). Using the channel length as the mean free path in the Boltzmann resistance, in addition to the series resistance of the Au lead at 77 K, results in the solid curve shown Fig. 4.5G, which agrees with the experimentally observed gate-dependent rise of R_S as the device is tuned near its CNP.

The agreement between the measured nonlinearities and those of the intrinsic ballistic model demonstrates the important role that Klein tunneling can play in ultra-short GFETs. The ballistic model is based on the assumption that the electrons pass through the source-channel and drain-channel interfaces with near perfect transmission [88]. This near perfect transmission is a unique feature of chiral tunneling of massless carriers (known as Klein tunneling) incident perpendicularly to energy barriers, [10] as is expected for graphene when the channel is tuned near its neutrality point.

The unique features of chiral tunneling could also be the source of the distinctly different nonlinear behavior of ultra-short bi-layer graphene, as seen in the Fig. 4.2D. In bi-layer devices the chiral tunneling should be described by an exponentially decaying transmission as a function of channel length, [10] much like conventional quantum tunneling through an insulating barrier. [118] For such exponentially-decaying trans-

port, it is reasonable to expect nonlinear response similar to a standard tunnel barrier without the zero-bias peak observed in the single-layer devices (consistent with the measurements of the bi-layer devices in Fig. 4.2D and 4.2F).

For the single-layer case in the strongly n-doped regime (at large positive gate voltages) we expect reduced transmission for Klein tunneling, [125–127] which is consistent with the measured low-bias linear resistance in Fig. 4.1D. In this n-doped regime the total effective transmission (which includes effects of scattering at the channel interfaces) becomes significantly reduced, which is in stark contrast to the high constant transmission, greater than 0.4, for the p-doped case (see section 4.9.1 and Fig. 4.10). The reduction in the effective transmission when the channel is strongly n-doped for $V_g - V_{CNP} \gtrsim 8$ V corresponds well with the breakdown of the ballistic model in describing the measured nonlinearities (see section 4.8). This reduced transmission and breakdown of the nonlinear ballistic model for positive gates are likewise consistent with p-doping of the graphene in the source and drain regions under the Au, as is theoretically expected [119].

The nonlinear measurements at negative gates show excellent agreement with the intrinsic ballistic model at biases within the inflection points a regime where the transmission through each mode of the channel should be nearly perfect [10, 88]. To perform a quantitative comparison over this extended regime we compare quartic fits of the calculated and measured $\partial V_b/\partial I$. A quartic fit (of the form $\partial V_b/\partial I = R_0 + a_4 I^4$, where a_4 is the quartic fitting coefficient) captures the essential features of the nonlinearities in the ballistic model over the relevant gate range in the experiments (see section 4.8). In Fig. 4.5H we compare this quartic fit for the theory and measurements at 77 K and find that they agree with each other over a 30 V range of gate voltages (corresponding to a range of channel charge density from 9.5×10^{11} cm^{-2} to 3.1×10^{12} cm^{-2}) and $\sim$ two-orders of magnitude variation in the quartic response. Moreover, the quantitative agreement up to room temperature suggests that ballis-

tic transport effects could be achievable in ultra-short nanogap devices consisting of atomically-thin components in technologically-relevant environments, a result that has direct relevance to the goal of achieving the smallest and fastest electronics.

4.3 Methods

4.3.1 Sample Fabrication

Graphene nanogap devices were fabricated on p-doped silicon substrates with a 300 nm thick SiO_2 layer [2], as detailed in Appendix A. Graphene flakes are mechanically exfoliated from Kish graphite in dry nitrogen [128]. Graphene thickness is determined based on Raman microscopy [129, 130]. Electron beam lithography is used to define 30 nm thick gold nanowires in a bowtie geometry on top of the graphene flakes [120]. An Oxford Instruments Plasmalab80plus is used to etch away excess graphene with an O_2 plasma [106]. Electromigration of the gold electrodes is performed in a Lakeshore probe station under vacuum ($\gtrsim 4 \times 10^{-5}$ Torr) at 293 K. Computer controlled feedback is maintained during electromigration to prevent thermal damage to the underlaying graphene. Electrical measurements are performed under vacuum at both 77 K and 293 K in the same probe station.

4.3.2 Nanogap Formation

In order to open a nanogap in the gold electrodes, feedback controlled electromigration is used. This is achieved by slowly increasing the bias voltage, V_b, across a nanowire. Both current and resistance are monitored during this process [104, 110]. As the voltage increases, the current density increases, resulting in electromigration of the gold atoms in the vicinity of the bowtie, where the current density is highest. As the cross sectional area of the bow tie decreases, the resistance increases. When the resistance has increased by ~ 2 % the computer decreases the voltage by ~ 20 % to

stop the electromigration, and avoid damage to the underlying graphene. This process is repeated until a nanogap is formed, leaving a graphene channel underneath.

4.3.3 Electrical Measurements

$I - V_b$ measurements are performed by sweeping the bias voltage in 1 mV steps from −400 mV to 400 mV. The highly p-doped silicon substrate is used as a back gate, while the 300 nm SiO_2 functions as the gate dielectric. Gate voltages are kept within a ±60 V range to avoid dielectric breakdown of the SiO_2. During each $I - V_b$ sweep, the gate voltage is held at a constant value. The gate voltage is then incremented and another $I - V_b$ sweep is performed. This process is repeated over a desired gate range in order to create $I - V_b - V_g$ maps. Bias voltage is applied using a National Instruments BNC 2120 DAQ, while a Keithley 6517A is used to both measure current and to apply the gate voltage.

4.4 Gate Hysteresis

The gate response of the samples tend to have a slight hysteresis of the charge neutrality point (CNP) where the resistance is peaked, as shown in Fig. 4.6 for the sample in Fig. 4.1 of the main text at 77 K. The differential conductance maps presented throughout (such as in Fig. 4.2 of the main text) were performed by stepping V_g from negative to positive voltages, whereas the low-bias resistance plots *versus* V_g shown in Fig. 4.1D were taken with the gate stepped in the opposite direction. Thus, the CNP determined by the differential conductance maps are about 1.6 V lower in gate voltage than for the low-bias measurements in the main text.

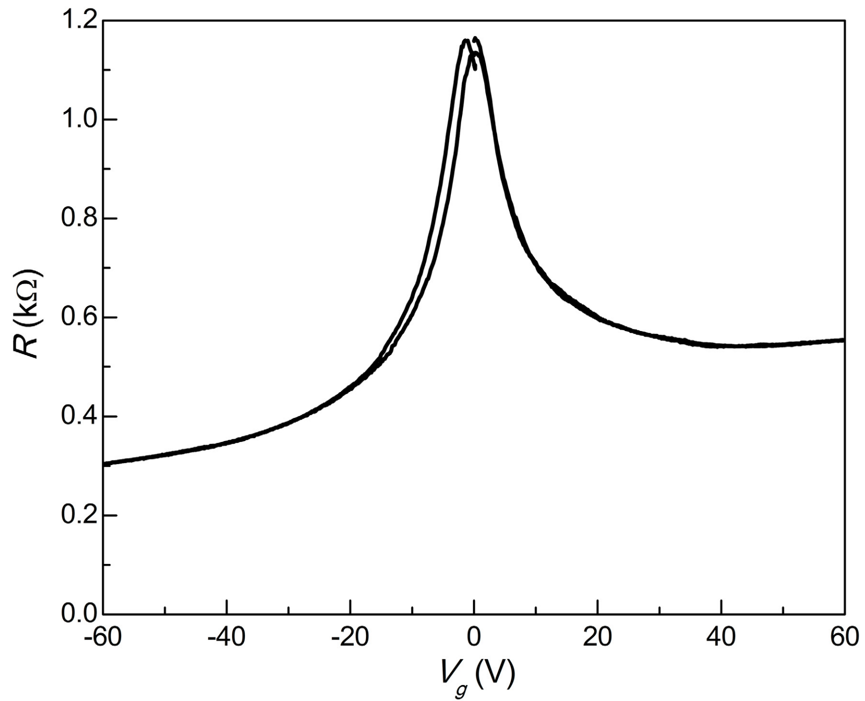

Figure 4.6: Hysteresis of low-bias behavior of samples. The low-bias resistance measured at 77 K of the sample presented in Fig. 4.1 of the main text. The measurements were initiated at $V_g = 0$ V, swept to $V_g = +60$ V, then down to $V_g =$ -60V, and finally back to $V_g = 0$ V.

4.5 Nonlinear Ballistic Model

We extend a recently proposed model [88] for an ultra-short ballistic graphene field effect transistor (GFET) appropriate for the gate coupling in our experiments. In this model, the source and drain regions are assumed to be made of a single layer graphene with a gold contact deposited on the top that effectively p-dopes the underlying graphene. The neutrality points of the source, channel, and drain regions are denoted by $E_{d,S}$, $E_{d,G}$ and $E_{d,D}$, respectively. In this model, we assume that the V_b and V_g do not strongly alter the electrode doping of the source and drain regions. This metal induced doping of graphene is incorporated in our model through a fixed energy difference ΔE_S, ΔE_D between the Fermi level and Dirac point of source and drain electrodes.

$$\Delta E_S = \mu_S - E_{d,S} \tag{4.1}$$

$$\Delta E_D = \mu_D - E_{d,D} \tag{4.2}$$

Using the Landauer formalism, [16] the ballistic current is,

$$I = \frac{2e}{h} \int_{-\infty}^{\infty} M(E)[f_S(E) - f_D(E)] \, \mathrm{d}E, \tag{4.3}$$

where e is the electron charge, $f_S(E)$ and $f_D(E)$ are the source and drain Fermi distributions with Fermi levels μ_S and μ_D respectively, and $M(E)$ is the minimum number of available transport modes in the three-component system amongst the source ($M_S(E)$), channel ($M_G(E)$), and drain regions ($M_D(E)$), *i.e.*,

$$M(E) = min[M_S(E), M_G(E), M_D(E)]. \tag{4.4}$$

The number of modes in each of the three regions is given by,

$$M_{S,G,D}(E) = \frac{2W}{\pi \hbar v_F} |E - E_{d,S,G,D}|, \tag{4.5}$$

where v_F is the graphene Fermi velocity and W is the effective width of the channel, which we have taken as 600 nm from the scanning electron microscopy image in Fig.

4.1E of the main text in order to make quantitative comparisons between theory and our experimental results.

In order to evaluate the integral in Eq. (4.3), the charge carrier density in the channel region is required, which is given by,

$$n = \int_{E_{d,G}}^{\infty} D(E)[f_S(E) + f_D(E)]\,\mathrm{d}E, \tag{4.6}$$

and,

$$p = \int_{\infty}^{E_{d,G}} D(E)[(1 - f_S(E)) + (1 - f_D(E))]\,\mathrm{d}E, \tag{4.7}$$

where $D(E)$ is the density of states in the channel given by,

$$D(E) = \frac{g_s g_v}{\pi(\hbar v_F)^2}|E - E_{d,G}|, \tag{4.8}$$

and g_s, g_v are the spin and valley degeneracy respectively.

The neutrality point of the channel $E_{d,G}$ can be computed self-consistently by a plane capacitor model given by

$$n - p = \frac{C_{ox}}{q}(-\frac{\mu_s}{q} + V_g + \frac{E_{d,G}}{q}), \tag{4.9}$$

where C_{ox}= 0.115 fF µm^{-2} is the oxide gate capacitance calculated for the 300 nm thickness SiO_2 used in our experiments.

An analytic expression for $E_{d,G}$ can be determined as a function of $\mu_D - \mu_S = -eV$ and V_g from Eqs (4.6)-(4.9), where eV is the electrochemical drop in going from the source to the drain regions. To achieve the analytic solutions we assume the zero-temperature approximation to the Fermi distributions and that the channel always has the minimum number of transverse modes at all relevant energies for our experiments between μ_S and μ_D due to the electrode doping. To simplify the solutions, we also set $\mu_S \equiv 0$, so that changes in the electrochemical potential are given by $\mu_D = -eV$. The resulting analytic solution for $E_{d,G}$ in the various possible

regimes are:

$$E_{d,G} = \frac{1}{2}[-(b-\mu_D) + \sqrt{(b-\mu_D)^2 - 2(aV_g + \mu_D^2)}], \quad 0 < \mu_D < E_{d,G}, \tag{4.10a}$$

$$E_{d,G} = \frac{\mu_D^2 - aV_g}{2(b+\mu_D)}, \quad 0 < E_{d,G} < \mu_D, \tag{4.10b}$$

$$E_{d,G} = \frac{1}{2}[-(b-\mu_D) + \sqrt{(b-\mu_D)^2 - 2(aV_g + \mu_D^2)}], \quad \mu_D < 0 < E_{d,G}, \tag{4.10c}$$

$$E_{d,G} = \frac{1}{2}[(b+\mu_D) - \sqrt{(b+\mu_D)^2 - 2(-aV_g + \mu_D^2)}], \quad E_{d,G} < 0 < \mu_D, \tag{4.10d}$$

$$E_{d,G} = \frac{1}{2}[(b+\mu_D) - \sqrt{(b+\mu_D)^2 - 2(-aV_g + \mu_D^2)}], \quad E_{d,G} < \mu_D < 0, \tag{4.10e}$$

$$E_{d,G} = -\frac{\mu_D^2 + aV_g}{2(b-\mu_D)}, \quad \mu_D < E_{d,G} < 0, \tag{4.10f}$$

where $a = 2\pi(\hbar v_F)^2 C_{ox}/e$ and $b = \pi(\hbar v_F)^2 C_{ox}/e^2$. To solve these sets of equations for arbitrary V and V_g we first specify a V_g value. For this V_g, we then determine the boundary points specified by Eq. (4.10) for the various ranges of $\mu_D = -eV$. This allows us to compute piece-wise the $E_{d,G}$ value for that specified V_g as a function of V. Once $E_{d,G}(V, V_g)$ is determined, we obtain the ballistic current $I(V, V_g)$ using Eqs. (4.3) and (4.5), assuming the channel always has the minimum number of transverse modes in comparison to the source and drain regions.

Without a series resistor (R_S), the voltage V is determined by the bias voltage to the entire device circuit, *i.e.*, $V = V_b$. However, with a non-zero series resistor, some of the applied bias voltage V_b is dropped across R_S. Since the applied bias voltage variations are $\sim$ two orders of magnitude smaller than the variations in V_g in our experiments, we assume that the voltage dropped by R_S does not appreciably alter the charge on the graphene channel. Using this assumption, we are able to account for the series resistor in our model by setting $V_b = V + I(V, V_g) \times R_S$. The calculation of $\partial I/\partial V_b$ in Fig. 4.3D has been obtained in this way using a series resistor of 350 Ω, a value consistent with the analysis of the nonlinear transport data shown in Fig. 4.5. Although the calculated nonlinear responses from theory shown in Fig. 4.5 (and below in Figs. 4.7-4.9) can include such a series resistor, we have set in those

calculations since such a resistor only results in an overall up-and-down shift of the $\partial V_b/\partial I$ curves.

4.6 Inflection points

The inflection points occur when the chemical potential of the drain, μ_D, equals the chemical potential of the channel. Equation (4.3) gives,

$$\begin{aligned} I &= \frac{2e}{h}\int_0^{\mu_S} M(E)[f_S(E) - f_D(E)]\,\mathrm{d}E, \\ &= \frac{eW\mu_S^2}{v_F(\hbar\pi)^2}. \end{aligned} \tag{4.11}$$

The carrier density in the channel is given by,

$$\begin{aligned} n &= \int_0^{\mu_S} D(E)[f_S(E) + f_D(E)]\,\mathrm{d}E, \\ &= \frac{\mu_S^2}{2\pi(\hbar v_F)^2}. \end{aligned} \tag{4.12}$$

The chemical potential,μ_S, can be solved for using Equation (4.9),

$$\begin{aligned} \frac{\mu_S^2}{2\pi(\hbar v_F)^2} &= \frac{C_{ox}V_g}{e}, \\ \mu_S &= \hbar v_F\sqrt{\frac{2\pi C_{ox}V_g}{e}}. \end{aligned} \tag{4.13}$$

A final expression for the current at the inflection point can be found by inserting Equation 4.13 into Equation 4.11,

$$I_{infl} = \frac{2v_F W C_{ox} V_g}{\pi}. \tag{4.14}$$

4.7 Gate Coupling Estimate

The gate coupling in our experiments can be understood from a rough estimate of the total electrochemical potential energy (U_{EC}) in the vicinity of the nanogap. The chemical potential energy will be defined relative to the charge neutral state of the graphene channel, ignoring any built-in potentials at the metal interfaces for

simplicity. Since the density of states of the metal electrodes is much larger than that of graphene, we will assume that changes in the chemical potential energy (U_C) are only due to variations in the charge density in the uncovered graphene channel. For simplicity, we will also assume that the density of states for the graphene channel is a constant (D) such that a value for broadened graphene near its neutrality point can be used as a conservative estimate for the gate coupling. Using this constant density of states we can write the differential increase of the chemical potential energy as

$$\mathrm{d}U_c = \Phi(N)\,\mathrm{d}N = \frac{\mathrm{d}\Phi}{\mathrm{d}N} N\,\mathrm{d}N = \frac{N}{DA}\,\mathrm{d}N, \tag{4.15}$$

where $\Phi(N)$ is the chemical potential in the graphene channel as a function of the excess number of charges N and A is the area of the channel. Equation (4.15) can be integrated to give the total chemical potential energy change,

$$U_c = \int_0^{U_C} \mathrm{d}U_c = \int_0^{N_t} \frac{N}{DA}\,\mathrm{d}N = \frac{N_t^2}{2DA} = \frac{A\sigma^2}{2De^2} \approx \frac{LW(\epsilon\mathcal{E}_G)^2}{2De^2}, \tag{4.16}$$

where N_t is the total number of excess charge carriers, σ is the charge density in the channel, L is the nanogap size, $\epsilon = \kappa\epsilon_0$ is the dielectric constant, and $\mathcal{E}_G$ is an estimate of the local electrical field in the vicinity of the channel.

The electrostatic potential energy can be estimated as that due to the field at the channel ($\mathcal{E}_G$) in a volume of order WL^2. Since the electric flux emanating from the distant gate electrode must be conserved, the field that terminates on the metal covered graphene region adjacent to the nanogap will be altered as $\mathcal{E}_G$ varies. To conserve flux, we approximate this adjacent field as $2\mathcal{E}_0 - \mathcal{E}_G$ over the same sized volume WL^2 (though located adjacent to the nanogap and not in the direct vicinity of it), where $\mathcal{E}_0$ is the field assuming a standard parallel plate capacitor model. Using this notation, if the field at the channel $\mathcal{E}_G$ is equal to $\mathcal{E}_0$, then all locations in the vicinity of the nanogap and adjacent to it will have this planar parallel plate value. Using these estimates for the electric field we can calculate the electrical potential

energy as

$$U_E \approx \frac{\epsilon}{2} W L^2 \{ \mathcal{E}_G^2 + (2\mathcal{E}_0 - \mathcal{E}_G)^2 \}. \tag{4.17}$$

The total electro-chemical potential energy can be estimated as the sum of Eqs. (4.16) and (4.17), yielding,

$$U_{EC} \approx \frac{\epsilon}{2} W L^2 \{ \mathcal{E}_G^2 + (2\mathcal{E}_0 - \mathcal{E}_G)^2 \} + \frac{LW(\epsilon \mathcal{E}_G)^2}{2De^2}. \tag{4.18}$$

For a given gate voltage, the electric field at the channel will be such that is minimized. To find this minimum condition, we take the derivative of Eq. (4.18) as a function of and set the result equal to zero, yielding the relation,

$$\mathcal{E}_G \approx \frac{2L}{2L + \frac{\epsilon}{De^2}} \mathcal{E}_0. \tag{4.19}$$

The gate response can be understood through the interplay of the two terms in the denominator of Eq. (4.19). The case where $2L < \frac{\epsilon}{De^2}$, which is appropriate for small densities of state and nanogap sizes, results in a diminished electric field at the channel in comparison to that expected for a parallel plate model, *i.e.*, $\mathcal{E}_G < \mathcal{E}_0$. This reduced field corresponds to the strongly screened case that is appropriate for single molecules located inside nanogaps, as addressed in Ref. [121].

In the opposite regime where $2L > \frac{\epsilon}{De^2}$, the field at the channel approaches the value for a planar parallel plate capacitor model. For a given density of states, we can determine the minimum nanogap size that yields the coupling of a parallel plate capacitor model as the crossover point between these two regimes, *i.e.*,

$$L_{min} \approx \frac{\epsilon}{2De^2}. \tag{4.20}$$

For nanogaps much larger than L_{min} we expect that a planar parallel plate model should be valid for describing the gate coupling to the channel. A conservative estimate for L_{min} can be achieved by using a typical broadening near the CNP of graphene in an ultra-short device (*i.e.*, $D \sim 3 \times 10^{13}$ cm^{-2}eV^{-1} taken from Ref. [88]) and the

dielectric constant of SiO_2 ($\kappa = 3.9$) in Eq. (4.20). This yields an $L_{min} \sim 0.36$ nm, which is a much smaller length than we expect for the nanogap size [120]. Thus, we should be justified in using the planar parallel plate model with uniform capacitive coupling along the entire width of the nanogap.

4.8 Detailed Comparison of Nonlinear Transport Between Experiments and Theory

In the main text we have analyzed the first derivative of the data, $\partial V_b/\partial I = R_S(T, V_g) + R_L(V_g) + R_{NL}(V_g, I)$ in order to compare the experimentally-determined nonlinearities with those from the ballistic theory. Since the linear series resistance R_S only contributes an overall up-and-down shift of the $\partial V_b/\partial I$ data, this parameter has no effect on the comparison of the measurements to the nonlinear ballistic model. The only parameters in the model that do contribute to the nonlinear response are the width and C_{ox}, which are both experimentally known quantities (as discussed in the main text). Thus, we do not have any free parameters in our comparison between the experimentally-observed nonlinearities and those predicted by the ballistic model. In principle, this comparison could alternatively be achieved by focusing on $\partial^2 V_b/\partial I^2$, since this would eliminate the linear response. However, such an alternative analysis would require taking an additional derivative of the measurements.

Figure 4.5 from the main text shows our comparison of the nonlinear transport between the experiments and the ballistic model for three applied gate voltages. A comparison over the full gate range is shown in Figs. 4.7-4.9. Figures 4.7 and 4.8 show a comparison of the experimentally determined at 77 K with the ballistic theory, while Fig. 4.9 compares the room temperature results. In both sets of measurements, the ballistic theory is seen to account well for the nonlinear response of the measurements within the inflection points over an extended range of applied gates.

To investigate the nonlinear transport over this extended range of gate voltages,

we have utilized a quartic fit in Fig. 4.5H of the main text. The form of the quartic fit is $\partial V_b/\partial I = R_0 + a_4 I^4$, where a_4 is the fitting coefficient and R_0 is a constant. The fits are performed between the two calculated inflection points, which are locations where $\partial V_b/\partial I$ diverges to infinity. To avoid comparing data close to the inflection points, a regime that is expected to be strongly affected by broadening and might also be influenced by scattering, [88, 124] we have eliminated data within 50 µA of inflection points from the least squares fitting at all gate voltages.

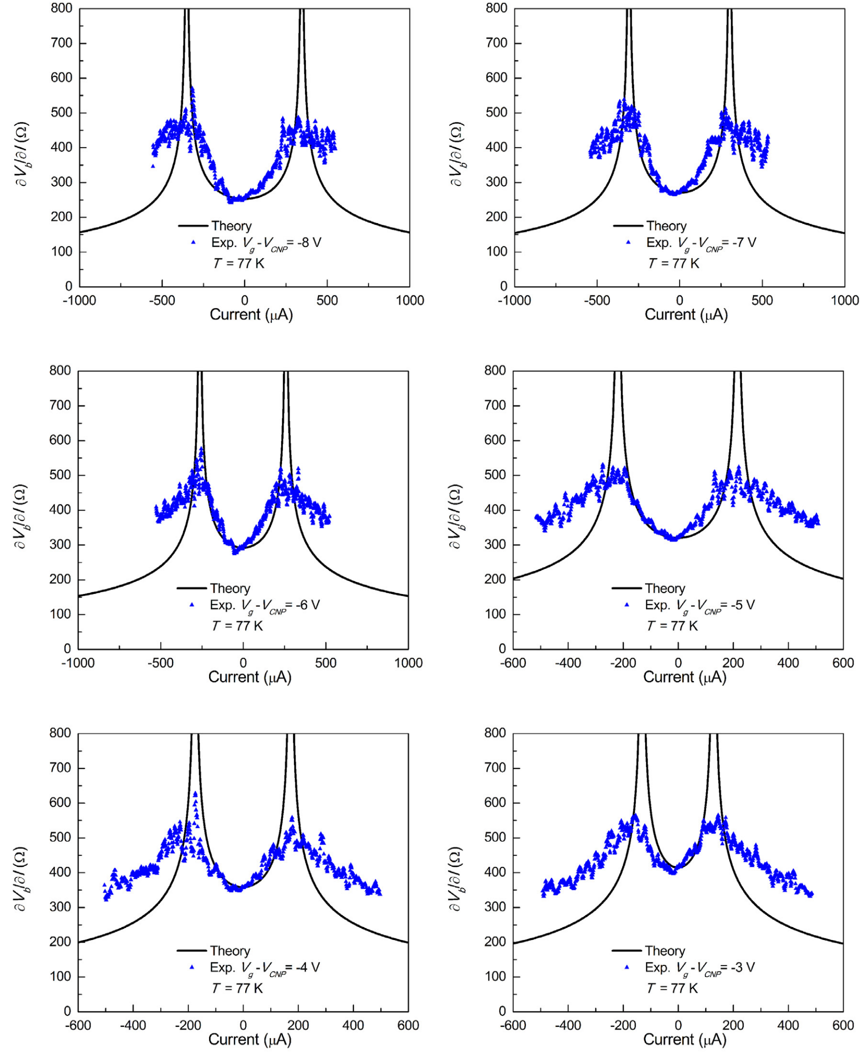

Figure 4.7: Quantitative comparison between nonlinear response of ultra-short GFET at 77 K and the ballistic theory for the range -8 V $\leq V_g - V_{CNP} \leq$ -3 V. $\partial V_b/\partial I$ for the ballistic theory (solid lines) plotted against the experimentally determined values for measurements at 77 K (blue squares) with a series resistance (R_S) subtracted off and plotted in Fig. 4.5G of the main text.

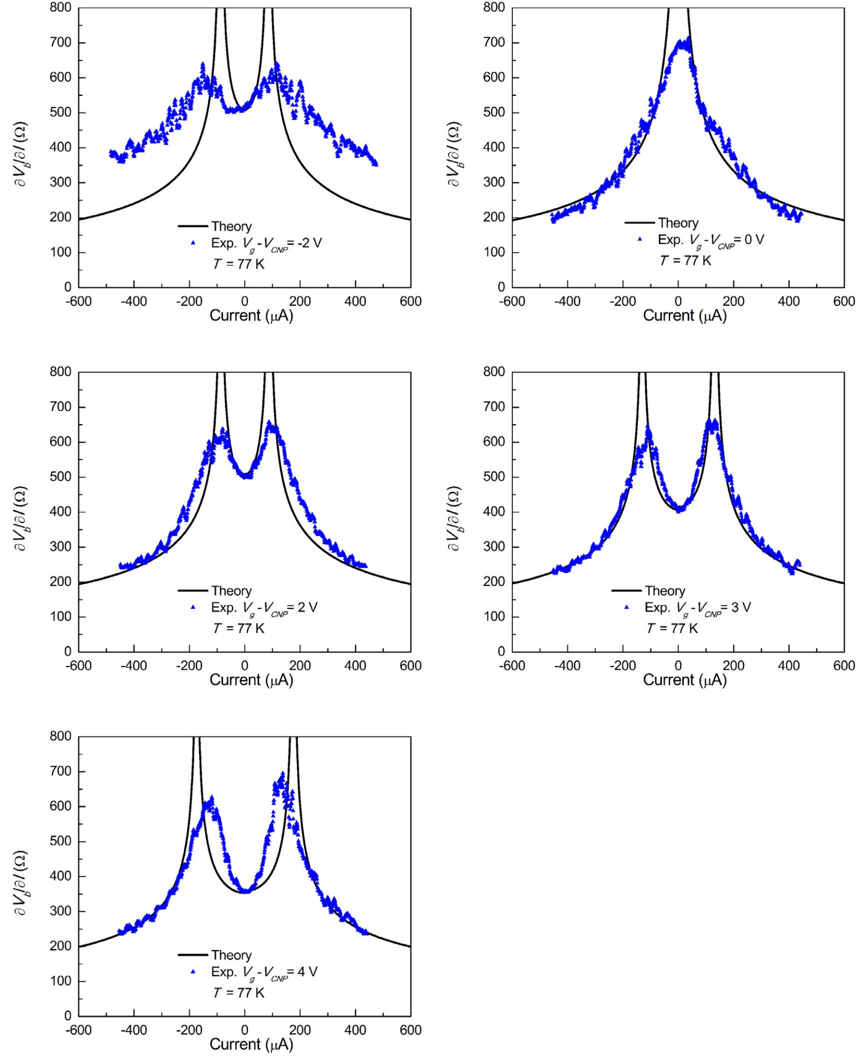

Figure 4.8: Quantitative comparison between nonlinear response of ultra-short GFET at 77 K and the ballistic theory for the range -2 V $\leq V_g - V_{CNP} \leq$ 4 V. $\partial V_b/\partial I$ for the ballistic theory (solid lines) plotted against the experimentally determined values for measurements at 77 K (blue squares) with a series resistance (R_S) subtracted off and plotted in Fig. 4.5G of the main text.

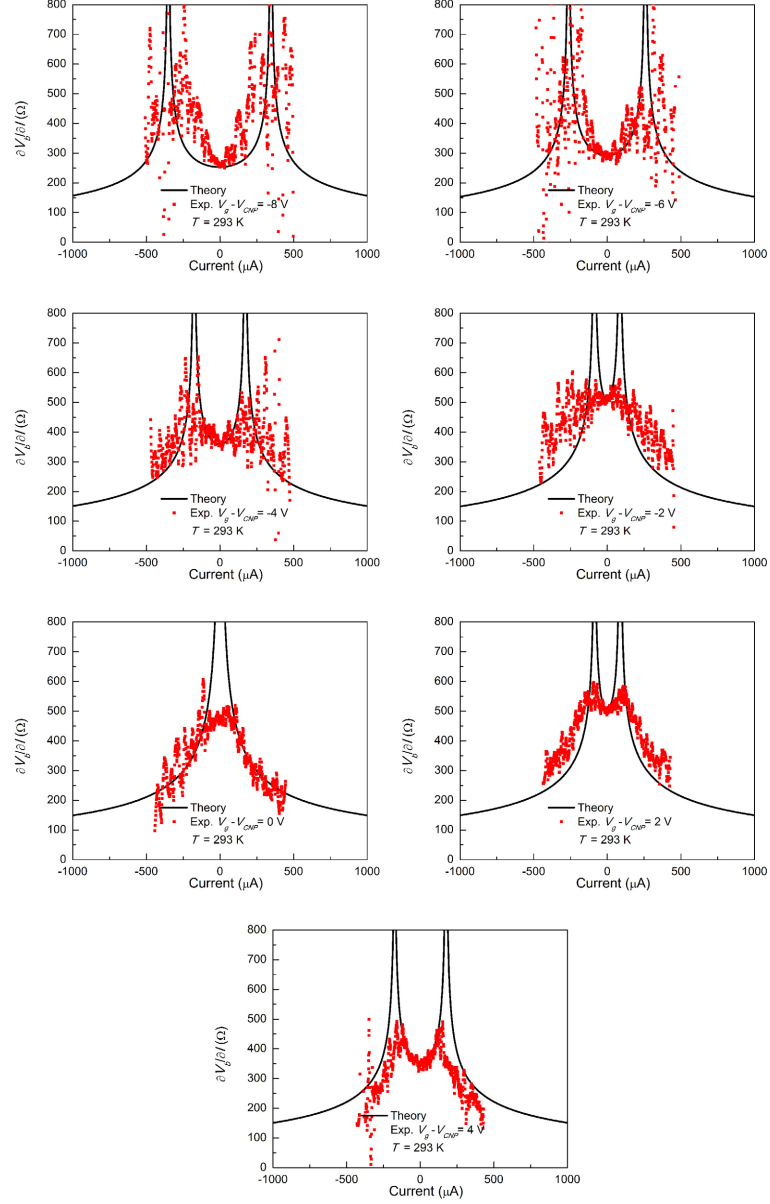

Figure 4.9: Quantitative comparison between nonlinear response of ultra-short GFET at 293 K (red triangles) and the ballistic theory for the range -8 V $\leq V_g - V_{CNP} \leq$ 4 V.

4.9 Transmission Through Device, Contact Resistance, and Discussion on Phase Coherent Effects

4.9.1 Effective Transmission Through Device

The overall transmission through the metal-graphene-metal device in Figs. 4.1 and 4.5 of the main text can be approximated as follows. First we subtract away the resistance of the gold electrode (R_{lead}) from the total two-probe low-bias resistance measured in Fig. 4.1D (*i.e.*, the orange line) after electromigration is complete. The resistance of the gold electrode is estimated as the resistance of the device before any electromigration is performed (*i.e.*, the black line in Fig. 4.1D). Using this corrected device resistance (R_{Dev}), we can determine the total effective transmission through the device as

$$\mathcal{T} = \frac{h}{2e^2 M(V_g) R_{Dev}}, \tag{4.21}$$

where $M(V_g)$ is the number of modes in the channel as a function of gate. At low-bias, the gate dependence of $M(V_g)$ is determined by setting $\mu_d = E = 0$ in Eq. (4.10) and inserting the result into Eq. (4.5), assuming the same width ($W = 600$ nm) used for the analysis shown in Fig. 4.5 of the main text. The measured effective device transmission at both room temperature and 77 K is shown in Fig. 4.10. The divergence of $\mathcal{T}$ near the CNP is likely due to broadening and puddling of the charge carriers in the graphene, and is not representative of the actual transmission. For the p-doped side (with negative applied gates) the total transmission is greater than 0.4 at both 77 K and room temperature, as seen in Fig. 4.10, while on the n-doped side the transmission decreases, suggesting that the interfaces to the source and drain are becoming increasingly opaque.

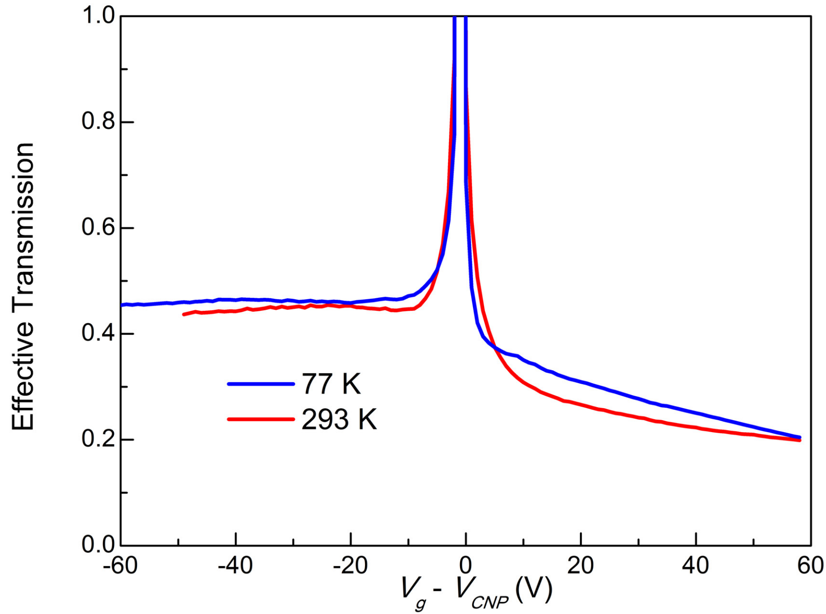

Figure 4.10: Effective device transmission of the ultra-short single-layer device in Fig. 4.1 of the main text.

4.9.2 Contact and Series Resistances

Here we will derive the relation $\partial V_b/\partial I = R_S(T, V_g) + R_L(V_g) + R_{NL}(V_g, I)$ used in the analysis of the data and show that the series resistance, R_S, should depend on both the gate voltage and the temperature.

According to the Boltzmann transport equation, [17] the resistance of a graphene segment in the diffusive limit of length L and width W is,

$$R_{Diff} = \frac{2L}{e^2 v_F^2 D(V_g)\tau W} = \frac{2L}{e^2 v_F D(V_g) l W}, \tag{4.22}$$

where τ is the relaxation time and $l = \tau/v_F$ is the mean free path. For graphene, the intrinsic low-bias linear ballistic resistance is given by

$$R_{int}(V_g) = \frac{\pi}{e^2 v_F D(V_g) W}. \tag{4.23}$$

The Boltzmann transport solution in Eq. (4.22) reverts to the intrinsic ballistic

resistance in Eq. (4.23) when the mean free path is of order the length of the graphene segment, *i.e.*, when $l = \frac{2L}{\pi} \equiv l_B$, which we call the ballistic mean free path. To account for both ballistic transport and scattering we can use Matthiessens rule to calculate l in Eq. (4.22), such that $\frac{1}{l} = \frac{1}{l_{SC}} + \frac{1}{l_B}$, where l_{SC} is the mean free path for scattering. Assuming that the metallic edge roughness at the source drain boundaries can act as scattering sites for the carriers, the scattering length can be estimated as $l_{SC} = fL$, where f is a factor that accounts for the probability of scattering at the interfaces. Using Matthiessens rule in Eq. (4.22) yields the total device resistance,

$$R_{Dev} = \frac{2}{fe^2 v_F D(V_g) W} + \frac{\pi}{e^2 v_F D(V_g) W}, \tag{4.24}$$

or,

$$R_{Dev} = R_C(V_g) + R_{int}(V_g), \tag{4.25}$$

where the first term, $R_C(V_g)$, acts as a contact resistance due to scattering off of the electrode interfaces and the second term, $R_{int}(V_g)$, is the *intrinsic* linear ballistic resistance of the channel for perfect transmission. In the low-bias linear regime (for a given applied current) the voltage across the device is given by,

$$V_{Dev} = IR_C(V_g) + IR_{int}(V_g). \tag{4.26}$$

At higher currents the intrinsic ballistic response becomes nonlinear, which can be accounted for by setting $R_{int}(V_g, I) = R_L(V_g) + \mathcal{R}_{NL}(V_g, I)$, where the term $\mathcal{R}_{NL}(V_g, I)$ contains all of the nonlinearities. Assuming the contact resistance $R_C(V_g)$ due to scattering remains linear, the total voltage across the device and the metallic leads, having $R_{lead}(T)$, is given by the bias voltage,

$$V_b = IR_{lead}(T) + IR_C(V_g) + IR_L(V_g) + I\mathcal{R}_{NL}(V_g, I). \tag{4.27}$$

Taking the partial derivative of Eq. (4.27) with respect to current yields,

$$\frac{\partial V_b}{\partial I} = R_{lead}(T) + R_C(V_g) + R_L(V_g) + \frac{\partial \{I\mathcal{R}_{NL}(V_g, I)\}}{\partial I}. \tag{4.28}$$

The last term, which contains all of the nonlinearities, can be written as $R_{NL}(V_g, I)$. In addition, the sum of the first two terms can be combined into a single series resistance $R_S(T, V_g) = R_{lead}(T) + R_C(V_g)$, which has both temperature and gate dependence. The resulting relation for the partial derivative is,

$$\frac{\partial V_b}{\partial I} = R_S(T, V_g) + R_L(V_g) + R_{NL}(V_g, I), \tag{4.29}$$

i.e., the one used in the analysis shown in Fig. (4.5) of the main text. It should be noted that as the channel is tuned to the CNP, the density of states $D(V_g)$ decreases which results in an increased value for R_S, despite the fact that the lead resistance, R_{lead}, remains constant. This increasing contact resistance as the CNP of the channel is approached is in agreement with our results in Fig. (4.5)G of the main text. Assuming that the scattering mean free path is of order the channel length gives $l_{SC} \approx L$ and $f \approx 1$ in Eq. (4.24), with a resulting series resistance of,

$$R_S(T, V_g) = \frac{2}{e^2 v_F D(V_g) W} + R_{lead}(T). \tag{4.30}$$

The initial term depends only on the width of the channel if the density of states of graphene is assumed, while the final term in Eq. (4.30) can be estimated from the initial resistance of the electrodes before they are electromigrated. Equation (4.30) is the theoretical curve labeled Boltzmann Transport 77 K in Fig. (4.5)G of the main text using the same 600 nm width assumed in other portions of the data analysis, along with an estimate of R_{lead} at a temperature of 77 K.

4.9.3 Discussion on Phase Coherent Effects

We have so far discussed the transport neglecting phase coherent effects, such as resonant tunneling and Fabry-Perot interference, [16] which we now consider. For a double-barrier ballistic system maintaining phase coherence the total transmission is

$$\mathfrak{T} = \frac{|t_1|^2 |t_2|^2}{1 + |r_1|^2 |r_2|^2 - 2|r_1||R_2| \cos(\varphi^*)}, \tag{4.31}$$

where $t_1 = |t_1|e^{i\varphi_{t1}}$, $t_2 = |t_2|e^{i\varphi_{t2}}$, $r_1 = |r_1|e^{i\varphi_{r1}}$, and $r_2 = |r_2|e^{i\varphi_{r2}}$ are the complex transmission and reflection amplitudes at each of the two barriers, and $\varphi^* = 2kL + \varphi_{r1} + \varphi_{r2}$ is the round trip phase change over the channel length L of carriers with wave vector k. (The derivation of Eq. (4.31) can be found in standard texts, such as Refs. [16] and [17].) We will consider phase coherent effects assuming that the two barriers are those at the source and drain interfaces to the uncovered graphene channel.

In the case of a p-doped channel these interfaces are nearly transparent for ballistic transport according to Klein tunneling [10]. This results in reflection amplitudes in Eq. (4.31) that are approximately zero, which makes the transmission nearly constant within this regime. This is the likely reason coherent effects are not readily apparent in our measurements for negative gate voltages (*i.e.*, within the p-doped regime).

In the strongly n-doped regime (for positive gate voltages), the interfaces between the source and drain regions and the channel become less transparent, [125] and could thus contribute to coherent effects. Insight into possible coherent effects due to these interfaces can be obtained by considering the resonant double-barrier tunneling conditions, such that $\varphi^* = 2\pi n$ with n being an integer [17]. Assuming the phase change occurs predominantly due to carriers moving through the channel, *i.e.*, $2kL \gg \varphi_{r1} + \varphi_{r2}$, the first resonant tunneling condition is $k_1 = \pi/L$. For a 10 nm long nanogap channel this gives $k_1 \approx 3.1 \times 10^8$ m^{-1}, which is approximately the value of k_F in the channel at the slight resistance minimum seen in Fig. 4.1D (77 K blue curve) for positive gates (assuming that planar parallel plate gate coupling is valid). While this agreement suggests a possible coherent effect, the Fermi energy at this gate voltage is $\approx$ -200 meV relative to the CNP (*i.e.*, very close to the expected doping level of graphene due to the Au electrode [119]). This Fermi energy suggests an alternative explanation of the resistance minimum – where the number of modes in the channel is no longer smaller than the number in the source and drain regions.

Our measurements do not currently resolve how these two possible effects conspire to produce the resistance minimum observed at positive gate voltages, nor do they resolve the way variations in the channel length along the width of the nanogap influence phase coherent effects.

4.10 Conclusions

We have shown experimental evidence for nonlinear electron transport in ultra-short single-layer graphene devices on SiO_2 substrates. This transport is shown to be distinctly different from that in similar devices incorporating bilayer channels. Comparison of the electron transport in a single-layer graphene device to theory has revealed quantitative agreement with intrinsic ballistic transport across the graphene channel up to room temperature. Moreover, this quantitative agreement up to room temperature suggests that ballistic transport effects could be achievable in ultra-short nanogap devices consisting of atomically-thin components in technologically-relevant environments, a result that has direct relevance to the goal of achieving the smallest and fastest electronics.

Copyright© Mathias J. Boland, 2016.

Chapter 5 Electrical Coupling Between Low Dimensional Nanoscale Materials

5.1 Introduction

In an effort to increase speed and efficiency in electronic devices, there has been a steady reduction in device size for the past 50 years. As device sizes have reached the nanoscale, the coupling between electrical contacts and the rest of the device becomes increasingly important. As the limitations of silicon electronics are reached, low dimensional materials may be utilized for future devices. It will then be critical to optimize the interfaces between these materials. By use atomically-thin materials as both the electrode and the channel material, there is a potential to have atomic registry between the two. This could allow for control over coherent transport at the electrode-channel interface. Coherent transport would allow for transport over extremely short lengths and very low contact resistance. These coherent transport effects should be greatest when the electrode lattice is commensurate with the channel lattice. On going and future work is focused on investigating some of these phenomena.

5.2 Electrical Contacts

In order to make a useful semiconductor device, it is necessary to contact the device with conductive electrodes. Electrical contacts usually impart an added contact resistance, which can be responsible for energy dissipation and Joule heating of the device. The International Technology Roadmap for Semiconductors identifies contact resistance as one of the limiting factor for the use of atomically thin materials in device applications [131]. Figure 5.1 shows some of the relevant parameters related to

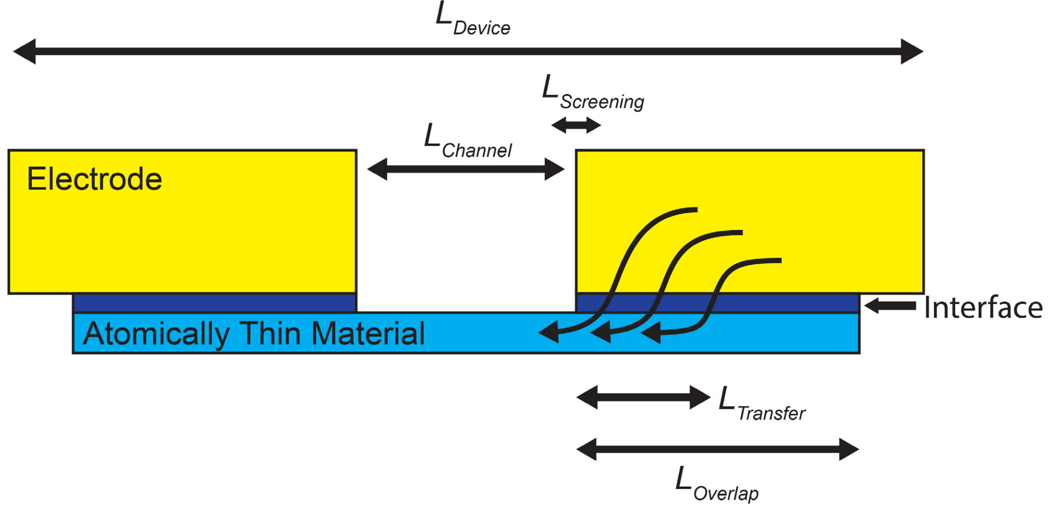

Figure 5.1: Schematic illustration of electron transfer from a metallic electrode to an atomically thin material. The total device length, L_{Device} includes the channel, $L_{Channel}$ as well as the overlap between the 2D material and the electrodes, $L_{Overlap}$. As the device is scaled down, $L_{Channel}$, $L_{Overlap}$, $L_{Transfer}$, and $L_{Screening}$ become constrained, and the specific properties of the interface become critical to device performance.

metallic contacts to a atomically-thin device. As current flows from the contact to the atomically-thin material, the current does not transfer equally over the entire overlap length. Instead, it preferentially travels towards the end of the highly conductive metal, until it transfers into the channel. The current profile is roughly,

$$I(x) \propto \exp(-\frac{x}{L_{Transfer}}), \tag{5.1}$$

where x is the distance from the edge of the contact, and $L_{Transfer}$ is the transfer length. The transfer length is given by,

$$L_{Transfer} = \sqrt{\frac{\rho_c}{R_{ch}}}, \tag{5.2}$$

where ρ_c is the contact resistivity, and R_{ch} is the channel resistance [132]. When the overlap region is made smaller than the transfer length the contact resistance increases significantly [127, 133]. Thus, in order to make very short, low power devices the transfer length plays a key role [134–136]. If the mean-free path is longer

than the transfer length, there is the possibility of ballistic transport across the contact. Contacts with transport approaching the ballistic regime have recently been achieved in graphene devices with metallic contacts in cases where the overlap length is long [6, 127]. This can allow the charge carriers to maintain phase coherence across the interface, which could result in a variety of effects such as negative differential resistance. In order to reduce the transfer length it is necessary to have very strong interfacial coupling between the electrode and the channel [132].

5.2.1 Momentum Conservation at Electrode Interfaces

One way to improve electrical coupling to electrodes is by conserving crystal momentum across the electrode interface [137]. An increase in contact resistance can result if scattering or tunneling is necessary to link the momentum of the electrode state to the channel states. However, in a crystalline system with an ordered interface, a reciprocal lattice vector of the system could cause the required momentum change. In this case, transport could remain phase coherent across the interface. Since atomically thin materials generally have strong in-plane bonding and weak out-of-plane van der Waals (vdW) bonding, they are good candidates for investigating this kind of transport. The similar crystal structure of various atomically thin materials and their vdW bonding has allowed for the creation of superlattices of these materials by stacking various components on top of one another. When the lattice constants are similar, these superlattices create a moiré pattern [138, 139]. This produces a separate reciprocal vector associated with the moiré pattern. This has recently attracted attention with the observation of the Hofstadter Butterfly in twisted bilayer graphene and graphene-BN systems [140–143]. It is possible this additional reciprocal vector could be utilized to provide the required momentum change to transfer charge across the contacts in systems with graphene contacts bridged by a graphene channel. Since the moiré pattern depends on the relative rotational orientation of

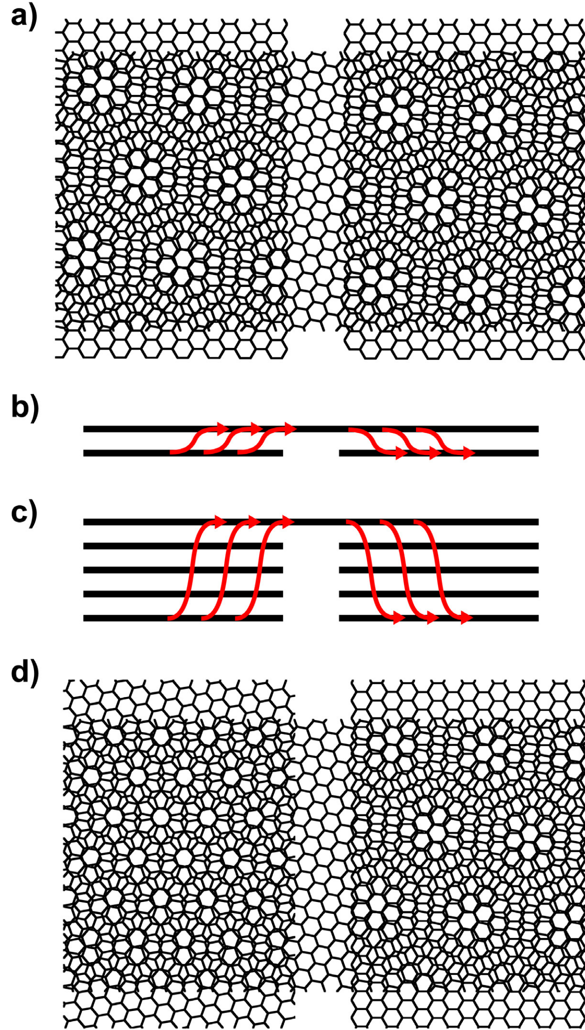

Figure 5.2: Schematic illustration of electron transfer in a graphene-graphene contact. (a) Illustration of a single layer graphene channel bridging two single layer graphene sheets as contacts. When the contacts are commensurate, the moiré pattern is periodic across the gap. (b) Electron transport between the contacts and the channel. (c) Same as (b) for a multilayer graphene channel. (d) Same as (a), but with incommensurate contacts. In this case the moiré pattern loses its' periodicity across the gap.

the graphene layers, the reciprocal lattice vector associated with it could be tuned as well. If the contacts are commensurate with each other, the moiré patter will maintain its' reciprocal lattice across the gap, potentially allowing coherent transport with enhanced coupling, as illustrated in Figure 5.2. This kind of system could be realized by transferring graphene flakes on top of nanogaps created by crystallographically etched graphene. The etched graphene acts commensurate contacts with a nanogap separating them and the transferred graphene flake acts as a channel.

5.3 Transport Between Carbon Nanotubes and Graphene

Transport between carbon nanotubes (CNTs) and graphene is predicated to strongly depend on their relative orientation [144, 145]. The very similar lattice between the two materials results in a near perfect transmission for certain alignment angles for CNTs on graphene, even with a contact overlap as small as 10 nm [127, 146].

Our group has produced crystallographically aligned etch tracks in graphene and graphite on top of an insulating SiO_2 substrate. These are formed through a catalytic etching process [147], which results in a nanogap of approximately 10 nm. Since the graphene is initially a single crystal sheet, these sample maintain commensurate lattices across the etch track. We have shown that the graphene regions separated by the etch tracks are electrically isolated with resistances $>10^{12}$ Ω. This allows the two regions of graphene to act as commensurate electrodes [147]. Furthermore, the etch tracks tend to form adjacent to one another, creating parallel nanoribbons.

We have recently grown crystallographically-aligned CNTs across graphene nanogaps through a chemical vapor deposition process [148]. In this system, the graphene regions act as electrodes and the CNT acts as a channel material. Ongoing work involves fabricating devices with these system and measuring transport through them. Through the use of a four probe STM system, located in Oak Ridge National Laboratory, we are working on directly measuring transport from a STM probe to a CNT,

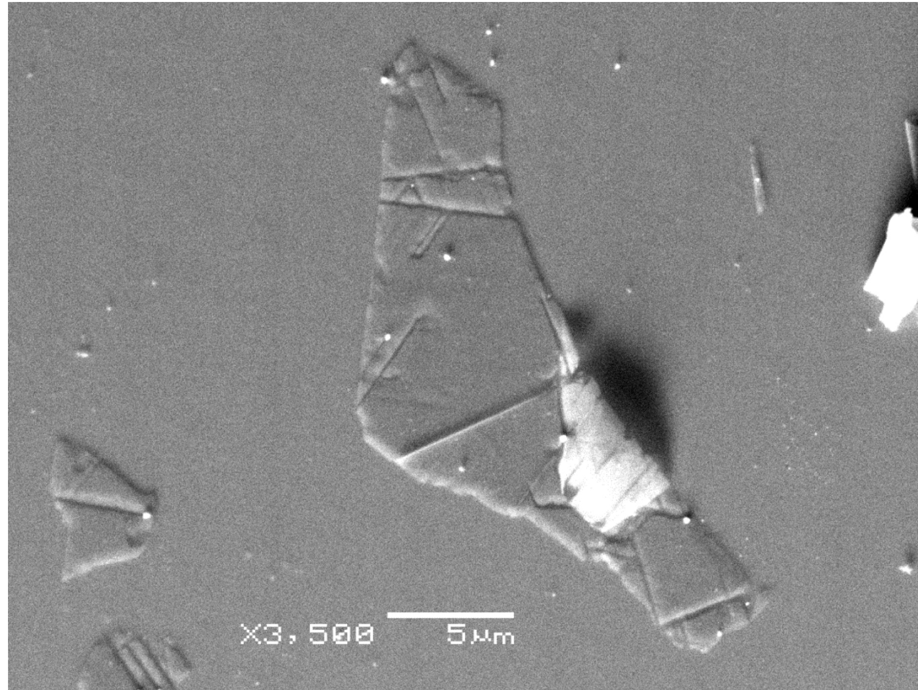

Figure 5.3: Scanning electron microscopy image of graphene with etch tracks.

and through the CNT to graphene. Figures 5.3, 5.4, and 5.5 show ongoing work in using a four probe STM to measure transport properties of such systems.

Copyright© Mathias J. Boland, 2016.

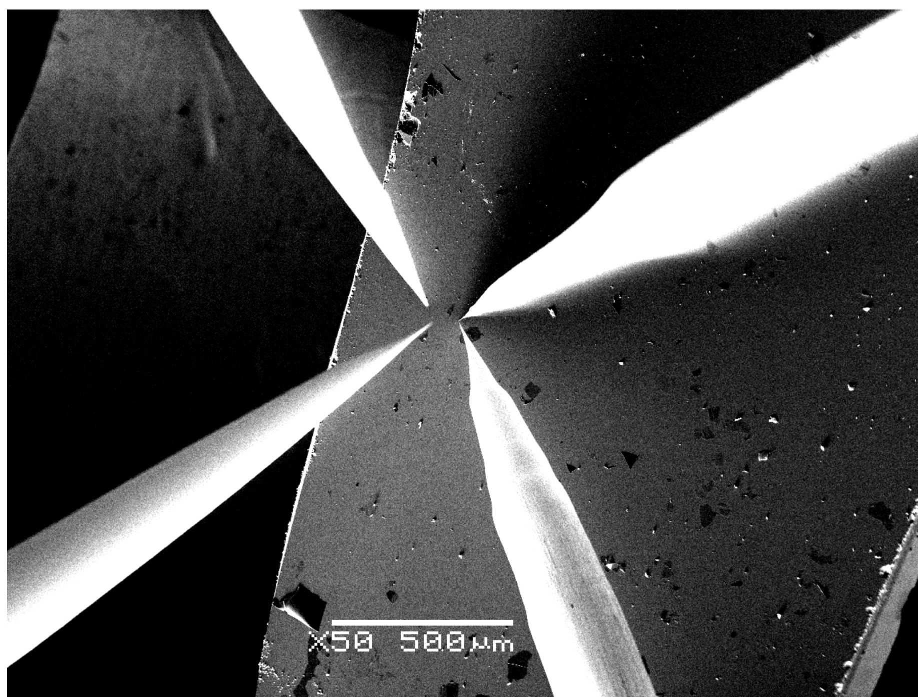

Figure 5.4: Four probe STM. In ongoing work, a four probe STM located at Oak Ridge National Laboratory is used to probe transport properties of CNTs on graphene. The four STM probes can be used to can standard STM images, but also allows four probe electrical measurements across a sample.

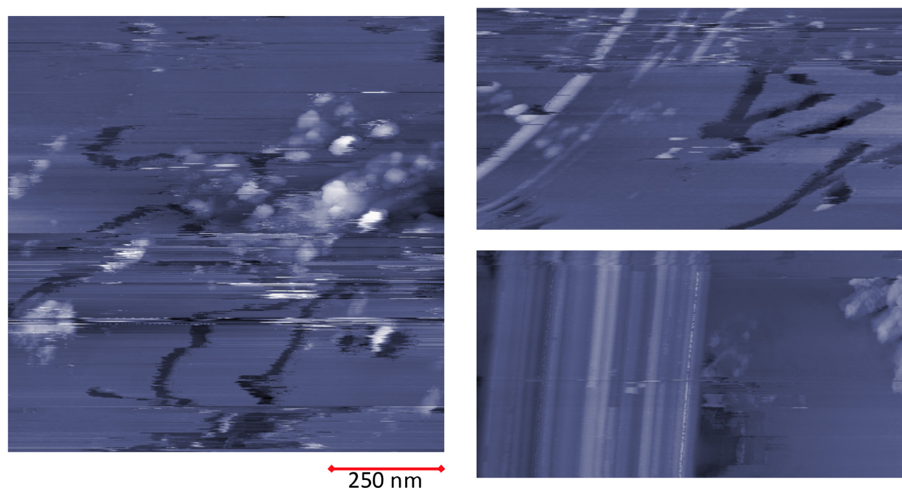

Figure 5.5: Preliminary scanning tunneling microscopy images of CNTs on graphene. Four probe STM should allow for direct measurements of electrical transport across a CNT graphene interface.

Appendix A Electron Beam Lithography

The procedure for making graphene field effect devices using the Raith e-LINE electron beam lithography system follows.

A.1 Silicon Wafer Preparation

100 mm diameter p-type silicon wafers are used. The silicon is p-doped with boron, so that the resistivity is < 0.009 ohm·cm. Both the top and bottom surfaces have an insulating 300 nm thick thermal oxide. The front surface is polished and has a crystal orientation of $\langle 100 \rangle$. As seen in Figure A.1 there are two flats cut into the sides, both along the $\langle 110 \rangle$ directions. Silicon preferentially cleaves along this direction. In order to cut the wafer into chips, a diamond scribe is used to scratch a small notch in the top surface parallel to the $\langle 110 \rangle$ at the edge of the wafer. Care should be taken to hold the scribe perpendicular to the top surface with even pressure applied. A pair of tweezers can be placed directly on either side of the the scratch. The wafer can be cleaved by lightly twisting the tweezers in opposite directions so as to break the wafer along the crystal axis. This should result in a clean, crystallographic cleave. This process can be repeated until chips of the desired size are produced (usually $\sim 2 \times 3$ cm). Compressed nitrogen gas can be used to blow off any silicon dust remaining on the chip.

Chips are cleaned by ultrasonicating in acetone, followed by isopropyl alcohol, and finally deionized water for 5 minutes each. They are then dried with compressed nitrogen. Chips are then placed into a UV ozone cleaner for 30 minutes, which removes organic contaminates and leaves a more hydrophilic surface.

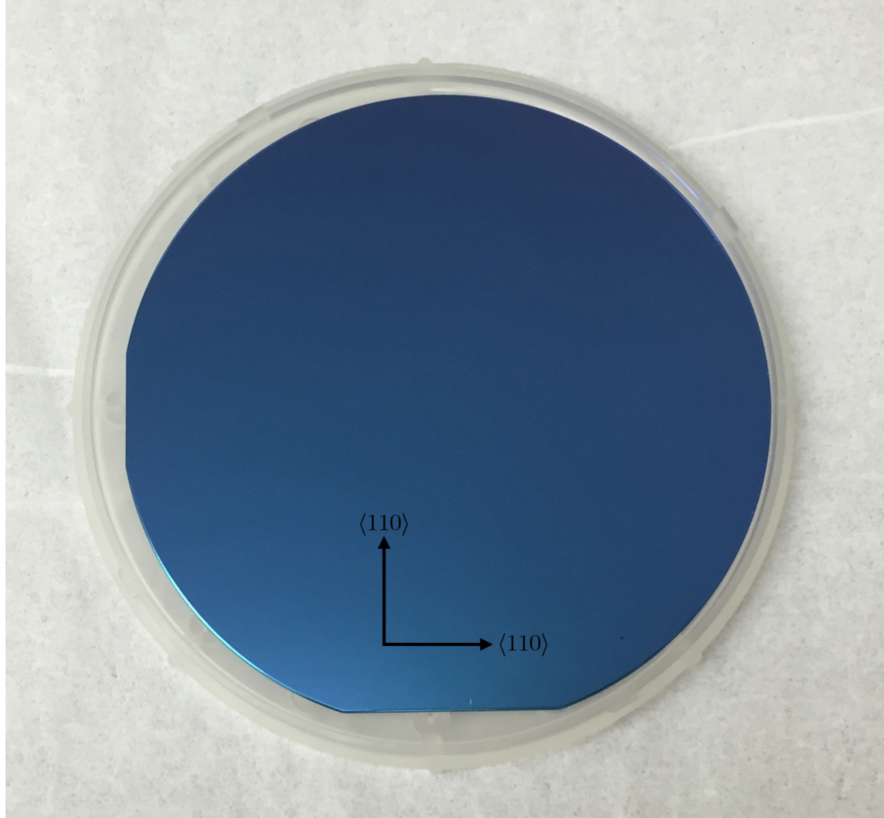

Figure A.1: Image of a ⟨100⟩ cut silicon wafer with $\sim$ 300 nm oxide layer showing ⟨110⟩ flats. The ⟨100⟩ crystal plane is orientated out of the page (normal to the wafer surface).

A.2 2D Material Preparation

Graphene (applies to other 2D laminar materials such as MoS_2) are transferred to the silicon chips through mechanical exfoliation [3, 43]. A small ($\sim 2 \times 2$ mm) flake of graphite is placed onto the sticky side of a strip of cellophane tape. The sticky side of the tape is then repeatedly pressed onto the graphite and pealed away. This process results in thinner and thinner layers of graphite. After most of the tape is covered with graphite, the tape is pressed onto a cleaned silicon chip with uniform pressure. The tape is then pealed off, leaving some of the graphite fixed to the silicon with a variety of thicknesses, all the way down to single layer graphene. The silicon chips are then placed in a chemical vapor deposition (CVD) furnace and processed

for one hour at 400 °C with gas flows of 380 sccm Ar and 340 sccm H_2 to remove tape residue.

Graphene flakes of interest are located visually using an optical microscope. Raman spectroscopy is used to confirm the thickness of the flakes based on the line shape of the graphite 2D peak. Alternatively, atomic force microscopy can be used to determine sample topography/geometry.

A.3 Lithography

There are three electron beam lithography (EBL) steps required to fabricate graphene devices. The first step is the addition of alignment marks onto the chip, the second is the fabrication of electrical contacts onto the graphene flakes, and the third is the creation of an etch mask, which is used to define the geometry of the graphene channel and remove excess graphene.

For the first step, a bi-layer of polymer resist is used as shown in Fig. 2.7. The bottom layer is a copolymer based on a mixture of methyl methacrylate and $\sim 8.5\%$ methacrylic acid (MMA (8.5) MAA) copolymer in ethyl lactate (6.9% solids). The co-polymer is spin coated onto the chip at 4000 rpm for 45 seconds and then baked on a hotplate at 150 °C for 90 seconds, resulting in a $\sim$ 150 nm thick film. Next, 950,000 molecular weight poly(methyl methacrylate) (PMMA) with 2% solids in anisole is spin coated at 4000 rpm for 45 seconds and then baked on a hotplate at 180 °C for 90 seconds, resulting in a $\sim$ 50 nm film, for a total bi-layer thickness of $\sim$ 200 nm.

The chip is then loaded into the scanning electron microscope (SEM) in order to write the alignment marks. Alignment marks are structures added to the chip to facilitate the precise alignment of overlay patterns in EBL. A plus shaped structure is written at each corner of the chip, along with a regular, labeled grid covering the chip. Three of the corner plus structures are used in subsequent EBL steps to define a coordinate transformation between the SEM stage/chip xyz-coordinates and the

electronic GDSII *uvw*-coordinates. The remaining grid structures are used to assist in the location of graphene flakes on the chip. The pattern is then written with the parameters shown in Table A.1. Note that doses listed in Table A.1 are approximate, and should be determined based on a dose test.

Table A.1: Sample EBL Parameters

	Alignment Marks	**Leads 1**	**Leads 2**	**Etch Mask**
Resist*	A2 + EL6.9	A2 + EL6.9	A2 + EL6.9	A4
Accelerating Voltage (V)	30	30	20	30
Aperture (µm)	20	20	60	20
Write Field (µm)	100	100	500	100
Step Size (µm)	0.008	0.008	0.102	0.008
Dose ($\mu A\,s\,cm^{-2}$)	235	235	180	275
Current (nA)†	0.12	0.12	3‡	0.12
Dwell Time (ms)§	0.001	0.001	0.006	0.0015
Beam Speed ($mm\ s^{-1}$)§	7.7	7.7	17	5.3

* A2 corresponds to 2% PMMA in anisole, A4 to 4% PMMA in anisole, EL6.9 to 6.9% co-polymer in ethyl lactate. For double layer process, the co-polymer is spin coated first, followed by the PMMA on top.

† Typical values.

‡ High current mode enabled.

§ Calculated based on step size, dose, and current.

A.4 Development

Following electron beam writing, the exposed resist is removed during a development procedure. Development is done by immersing the chip in solution of methyl isobutyl ketone (MIBK) and isopropyl alcohol (IPA) mixed with a ratio of 1:3 MIBK to IPA held at 21 °C for 60 seconds. It is important to keep development parameters between

dose tests and device fabrication as consistent as possible, in order to achieve consistent, high resolution patterns. After development in MIBK:IPA, the development is halted by immersing the chip in IPA, followed by deionized water for 1 minute each. The chip should then be loaded into the electron beam evaporate and put under vacuum as quickly as possible, since MIBK residue will continue to slowly remove resist, which can result in an expansion of feature size and loss of fine details.

Metal is deposited onto the sample using an electron beam evaporator. Leads are usually a $\sim$ 30 nm thick layer of gold or nickel. Gold does not adhere well to SiO_2, so a $\sim$ 1 nm thick titanium sticking layer is usually deposited first. It is important to not break vacuum between Ti and Au evaporation, as an oxide layer will begin to form on the titanium [149]. Evaporation should preferably be done at pressures $< 1 \times 10^{-6}$ Torr. Deposition rates are monitored with a crystal monitor and should be > 1 nm/min for thick films to minimize extended heating of the resists.

After metal deposition the resists are removed during liftoff by immersing the chip in 70 °C N-methyl pyrrolidone (NMP) for $\sim$ 10 min or so. The metal film sitting on top of the resist should become visibly wrinkled and begin to come off the chip. At this point a pipette can be used to gently remove the excess film with a stream of NMP. The chip is then immersed in acetone for 1 minute to fully remove any remaining resist. Acetone is removed by immersing in IPA followed by deionized water for 1 minute each. This should leave lithographically defined alignment marks on the sample.

A.5 Overlay Patterns

The lithography and development procedures are then repeated, using parameters in Table A.1, to write *Leads 1*, which are fine leads which contact the sample and *Leads 2*, which are large leads starting at leads 1 and ending in contact pads. Before designing patterns for leads 1 and 2, it is first necessary to take calibrated images

of the desired sample regions. To do this, the chip is loaded into the EBL chamber, and a three point alignment procedure is performed on the stage using the previously written alignment marks. The electron beam write field is then aligned using Raith's write field alignment procedure. Once the stage and write field are aligned, images are taken of the regions of interest on the sample. These images are recorded with their associated dimensions, angle, and position relative to the alignment marks. These can then be loaded into Raith's GDSII editor and patterns can be designed on top of them. Once patterns are designed, the chip is loaded back into the EBL chamber, the stage and write field are aligned, and the patterns are written.

In order to control the geometry of the channel, an etch mask is created by following the same procedure used for leads 1 and 2. Regions which are desired to be removed are exposed with the electron beam, so that when the resist is developed the desired channel region is protected by resist, while undesired material is exposed. The chip is then immediately loaded into a reactive ion etcher, where exposed graphene (MoS_2) is removed with an O_2 (SF_6) plasma. After etching, remaining resist is removed by immersion in Acetone, IPA, and finally deionized water.

Copyright© Mathias J. Boland, 2016.

Appendix B Lateral Force Microscopy Calibration

Calibration of lateral force microscopy (LFM) is performed through a low load procedure found in reference [53]. We first perform a thermal tune in order to find the spring constant of the cantilever. An LFM scan is then performed over a few layer sheet of graphene. Assuming a vertical adhesion, rather than the typical normal adhesion, of the probe tip results in a relationship between the lateral signal and the spatial derivative of the topography.

$$\theta = \frac{\alpha[(V_t + V_r)/2 - V_0]}{(L + A)(1 + \mu^2)}, \tag{B.1}$$

where α is the lateral calibration constant, V_t and V_r are the lateral trace and retrace signals, V_0 is a zero offset for the lateral signals, L is the applied load to the cantilever, A is the measured adhesion force, and μ is the frictional coefficient between the LFM probe and the graphene surface. The frictional coefficient for graphene is small, so that $1 + \mu^2 \approx 1$. The local incline angle, θ, is determined by the spatial derivative of the topography, which can either be acquired simultaneously with the LFM signal, or with a separate tapping mode image.

Copyright© Mathias J. Boland, 2016.

Appendix C Experimental Determination of Field Effect Mobility

Based on the Drude model of conduction, carrier mobility, μ, is given by

$$\mu = \frac{\sigma}{ne}, \tag{C.1}$$

where σ is the conductivity, n is the carrier density, and e is the elementary charge [9]. In a planar graphene field effect transistor, the applied gate voltage controls the charge carrier density on the graphene channel. This system can be approximated as a parallel plate capacitor. The carrier concentration, n, is then determined by the gate voltage, V_g, with the relation:

$$ne = cV_g, \tag{C.2}$$

where c is the capacitance per area for the gate dielectric. In general, graphene samples on SiO_2 substrates exhibit carrier doping. In this case the charge at zero gate is not zero as assumed by Equation C.2. In order to account for this, the gate voltage shift from the charge neutrality point, V_{CNP}, is used, thus replacing V_g with $V_g - V_{CNP}$. The charge neutrality point is identified as the gate voltage where the graphene has the lowest conductance. The capacitance per area can be found from

$$c = \frac{\varepsilon_0 \varepsilon_r}{t}, \tag{C.3}$$

with ε_0 being the vacuum permittivity, ε_r being the relative permittivity of the dielectric, and t being the dielectric thickness. Combining Equations (C.1), (C.2), and (C.3), we find mobility is given by

$$\mu = \frac{t}{\varepsilon_0 \varepsilon_r} \frac{\sigma}{V_g}. \tag{C.4}$$

The conductivity, σ, can be determined based on the device's four-probe conductance, $G = I/V_{4p}$, and its' geometry. Using the four-probe voltage measurement allows for

the determination of the intrinsic channel conductance without contact resistance. Sheet conductivity is then

$$\sigma = \frac{\ell}{W}G = \frac{\ell}{W}\frac{I}{V_{4p}}, \tag{C.5}$$

where ℓ is the channel length measured between the four-probe contacts and W is the channel length. Combining Equations (C.4) and (C.5) results in a final expression for the field effect mobility,

$$\mu = \frac{t}{\varepsilon_0 \varepsilon_r}\frac{\ell}{W}\frac{I}{V_{4p}V_g}, \tag{C.6}$$

which only depends on experimentally measured quantities.

Copyright© Mathias J. Boland, 2016.

References

[1] William F Brinkman, Douglas E Haggan, and William W Troutman. A history of the invention of the transistor and where it will lead us. *IEEE Journal of Solid-State Circuits*, 32(12):1858–1865, 1997.

[2] K. S. Novoselov, A. K. Geim, S. V. Morozov, D. Jiang, Y. Zhang, S. V. Dubonos, I. V. Grigorieva, and A. A. Firsov. Electric field effect in atomically thin carbon films. *Science*, 306:666–669, 2004.

[3] A. K. Geim and K. S. Novoselov. The rise of graphene. *Nature Materials*, 6:183–191, 2007.

[4] Xiaoting Jia, Jessica Campos-Delgado, Mauricio Terrones, Vincent Meunier, and Mildred S Dresselhaus. Graphene edges: a review of their fabrication and characterization. *Nanoscale*, 3(1):86–95, 2011.

[5] Mathias J Boland, Mohsen Nasseri, D Patrick Hunley, Armin Ansary, and Douglas R Strachan. Striped nanoscale friction and edge rigidity of mos 2 layers. *RSC Advances*, 5(112):92165–92173, 2015.

[6] Mathias J Boland, Abhishek Sundararajan, M Javad Farrokhi, and Douglas R Strachan. Nonlinear ballistic transport in an atomically thin material. *ACS nano*, 10(1):1231–1239, 2015.

[7] Stephanie Reich, Janina Maultzsch, Christian Thomsen, and Pablo Ordejon. Tight-binding description of graphene. *Physical Review B*, 66(3):035412, 2002.

[8] Neil W Ashcroft and N David Mermin. *Solid State Physics*. Saunders College, Philadelphia, 1976.

[9] KSA Novoselov, Andre K Geim, SVb Morozov, Da Jiang, MIc Katsnelson, IVa Grigorieva, SVb Dubonos, and AAb Firsov. Two-dimensional gas of massless dirac fermions in graphene. *nature*, 438(7065):197–200, 2005.

[10] M. I. Katsnelson, K. S. Novoselov, and A. K. Geim. Chiral tunnelling and the klein paradox in graphene. *Nature Physics*, 2(9):620–625, 2006.

[11] Kin Fai Mak, Changgu Lee, James Hone, Jie Shan, and Tony F Heinz. Atomically thin mos 2: a new direct-gap semiconductor. *Physical Review Letters*, 105(13):136805, 2010.

[12] Darshana Wickramaratne, Ferdows Zahid, and Roger K Lake. Electronic and thermoelectric properties of few-layer transition metal dichalcogenides. *The Journal of chemical physics*, 140(12):124710, 2014.

[13] LF Mattheiss. Band structures of transition-metal-dichalcogenide layer compounds. *Physical Review B*, 8(8):3719, 1973.

[14] H. E. Sliney. High temperature solid lubricants, part 1: layer lattice compounds and graphite. *Mechanical Engineering*, 96(2):18–22, 1974.

[15] F. Schwierz. Graphene transistors. *Nature Nanotechnology*, 5(7):487–496, 2010.

[16] S. Datta. *Electronic Transport in Mesoscopic Systems*. Cambridge University Press, Cambridge, UK, 1995.

[17] Charles Kittel. *Introduction to Solid State Physics*. Wiley, 8th edition, 2004.

[18] Winfried Monch. On the physics of metal-semiconductor interfaces. *Reports on Progress in Physics*, 53(3):221, 1990.

[19] J Tersoff. Schottky barrier heights and the continuum of gap states. *Physical Review Letters*, 52(6):465, 1984.

[20] Anastasia Varlet, Ming-Hao Liu, Dominik Bischoff, Pauline Simonet, Takashi Taniguchi, Kenji Watanabe, Klaus Richter, Thomas Ihn, and Klaus Ensslin. Band gap and broken chirality in single-layer and bilayer graphene. *physica status solidi (RRL)-Rapid Research Letters*, 9999, 2015.

[21] Gerd Binnig, Calvin F Quate, and Ch Gerber. Atomic force microscope. *Physical review letters*, 56(9):930, 1986.

[22] SV Kalinin and DA Bonnell. Electrostatic and magnetic force microscopy. *Scanning Probe Microscopy and Spectroscopy*, 2, 2001.

[23] NA Burnham, Xinyong Chen, CS Hodges, GA Matei, EJ Thoreson, CJ Roberts, MC Davies, and SJB Tendler. Comparison of calibration methods for atomic-force microscopy cantilevers. *Nanotechnology*, 14(1):1, 2002.

[24] John E Sader, James WM Chon, and Paul Mulvaney. Calibration of rectangular atomic force microscope cantilevers. *Review of Scientific Instruments*, 70(10):3967–3969, 1999.

[25] Michael T Postek. Critical issues in scanning electron microscope metrology. *Journal of Research-National Institute of Standards and Technology*, 99:641–641, 1994.

[26] Joseph Goldstein, DE Newbury, DC Joy, CE Lyman, P Echlin, E LIfshin, L Sawyer, and JR Michael. Scanning electron microscopy and x-ray microanalysis. 2003.

[27] K_ Kanaya and S Okayama. Penetration and energy-loss theory of electrons in solid targets. *Journal of Physics D: Applied Physics*, 5(1):43, 1972.

[28] TE Everhart and MS Chung. Idealized spatial emission distribution of secondary electrons. *Journal of Applied Physics*, 43(9):3707–3711, 1972.

[29] Thomas E Everhart and RFM Thornley. Wide-band detector for micro-microampere low-energy electron currents. *Journal of scientific instruments*, 37(7):246, 1960.

[30] David J Grant and Siva Sivoththaman. Electron-beam lithography: From past to present. 2003.

[31] I Zailer, JEF Frost, V Chabasseur-Molyneux, CJB Ford, and M Pepper. Crosslinked pmma as a high-resolution negative resist for electron beam lithography and applications for physics of low-dimensional structures. *Semiconductor science and technology*, 11(8):1235, 1996.

[32] AC Ferrari, JC Meyer, V Scardaci, C Casiraghi, Michele Lazzeri, Francesco Mauri, S Piscanec, Da Jiang, KS Novoselov, S Roth, et al. Raman spectrum of graphene and graphene layers. *Physical review letters*, 97(18):187401, 2006.

[33] F Tuinstra and J L_ Koenig. Raman spectrum of graphite. *The Journal of Chemical Physics*, 53(3):1126–1130, 1970.

[34] YuMeng You, ZhenHua Ni, Ting Yu, and ZeXiang Shen. Edge chirality determination of graphene by raman spectroscopy. *Applied Physics Letters*, 93(16):3112, 2008.

[35] Z. Rymuza. Control tribological and mechanical properties of mems surfaces. part 1: critical review. *Microsystem Technologies*, 5(4):173–180, 1999.

[36] B. Bhushan, J. N. Israelachvili, and U. Landman. Nanotribology: friction, wear and lubrication at the atomic scale. *Nature*, 374(6523):607–616, 1995.

[37] Nikhil S Tambe and Bharat Bhushan. Scale dependence of micro/nano-friction and adhesion of mems/nems materials, coatings and lubricants. *Nanotechnology*, 15(11):1561, 2004.

[38] D. Berman, S. A. Deshmukh, Skrs Sankaranarayanan, A. Erdemir, and A. V. Sumant. Macroscale superlubricity enabled by graphene nanoscroll formation. *Science*, 348(6239):1118–1122, 2015.

[39] J. Hone and R. W. Carpick. Slippery when dry. *Science*, 348(6239):1087–1088, 2015.

[40] D. Berman, A. Erdemir, and A. V. Sumant. Few layer graphene to reduce wear and friction on sliding steel surfaces. *Carbon*, 54:454–459, 2013.

[41] C. Martin-Olmos, H. M. Rasool, B. H. Weiller, and J. K. Gimzewski. Graphene mems: Afm probe performance improvement. *ACS Nano*, 7(5):4164–4170, 2013.

[42] M. M. van Wijk and A. Fasolino. Minimal graphene thickness for wear protection of diamond. *Aip Advances*, 5(1), 2015.

[43] R. F. Frindt. Superconductivity in ultrathin nbse2 layers. *Phys. Rev. Lett.*, 28(5):299–301, 1972.

[44] Consador.F and R. F. Frindt. Crystal size effects on the exciton absorption spectrum of wse2. *Physical Review B*, 2(12):4893, 1970.

[45] S. Bae, H. Kim, Y. Lee, X. F. Xu, J. S. Park, Y. Zheng, J. Balakrishnan, T. Lei, H. R. Kim, Y. I. Song, Y. J. Kim, K. S. Kim, B. Ozyilmaz, J. H. Ahn, B. H. Hong, and S. Iijima. Roll-to-roll production of 30-inch graphene films for transparent electrodes. *Nature Nanotechnology*, 5(8):574–578, 2010.

[46] C. R. Dean, A. F. Young, MericI, LeeC, WangL, SorgenfreiS, WatanabeK, TaniguchiT, KimP, K. L. Shepard, and HoneJ. Boron nitride substrates for high-quality graphene electronics. *Nat Nano*, 5(10):722–726, 2010.

[47] T. Filleter, J. L. McChesney, A. Bostwick, E. Rotenberg, K. V. Emtsev, T. Seyller, K. Horn, and R. Bennewitz. Friction and dissipation in epitaxial graphene films. *Physical Review Letters*, 102(8):086102, 2009.

[48] C. Lee, Q. Y. Li, W. Kalb, X. Z. Liu, H. Berger, R. W. Carpick, and J. Hone. Frictional characteristics of atomically thin sheets. *Science*, 328(5974):76–80, 2010.

[49] C. Lee, X. D. Wei, J. W. Kysar, and J. Hone. Measurement of the elastic properties and intrinsic strength of monolayer graphene. *Science*, 321(5887):385–388, 2008.

[50] X. Z. Liu, Q. Y. Li, P. Egberts, and R. W. Carpick. Nanoscale adhesive properties of graphene: The effect of sliding history. *Advanced Materials Interfaces*, 1(2), 2014.

[51] Z. Deng, A. Smolyanitsky, Q. Y. Li, X. Q. Feng, and R. J. Cannara. Adhesion-dependent negative friction coefficient on chemically modified graphite at the nanoscale. *Nature Materials*, 11(12):1032–1037, 2012.

[52] J. S. Choi, J. S. Kim, I. S. Byun, D. H. Lee, M. J. Lee, B. H. Park, C. Lee, D. Yoon, H. Cheong, K. H. Lee, Y. W. Son, J. Y. Park, and M. Salmeron. Friction anisotropy-driven domain imaging on exfoliated monolayer graphene. *Science*, 333(6042):607–610, 2011.

[53] D. P. Hunley, T. J. Flynn, T. Dodson, A. Sundararajan, M. Boland, and D. R. Strachan. Friction, adhesion, and elasticity of graphene edges. *Physical Review B*, 87:035417, 2013.

[54] H. Holscher, D. Ebeling, and U. D. Schwarz. Friction at atomic-scale surface steps: Experiment and theory. *Physical Review Letters*, 101(24):246105, 2008.

[55] T. Muller, M. Lohrmann, T. Kasser, O. Marti, J. Mlynek, and G. Krausch. Frictional force between a sharp asperity and a surface step. *Physical Review Letters*, 79(25):5066–5069, 1997.

[56] H. Lee, H. B. R. Lee, S. Kwon, M. Salmeron, and J. Y. Park. Internal and external atomic steps in graphite exhibit dramatically different physical and chemical properties. *ACS Nano*, 9(4):3814–3819, 2015.

[57] Z. J. Ye and A. Martini. Atomic friction at exposed and buried graphite step edges: Experiments and simulations. *Applied Physics Letters*, 106(23), 2015.

[58] P. Egberts, Z. J. Ye, X. Z. Liu, Y. L. Dong, A. Martini, and R. W. Carpick. Environmental dependence of atomic-scale friction at graphite surface steps. *Physical Review B*, 88(3), 2013.

[59] Z. J. Ye, A. Otero-de-la Roza, E. R. Johnson, and A. Martini. Effect of tip shape on atomic-friction at graphite step edges. *Applied Physics Letters*, 103(8), 2013.

[60] P. Steiner, E. Gnecco, F. Krok, J. Budzioch, L. Walczak, J. Konior, M. Szymonski, and E. Meyer. Atomic-scale friction on stepped surfaces of ionic crystals. *Physical Review Letters*, 106(18):186104, 2011.

[61] Y. L. Dong, X. Z. Liu, P. Egberts, Z. J. Ye, R. W. Carpick, and A. Martini. Correlation between probe shape and atomic friction peaks at graphite step edges. *Tribology Letters*, 50(1):49–57, 2013.

[62] M. V. Rastei, B. Heinrich, and J. L. Gallani. Puckering stick-slip friction induced by a sliding nanoscale contact. *Physical Review Letters*, 111(8), 2013.

[63] M. V. Rastei, P. Guzman, and J. L. Gallani. Sliding speed-induced nanoscale friction mosaicity at the graphite surface. *Physical Review B*, 90(4), 2014.

[64] P. E. Sheehan and C. M. Lieber. Nanotribology and nanofabrication of moo3 structures by atomic force microscopy. *Science*, 272(5265):1158–1161, 1996.

[65] S. G. Balakrishna, A. S. de Wijn, and R. Bennewitz. Preferential sliding directions on graphite. *Physical Review B*, 89(24), 2014.

[66] M. Varenberg, I. Etsion, and G. Halperin. An improved wedge calibration method for lateral force in atomic force microscopy. *Rev. Sci. Instrum.*, 74(7):3362–3367, 2003.

[67] D. F. Ogletree, R. W. Carpick, and M. Salmeron. Calibration of frictional forces in atomic force microscopy. *Review of Scientific Instruments*, 67(9):3298–3306, 1996.

[68] Valentin L. Popov. *Contact Mechanics and Friction, Physical Principles and Applications*. Springer-Verlag, Berlin Heidelberg, 2010.

[69] H. Rydberg, M. Dion, N. Jacobson, E. Schroder, P. Hyldgaard, S. I. Simak, D. C. Langreth, and B. I. Lundqvist. Van der waals density functional for layered structures. *Physical Review Letters*, 91(12), 2003.

[70] R. L. Schwoebel and E. J Shipsey. Step motion on crystal surfaces. *Journal of Applied Physics*, 37(10):3682–3686, 1966.

[71] G. Ehrlich. Atomiatomic displacements in oneand twodimensional diffusion. *Journal of Chemical Physics*, 44(3):1050–1055, 1966.

[72] C. H. Lui, L. Liu, K. F. Mak, G. W. Flynn, and T. F. Heinz. Ultraflat graphene. *Nature*, 462(7271):339–341, 2009.

[73] S. V. Morozov, K. S. Novoselov, M. I. Katsnelson, F. Schedin, L. A. Ponomarenko, D. Jiang, and A. K. Geim. Strong suppression of weak localization in graphene. *Physical Review Letters*, 97(1):016801, 2006.

[74] W. Z. Bao, F. Miao, Z. Chen, H. Zhang, W. Y. Jang, C. Dames, and C. N. Lau. Controlled ripple texturing of suspended graphene and ultrathin graphite membranes. *Nature Nanotechnology*, 4(9):562–566, 2009.

[75] A. Fasolino, J. H. Los, and M. I. Katsnelson. Intrinsic ripples in graphene. *Nature Materials*, 6(11):858–861, 2007.

[76] K. Xu, P. G. Cao, and J. R. Heath. Scanning tunneling microscopy characterization of the electrical properties of wrinkles in exfoliated graphene monolayers. *Nano Letters*, 9(12):4446–4451, 2009.

[77] M.W. Such, D.E. Kramer, and M.C. Hersam. Reproducible lateral force microscopy measurements for quantitative comparisons of the frictional and chemical properties of nanostructures. *Ultramicroscopy*, 99:189 – 196, 2004.

[78] Patrick Gallagher, Menyoung Lee, Francois Amet, Petro Maksymovych, Jun Wang, Shuopei Wang, Xiaobo Lu, Guangyu Zhang, Kenji Watanabe, and Takashi Taniguchi. One-dimensional ripple superlattices in graphene and hexagonal boron nitride. *arXiv preprint arXiv:1504.05253v2*, 2015.

[79] Daniel S Wastl, Florian Speck, Elisabeth Wutscher, Markus Ostler, Thomas Seyller, and Franz J Giessibl. Observation of 4 nm pitch stripe domains formed by exposing graphene to ambient air. *ACS nano*, 7(11):10032–10037, 2013.

[80] Srinivas Manne and Hermann E Gaub. Molecular organization of surfactants at solid-liquid interfaces. *Science*, 270(5241):1480, 1995.

[81] Erica J Wanless and William A Ducker. Organization of sodium dodecyl sulfate at the graphite-solution interface. *The Journal of Physical Chemistry*, 100(8):3207–3214, 1996.

[82] Stephan M Dammer and Detlef Lohse. Gas enrichment at liquid-wall interfaces. *Physical review letters*, 96(20):206101, 2006.

[83] Michael Seul and David Andelman. Domain shapes and patterns: the phenomenology of modulated phases. *Science*, 267(5197):476–483, 1995.

[84] J. X. Zheng, L. Wang, R. G. Quhe, Q. H. Liu, H. Li, D. P. Yu, W. N. Mei, J. J. Shi, Z. X. Gao, and J. Lu. Sub-10 nm gate length graphene transistors: Operating at terahertz frequencies with current saturation. *Scientific Reports*, 3, 2013.

[85] K. Ganapathi, Y. Yoon, M. Lundstrom, and S. Salahuddin. Ballistic i-v characteristics of short-channel graphene field-effect transistors: Analysis and optimization for analog and rf applications. *IEEE Transactions on Electron Devices*, 60(3):958–964, 2013.

[86] S. O. Koswatta, A. Valdes-Garcia, M. B. Steiner, Y. M. Lin, and P. Avouris. Ultimate rf performance potential of carbon electronics. *Ieee Transactions on Microwave Theory and Techniques*, 59(10):2739–2750, 2011.

[87] C. Pugnaghi, R. Grassi, A. Gnudi, V. Di Lecce, E. Gnani, S. Reggiani, and G. Baccarani. Semianalytical quantum model for graphene field-effect transistors. *Journal of Applied Physics*, 116(11), 2014.

[88] R. Grassi, T. Low, A. Gnudi, and G. Baccarani. Contact-induced negative differential resistance in short-channel graphene fets. *IEEE Transactions on Electron Devices*, 60(1):140–146, 2013.

[89] A. Barreiro, M. Lazzeri, J. Moser, F. Mauri, and A. Bachtold. Transport properties of graphene in the high-current limit. *Physical Review Letters*, 103(7), 2009.

[90] I. Meric, M. Y. Han, A. F. Young, B. Ozyilmaz, P. Kim, and K. L. Shepard. Current saturation in zero-bandgap, topgated graphene field-effect transistors. *Nature Nanotechnology*, 3(11):654–659, 2008.

[91] Y. Q. Wu, D. B. Farmer, W. J. Zhu, S. J. Han, C. D. Dimitrakopoulos, A. A. Bol, P. Avouris, and Y. M. Lin. Three-terminal graphene negative differential resistance devices. *ACS Nano*, 6(3):2610–2616, 2012.

[92] I. Meric, C. R. Dean, A. F. Young, N. Baklitskaya, N. J. Tremblay, C. Nuckolls, P. Kim, and K. L. Shepard. Channel length scaling in graphene field-effect transistors studied with pulsed current-voltage measurements. *Nano Letters*, 11(3):1093–1097, 2011.

[93] J. Baringhaus, M. Ruan, F. Edler, A. Tejeda, M. Sicot, A. Taleb-Ibrahimi, A. P. Li, Z. G. Jiang, E. H. Conrad, C. Berger, C. Tegenkamp, and W. A. de Heer. Exceptional ballistic transport in epitaxial graphene nanoribbons. *Nature*, 506(7488):349–354, 2014.

[94] M. J. Biercuk, N. Mason, J. Martin, A. Yacoby, and C. M. Marcus. Anomalous conductance quantization in carbon nanotubes. *Physical Review Letters*, 94(2), 2005.

[95] N. Tombros, A. Veligura, J. Junesch, M. H. D. Guimaraes, I. J. Vera-Marun, H. T. Jonkman, and B. J. van Wees. Quantized conductance of a suspended graphene nanoconstriction. *Nature Physics*, 7(9):697–700, 2011.

[96] M. Dragoman, A. Dinescu, and D. Dragoman. Negative differential resistance in graphenebased ballistic field-effect transistor with oblique top gate. *Nanotechnology*, 25(41):5, 2014.

[97] F. Miao, S. Wijeratne, Y. Zhang, U. C. Coskun, W. Bao, and C. N. Lau. Phase-coherent transport in graphene quantum billiards. *Science*, 317:1530–1533, 2007.

[98] Xu Du, Ivan Skachko, Anthony Barker, and Eva Y. Andrei. Approaching ballistic transport in suspended graphene. *Nature Nanotechnology*, 3(8):491–495, 2008.

[99] K. I. Bolotin, K. J. Sikes, Z. Jiang, M. Klima, G. Fudenberg, J. Hone, P. Kim, and H. L. Stormer. Ultrahigh electron mobility in suspended graphene. *Solid State Communications*, 146(9-10):351–355, 2008.

[100] Z. J. Qi, C. Daniels, S. J. Hong, Y. W. Park, V. Meunier, M. Drndic, and A. T. C. Johnson. Electronic transport of recrystallized freestanding graphene nanoribbons. *Acs Nano*, 9(4):3510–3520, 2015.

[101] Alexander S. Mayorov, Roman V. Gorbachev, Sergey V. Morozov, Liam Britnell, Rashid Jalil, Leonid A. Ponomarenko, Peter Blake, Kostya S. Novoselov, Kenji Watanabe, Takashi Taniguchi, and A. K. Geim. Micrometer-scale ballistic transport in encapsulated graphene at room temperature. *Nano Letters*, 11(6):2396–2399, 2011.

[102] Y. Q. Wu, V. Perebeinos, Y. M. Lin, T. Low, F. N. Xia, and P. Avouris. Quantum behavior of graphene transistors near the scaling limit. *Nano Letters*, 12(3):1417–1423, 2012.

[103] S. J. van der Molen and P. Liljeroth. Charge transport through molecular switches. *Journal of Physics-Condensed Matter*, 22(13), 2010.

[104] D. R. Strachan, D. E. Smith, D. E. Johnston, T.-H. Park, M. J. Therien, D. A. Bonnell, and A. T. Johnson. Controlled fabrication of nanogaps in ambient environment for molecular electronics. *Appl. Phys. Lett.*, 86:043109, 2005.

[105] H. Park, A. K. L. Lim, J. Park, A. P. Alivisatos, and P. L. McEuen. Fabrication of metallic electrodes with nanometer separation by electromigration. *Appl. Phys. Lett.*, 75:301 – 303, 1999.

[106] Ye Lu, Brett Goldsmith, Douglas R. Strachan, Jong Hsien Lim, Zhengtang Luo, and A. T. Charlie Johnson. High-on/off-ratio graphene nanoconstriction field-effect transistor. *Small*, 6(23):2748–2754, 2010.

[107] D. Patrick Hunley, Stephen L. Johnson, Roel L. Flores, Abhishek Sundararajan, and Douglas R. Strachan. Analytical model for self-heating in nanowire geometries. *Journal of Applied Physics*, 113(23):234306–7, 2013.

[108] G. Esen and M. S. Fuhrer. Temperature control of electromigration to form gold nanogap junctions. *Applied Physics Letters*, 87(26):263101, 2005.

[109] D. R. Strachan, D. E. Johnston, B. S. Guiton, S. S. Datta, P. K. Davies, D. A. Bonnell, and A. T. Johnson. Real-time tem imaging of the formation of crystalline nano-scale gaps. *Phys. Rev. Lett.*, 100:056805, 2008.

[110] D. E. Johnston, D. R. Strachan, and A. T. Johnson. Parallel fabrication of nanogap electrodes. *Nano Lett.*, 7:2774–2777, 2007.

[111] D.R. Ward, N.K. Grady, C.S. Levin, N.J. Halas, Y. Wu, P. Nordlander, and D. Natelson. Electromigrated nanoscale gaps for surface-enhanced raman spectroscopy. *Nano Lett.*, 7:1396–1400, 2007.

[112] Stephen L. Johnson, David P. Hunley, Abhishek Sundararajan, A. T. Charlie Johnson, and Douglas R. Strachan. High throughput nanogap formation using single ramp feedback control. *IEEE Trans. Nano.*, 10(4):806–809, 2010.

[113] Brian Standley, Wenzhong Bao, Hang Zhang, Jehoshua Bruck, Chun Ning Lau, and Marc Bockrath. Graphene-based atomic-scale switches. *Nano Letters*, 8(10):3345–3349, 2008.

[114] F. Prins, A. Barreiro, J. W. Ruitenberg, J. S. Seldenthuis, N. Aliaga-Alcalde, L. M. K. Vandersypen, and H. S. J. van der Zant. Room-temperature gating of molecular junctions using few-layer graphene nanogap electrodes. *Nano Letters*, 11(11):4607–4611, 2011.

[115] S. F. Shi, X. D. Xu, D. C. Ralph, and P. L. McEuen. Plasmon resonance in individual nanogap electrodes studied using graphene nanoconstrictions as photodetectors. *Nano Letters*, 11(4):1814–1818, 2011.

[116] J. Moser and A. Bachtold. Fabrication of large addition energy quantum dots in graphene. *Applied Physics Letters*, 95(17):173506–3, 2009.

[117] Vahid Tayari, Andrew C McRae, Serap Yigen, Joshua O Island, James M Porter, and Alexandre R Champagne. Tailoring 10 nm scale suspended graphene junctions and quantum dots. *Nano letters*, 15(1):114–119, 2014.

[118] J. G. Simmons. Generalized formula for electric tunnel effect between similar electrodes separated by a thin insulating film. *Journal of Applied Physics*, 34(6):1793, 1963.

[119] G. Giovannetti, P. A. Khomyakov, G. Brocks, V. M. Karpan, J. van den Brink, and P. J. Kelly. Doping graphene with metal contacts. *Physical Review Letters*, 101(2), 2008.

[120] D. R. Strachan, D. E. Smith, M. D. Fischbein, D. E. Johnston, B. S. Guiton, M. Drndic, D. A. Bonnell, and A. T. Johnson. Clean electromigrated nanogaps imaged by transmission electron microscopy. *Nano Lett.*, 6:441–444, 2006.

[121] S. S. Datta, D. R. Strachan, and A. T. Johnson. Gate coupling in nanoscale electronics. *Phys. Rev. B*, 79:205404, 2009.

[122] S. Barraza-Lopez, M. Vanevic, M. Kindermann, and M. Y. Chou. Effects of metallic contacts on electron transport through graphene. *Physical Review Letters*, 104(7):4, 2010.

[123] P. A. Khomyakov, A. A. Starikov, G. Brocks, and P. J. Kelly. Nonlinear screening of charges induced in graphene by metal contacts. *Physical Review B*, 82(11):115437, 2010.

[124] P. Zhao, Q. Zhang, D. Jena, and S. O. Koswatta. Influence of metal-graphene contact on the operation and scalability of graphene field-effect transistors. *Ieee Transactions on Electron Devices*, 58(9):3170–3178, 2011.

[125] T. Low, S. Hong, J. Appenzeller, S. Datta, and M. S. Lundstrom. Conductance asymmetry of graphene p-n junction. *IEEE Transactions on Electron Devices*, 56(6):1292–1299, 2009.

[126] B Huard, JA Sulpizio, N Stander, K Todd, B Yang, and D Goldhaber-Gordon. Transport measurements across a tunable potential barrier in graphene. *Physical review letters*, 98(23):236803, 2007.

[127] F. N. Xia, V. Perebeinos, Y. M. Lin, Y. Q. Wu, and P. Avouris. The origins and limits of metal-graphene junction resistance. *Nature Nanotechnology*, 6(3):179–184, 2011.

[128] Abhishek Sundararajan, Mathias J Boland, D Patrick Hunley, and Douglas R Strachan. Doping and hysteretic switching of polymer-encapsulated graphene field effect devices. *Applied Physics Letters*, 103(25):253505, 2013.

[129] A. C. Ferrari, J. C. Meyer, V. Scardaci, C. Casiraghi, M. Lazzeri, F. Mauri, S. Piscanec, D. Jiang, K. S. Novoselov, S. Roth, and A. K. Geim. Raman spectrum of graphene and graphene layers. *Phys. Rev. Lett.*, 97:187401, 2006.

[130] A. Gupta, G. Chen, P. Joshi, S. Tadigadapa, and P.C. Eklund. Raman scattering from high-frequency phonons in supported n-graphene layer films. *Nano Lett.*, 6:2667 – 2673, 2006.

[131] Emerging research materials. *International Technology Roadmap for Semiconductors*, 2011.

[132] François Léonard and A Alec Talin. Electrical contacts to one-and two-dimensional nanomaterials. *Nature nanotechnology*, 6(12):773–783, 2011.

[133] Aaron D Franklin and Zhihong Chen. Length scaling of carbon nanotube transistors. *Nature nanotechnology*, 5(12):858–862, 2010.

[134] K Nagashio, T Nishimura, K Kita, and A Toriumi. Metal/graphene contact as a performance killer of ultra-high mobility graphene analysis of intrinsic mobility and contact resistance. In *2009 IEEE International Electron Devices Meeting (IEDM)*, pages 1–4. IEEE, 2009.

[135] Aaron D Franklin, Shu-Jen Han, Ageeth A Bol, and Wilfried Haensch. Effects of nanoscale contacts to graphene. *IEEE Electron Device Letters*, 32(8):1035–1037, 2011.

[136] B Huard, N Stander, JA Sulpizio, and D Goldhaber-Gordon. Evidence of the role of contacts on the observed electron-hole asymmetry in graphene. *Physical Review B*, 78(12):121402, 2008.

[137] J Tersoff. Contact resistance of carbon nanotubes. *Applied Physics Letters*, 74(15):2122–2124, 1999.

[138] Shujie Tang, Haomin Wang, Yu Zhang, Ang Li, Hong Xie, Xiaoyu Liu, Lianqing Liu, Tianxin Li, Fuqiang Huang, Xiaoming Xie, et al. Precisely aligned graphene grown on hexagonal boron nitride by catalyst free chemical vapor deposition. *arXiv preprint arXiv:1309.0172*, 2013.

[139] Jiaqi He, Nardeep Kumar, Matthew Z Bellus, Hsin-Ying Chiu, Dawei He, Yongsheng Wang, and Hui Zhao. Electron transfer and coupling in graphene–tungsten disulfide van der waals heterostructures. *Nature communications*, 5, 2014.

[140] CR Dean, L Wang, P Maher, C Forsythe, F Ghahari, Y Gao, J Katoch, M Ishigami, P Moon, M Koshino, et al. Hofstadter/'s butterfly and the fractal quantum hall effect in moire superlattices. *Nature*, 497(7451):598–602, 2013.

[141] B Hunt, JD Sanchez-Yamagishi, AF Young, M Yankowitz, Brian J LeRoy, K Watanabe, T Taniguchi, P Moon, M Koshino, P Jarillo-Herrero, et al. Massive dirac fermions and hofstadter butterfly in a van der waals heterostructure. *Science*, 340(6139):1427–1430, 2013.

[142] LA Ponomarenko, RV Gorbachev, GL Yu, DC Elias, R Jalil, AA Patel, A Mishchenko, AS Mayorov, CR Woods, JR Wallbank, et al. Cloning of dirac fermions in graphene superlattices. *Nature*, 497(7451):594–597, 2013.

[143] R Bistritzer and AH MacDonald. Moiré butterflies in twisted bilayer graphene. *Physical Review B*, 84(3):035440, 2011.

[144] Ahmed A Maarouf and Eugene J Mele. Low-energy coherent transport in metallic carbon nanotube junctions. *Physical Review B*, 83(4):045402, 2011.

[145] Alper Buldum and Jian Ping Lu. Contact resistance between carbon nanotubes. *Physical Review B*, 63(16):161403, 2001.

[146] Ravi S Sundaram, Mathias Steiner, Hsin-Ying Chiu, Michael Engel, Ageeth A Bol, Ralph Krupke, Marko Burghard, Klaus Kern, and Phaedon Avouris. The graphene–gold interface and its implications for nanoelectronics. *Nano letters*, 11(9):3833–3837, 2011.

[147] D Patrick Hunley, Abhishek Sundararajan, Mathias J Boland, and Douglas R Strachan. Electrostatic force microscopy and electrical isolation of etched few-layer graphene nano-domains. *Applied Physics Letters*, 105(24):243109, 2014.

[148] D Patrick Hunley, Mathias J Boland, and Douglas R Strachan. Integrated nanotubes, etch tracks, and nanoribbons in crystallographic alignment to a graphene lattice. *Advanced Materials*, 27(5):813–818, 2015.

[149] MJ Mindel and SR Pollack. The room temperature oxidation of titanium thin films. *Acta Metallurgica*, 17(12):1441–1448, 1969.

Vita

MATHIAS J. BOLAND

EDUCATION

University of Kentucky, Lexington, Kentucky
Thesis advisor: Professor Douglas R. Strachan
Research Focus: Synthesis and characterization of nanoscale materials and devices
M.S. in Physics (2014)

The Ohio State University, Columbus, Ohio
B.S. in Physics (2010)

PROFESSIONAL EXPERIENCE

- **Graduate Research Assistant,** University of Kentucky (2012 – Present)
- **Teaching Assistant,** Department of Physics and Astronomy, University of Kentucky (2010 – 2016)

PUBLICATIONS

1. **Mathias J. Boland**, Abhishek Sundararajan, M. Javad Farrokhi, and Douglas R. Strachan, *Nonlinear Ballistic Transport in an Atomically Thin Material*, ACS Nano, (2016), 10 (1), pp 1231-1239. DOI: 10.1021/acsnano.5b06546
2. **Mathias J. Boland**, Mohsen Nasseri, D. Patrick Hunley, Armin Ansary, and Douglas R. Strachan, *Striped Nanoscale Friction and Edge Rigidity of* MoS_2 *Layers*, RSC Adv., (2015), 5, 92165, DOI: 10.1039/c5ra20617k
3. D. Patrick Hunley, **Mathias J. Boland** and Douglas R. Strachan, *Integrated Nanotubes, Etch Tracks, and Nanoribbons in Crystallographic Alignment to a Graphene Lattice*, Advanced Materials, (2015), 27:813818. DOI:10.1002/adma.201404060
4. D. Patrick Hunley, Abhishek Sundararajan, **Mathias J. Boland**, and Douglas R. Strachan. *Electrostatic force microscopy and electrical isolation of etched few-layer graphene nano-domains*, Applied Physics Letters 105, no. 24 (2014): 243109.
5. Mohsen Nasseri, D. Patrick Hunley, Abhishek Sundararajan, **Mathias J. Boland**, and Douglas R. Strachan. *Tuning between crystallographically aligned carbon nanotube growth and graphene etching*, Carbon 77 (2014): 958-963.

6. Abhishek Sundararajan, **Mathias J. Boland**, D. Patrick Hunley, and Douglas R. Strachan. *Doping and hysteretic switching of polymer-encapsulated graphene field effect devices*, Applied Physics Letters 103, no. 25 (2013): 253505.

7. D. Patrick Hunley, Tyler J. Flynn, Tom Dodson, Abhishek Sundararajan, **Mathias J. Boland**, and Douglas R. Strachan. *Friction, adhesion, and elasticity of graphene edges*, Physical Review B 87, no. 3 (2013): 035417.

CONTRIBUTED TALKS

- *Electrical Transport in Ultra-Short Atomically Thin Devices*, Oral presentation at the American Physical Society March Meeting 2016, Baltimore, MD.

- *Integration of Nanotubes, Etch Tracks, and Nanoribbons in Crystallographic Alignment.*, Oral presentation at the American Physical Society March Meeting 2015, San Antonio, TX.

POSTER PRESENTATIONS

- *Ultra-Short Channel Graphene Devices*, Poster presentation at the Gordon Research Conference on the Chemistry and Physics of Graphitic Carbon Materials 2014, Lewiston, ME.

- *Friction, Adhesion, and Elasticity of Graphene Edges*, Poster presentation at the 9th Kentucky Innovation and Entrepreneurship Conference 2013, Lexington, KY.